

NON-EQUILIBRIUM DYNAMICS IN
LATTICE-CONFINED ANTIFERROMAGNETIC
SPINOR CONDENSATES

By

ZIHE CHEN

Bachelor of Science in Physics
Nanjing University
Nanjing, China
2014

Submitted to the Faculty of the
Graduate College of the
Oklahoma State University
in partial fulfillment of
the requirements for
the Degree of
DOCTOR OF PHILOSOPHY
December, 2020

NON-EQUILIBRIUM DYNAMICS IN
LATTICE-CONFINED ANTIFERROMAGNETIC
SPINOR CONDENSATES

Dissertation Approved:

Dr. Yingmei Liu

Dissertation Adviser

Dr. Albert T. Rosenberger

Dr. Mayukh Lahiri

Dr. Weili Zhang

ACKNOWLEDGEMENTS

I would like to thank my advisor Dr. Yingmei Liu for her guidance, support and patience over the years. I always feel grateful having the chance to join her group. I have learned so much from her and I will always be inspired by her enthusiasm in research, detail oriented personality and willingness to help.

I would like to express my gratitude to my current and former committee members for their support. I have learned a lot from the classes of Dr. Albert T. Rosenberger, Dr. John Mintmire and Dr. Weili Zhang. I gained the knowledge from them to analyze laser, deal with models and calculate stuff. Outside of the classroom they also offered me great opportunities to talk with and learn from them. I also thank Dr. Mayukh Lahiri for agreeing to be my committee member in such a short time so I could complete my PhD degree on time.

Working with members of the Liu group will always be my great experience. I thank the guidance and help from Jie Jiang, Lichao Zhao, Tao Tang when I first joined in and thereafter. We have been through some tough times together, the results are always good and the memories are priceless. I would also thank the current members, Jared Austin and Zachary Shaw, for their help from the first day they joined in.

Many thanks extend to all professors, staffs and students in physics department who I met and talked with, worked together and got help from.

Last but not least, I want to thank my family and friends who cares about me over the years. My father Sibin and mother Ling give me their endless love and unconditional supports, and I dedicate this thesis to them.

Name: ZIHE CHEN

Date of Degree: DECEMBER, 2020

Title of Study: NON-EQUILIBRIUM DYNAMICS IN LATTICE-CONFINED
ANTIFERROMAGNETIC SPINOR CONDENSATES

Major Field: PHOTONICS

Abstract: A spinor Bose-Einstein condensate (BEC) is a new state of matter with both magnetic order and superfluidity. It is highly controllable especially when combining with the optical lattices. Lattice-confined spinor BEC is an ideal candidate for studying non-equilibrium quantum dynamics since it can be easily prepared far from equilibrium. In this dissertation, I present the results from our experimental studies on non-equilibrium quantum dynamics in our BEC system confined by cubic optical lattices.

The introduction part includes the background knowledge of the ground state properties of the spinor Bose gas in both the free space and the optical lattices. I explain how some of the parameters can change the behavior of the whole system. Effects of the net quadratic Zeeman energy q_{net} and the spin-dependent interactions c are emphasized. After we experimentally observed the first-order superfluid (SF) to Mott-insulator (MI) phase transition in the lattice confined antiferromagnetic spinor BECs with adiabatic lattice ramp, we design experiments with quantum quench process to study the non-equilibrium dynamics of the system.

The Quench-Q sequence investigates the spin-mixing dynamics of BECs in deep lattices after the spin state is prepared far from the ground state by quenching q . We observe complex spin oscillations with multiple frequencies after the quench. We analyze the spectra of the oscillations and confirm that a Rabi-type model can explain the data. The data can also be utilized to reveal atom number distributions of an inhomogeneous system, and to study transitions from two-body to many-body dynamics.

The quench-L sequence initialize the non-equilibrium dynamics by quenching the lattice depth across the SF-MI phase transition. The observed spin oscillation is therefore the first experimental study, to our knowledge, on such complicated spin-mixing dynamics. We demonstrate the dependence on the quench speed and lattice potential of the data. Fits of the spin oscillations enable precise measurements of the spin-dependent interaction, a key parameter determining the spinor physics.

Furthermore, I introduce the construction of the optical superlattice by combining a blue-detuned lattice beam with the existing cubic lattice. The state manipulations in such a system have the potential to be applied to quantum information processing. In the end I discuss the possibility of realizing quantum computer based on spinor neutral atoms in optical lattices.

TABLE OF CONTENTS

Chapter	Page
I. INTRODUCTION	1
1.1 Spinor Bose-Einstein condensates	2
1.1.1 Hyperfine spin manifolds in spin-one alkali metal atoms	2
1.1.2 Ground states of spin-one antiferromagnetic spinor condensates	5
1.2 Optical lattices	7
1.2.1 Band structures	11
1.2.2 Bose-Hubbard model	12
1.2.3 Superfluid to Mott-insulator quantum phase transitions	13
1.2.4 Mott insulators in an inhomogeneous system	16
1.2.5 SF to MI phase transitions in lattice-confined spinor condensates	17
1.3 Non-equilibrium dynamics in cold atomic gases	19
1.4 Outline	21
II. EXPERIMENTAL SETUPS AND PROCEDURES	23
2.1 Experimental setups	23
2.2 Experimental procedures	25
2.2.1 Magnetic field calibrations	26
2.2.2 Microwave imaging and microwave dressing field calibrations	27
2.2.3 Lattice calibrations via Kapitza-Dirac diffraction patterns	31
III. DYNAMICS OF SPINOR BECS IN DEEP LATTICES	34
3.1 Spin dynamics in two extremes	35
3.1.1 Single spatial mode approximation	35
3.1.2 Spin-exchanging collisions in few atoms	37

Chapter	Page
3.2 Spin dynamics in an inhomogeneous system	39
3.2.1 Experimental sequences	40
3.2.2 Spin oscillations at multiple frequencies	41
3.3 Spectra analysis and atom number distributions	42
3.4 Empirical model for damped spin oscillations	46
IV. QUANTUM QUENCH ACROSS SUPERFLUID TO MOTT-INSULATOR PHASE TRANSITIONS	 49
4.1 Dynamics after quenching across SF-MI transitions	50
4.1.1 Experimental sequences	51
4.1.2 Precisely measure spin-dependent interactions	53
4.2 Comparisons among quantum quench sequences	54
4.3 Universality and the Kibble-Zurek scaling law	58
4.4 Equilibration and thermalization of isolated quantum many-body system .	62
V. SPINOR BECS IN OPTICAL SUPERLATTICES	64
5.1 Experimental setup of a bichromatic superlattice	65
5.2 Bose-Hubbard model for a bichromatic superlattice	68
5.3 Generation of spin entanglement between cold atoms in superlattices	70
5.3.1 Ground state of cold atoms in optical superlattices	71
5.3.2 Generation of entanglement with state manipulations	72
VI. FUTURE DIRECTIONS	76
6.1 DiVincenzo’s criteria for atom quantum computers	76
6.2 Applications of spinor gases in quantum magnetometry	79
REFERENCES	81
APPENDICES	101
1 APPENDIX A	101
2 APPENDIX B	107
3 APPENDIX C	113

LIST OF TABLES

Table	Page
1.1 Atom number distributions at $n_{\text{peak}} = 6$	16
3.1 Calculated amplitudes D_n for n atoms in a single site at $q/h = 85$ Hz. . . .	42
3.2 Extracted damp rates for Quench-Q 85Hz data fittings	48
4.1 Useful quantities for ^{23}Na atoms in our cubic lattices	54

LIST OF FIGURES

Figure	Page
1.1 Spinor BEC after Stern-Gerlach imaging	3
1.2 Spin states on the Bloch sphere	6
1.3 Optical lattice diagram	9
1.4 Band structures of ultracold atoms in a 1D optical lattice	12
1.5 SF-MI phase diagram of scalar BECs	15
1.6 Inhomogeneous system and Mott shell structure	16
1.7 Measured ρ_0 versus q_B in MI states	18
2.1 Experimental apparatus of the vacuum part	24
2.2 Picture of the optical setup for lattice beams	25
2.3 Magnetic field calibration	26
2.4 Diagram for microwave imaging of spin-0 atoms	27
2.5 Rabi oscillation driven by the resonant microwave	28
2.6 Atom number in a typical ramp sequence	29
2.7 Condensate fraction fit	30
2.8 Kapitza-Dirac diffraction patterns of a one-dimensional optical lattice . . .	31
2.9 Lattice power locking	32
3.1 Equal-energy contour plots	36
3.2 Typical spin oscillation	37
3.3 Rabi-type model for collisions between two atoms	38
3.4 Schematic of our Quench-Q sequence	40
3.5 Spin dynamics after Quench-Q sequences	41
3.6 Quench-Q FFT spectrum and extracted number distributions	43
3.7 The 30Hz Quench-Q data FFT spectrum	45

Figure	Page
3.8 The damp of oscillation amplitudes and fittings for the damp rates	47
4.1 Schematic of our Quench-L sequence	51
4.2 Observed spin dynamics after Quench-L sequences and the extracted U_2/U_0	52
4.3 The extracted U_2/U_0 from all quench data	52
4.4 The comparison between two sequences	54
4.5 Schematic of a special quench sequence	56
4.6 Observed spin dynamics after the special Quench-Q sequences	57
4.7 Schematic diagram of the freeze out region	59
4.8 Quench q cross the phase transition	61
5.1 Optical layout of all lattice beams from one laser.	65
5.2 Superlattice setup and 1D superlattice potentials with various phases.	67
5.3 Superlattice relative phase calibration	68
5.4 Reciprocal lattice	69
5.5 Ground state phase diagram in superlattices	70
5.6 ρ_0 versus u_L^{Blue} in MI state at q_B 6 Hz and 460 Hz	71
5.7 State initialization and gate operations	73
6.1 Single qubit gate and its realization	78

CHAPTER I

INTRODUCTION

A Bose-Einstein condensate (BEC) as a new state of matter was first predicted by Albert Einstein based on Satyendra Nath Bose's theory of photons in 1925 [1]. Identical bosons governed by Bose-Einstein statistics can cross a quantum phase transition from a normal gas to a BEC, when their temperature is lower than a critical temperature $T_c = \frac{h^2}{2\pi m k_B} \left(\frac{n}{\zeta(3/2)} \right)^{2/3}$ [2]. Here T_c is a function of the particle density n and the atomic mass m , h is the Planck constant, k_B is the Boltzmann constant, and ζ is the Riemann zeta function with $\zeta(3/2) \approx 2.61$. Atoms in a BEC have proven to occupy the same lowest energy level and appear as one single matter wave. Such a quantum phenomenon has attracted many research interests. The experimental realization of a BEC, however, was limited by the cooling techniques until the development of laser cooling and trapping in 1990's. Finally the first observation of BEC was accomplished in 1995 in a dilute gas of alkaline metal atoms, after almost 70 years of hard work for cooling atoms down to the nano-kelvin regime [3–5]. Since then, various cooling techniques have been invented and BECs have been realized in many atomic species including alkaline metal atoms (e.g., ^{87}Rb , ^{23}Na , ^7Li , and ^{85}Rb) and alkaline earth atoms [3–6]. Studies of BECs have gradually developed from the weak/no interaction regime to the strong interaction regime [7]. It also becomes an platform for researches over a wide range of fields in physics. Over the past two decades, BECs have been widely investigated and applied to areas such as condensed matter physics, quantum statistics, quantum metrology, and quantum information science [7–11].

Scalar and spinor BECs are two widely-studied types of BECs. In scalar BECs, atoms are

trapped in magnetic fields and hence lose the spin degree of freedom. In opposite, atoms in optical traps preserve this internal degree of freedom since the optical trapping beams provide a spin insensitive potential. Therefore spinor BECs can demonstrate both superfluidity and magnetism. The first spinor BEC was produced in $F = 1$ ^{23}Na gases confined in optical dipole traps in 1998 by Wolfgang Ketterle's group at MIT [12]. The application of optical dipole traps and the realization of spinor BECs have opened up a new research direction using ultracold atomic systems [8]. The magnetism in the ground state and collective excitations have been investigated [13–18]. A magnetic field can break the degeneracy of different spin states. Together with the Feshbach resonance and optical lattices to further manipulate interatomic interactions, spinor BECs have become a highly controllable system suitable for studying condensed-matter models, as well as atomic entanglement and squeezing important for quantum information and quantum computing [8]. Preparing topological objects is also experimentally available with spinor BECs. Many theoretical and experimental works have advanced our understandings on spinor BECs, including spin-mixing dynamics [19, 20], ground state phase diagrams, quantum phase transitions [19, 21, 22], spin textures, and topological excitations [8].

My particular research interest is to experimentally investigate antiferromagnetic sodium BECs in cubic optical lattices, especially the non-equilibrium dynamics of such a system.

1.1 Spinor Bose-Einstein condensates

To experimentally study cold atoms in optical lattices, we first prepare atoms into a purely polarized BEC and then gradually load them into lattices. Therefore understanding BECs in free space is necessary.

1.1.1 Hyperfine spin manifolds in spin-one alkali metal atoms

For alkali-metal atoms at low magnetic fields, the total angular momentum \mathbf{F} is a good quantum number that can well describe their hyperfine structures. Here $\mathbf{F} = \mathbf{J} + \mathbf{I}$ is the

sum of the electron angular momentum and the nuclear angular momentum. For example, $I = \frac{3}{2}$ and $J = \frac{1}{2}$ in the ground state of ^{23}Na atoms, so $F = 1$ or $F = 2$.

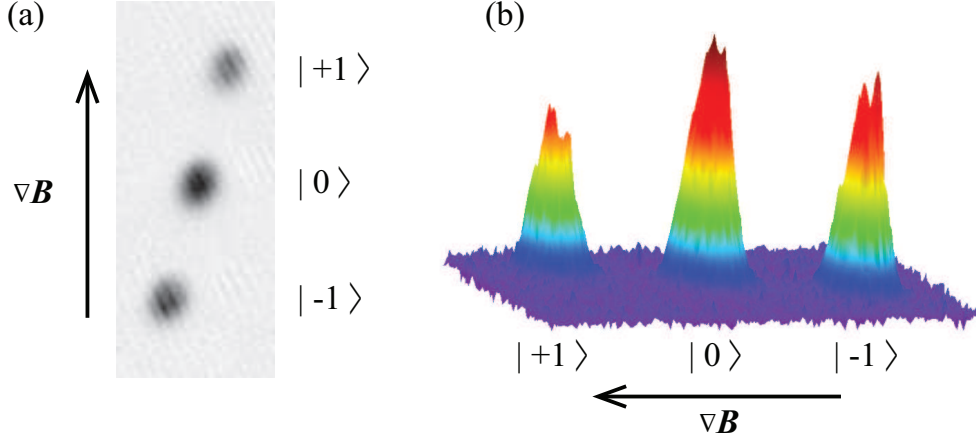


Figure 1.1: (a) Three spin components of a $F = 1$ BEC get separated after a Stern-Gerlach imaging. (b) The density profile of the image shown in Panel (a).

We choose to create a BEC of ^{23}Na atoms at the $F = 1$ hyperfine manifold, as $F = 1$ atoms have long lifetime while $F = 2$ atoms are unstable and decay quickly [23]. When an external magnetic field is applied, $F = 1$ atoms can be energetically split into three Zeeman sublevels, i.e., $|F = 1, m_F = +1\rangle$, $|F = 1, m_F = 0\rangle$, and $|F = 1, m_F = -1\rangle$, which can be detected separately with techniques like the Stern-Gerlach imaging as Fig. 1.1 shows. If the magnetic field is along z direction, $\mathbf{B} = B\hat{z}$, the energy of the three Zeeman states can be expressed as follows [24],

$$\begin{aligned}
 E_{\pm} &= -\frac{E_{\text{hfs}}}{8} \pm g_I \mu_I B - \frac{1}{2} E_{\text{hfs}} \sqrt{1 \pm \alpha + \alpha^2}, \\
 E_0 &= -\frac{E_{\text{hfs}}}{8} - \frac{1}{2} E_{\text{hfs}} \sqrt{1 + \alpha^2}.
 \end{aligned} \tag{1.1}$$

Here E_{hfs} is the hyperfine energy splitting, $\alpha = (g_J \mu_B - g_I \mu_I)B/E_{\text{hfs}}$, g_I and g_J respectively represent the Landé g factor for an atom and for a valence electron, and μ_I and μ_B respectively represent the nuclear magneton and the Bohr magneton. The linear Zeeman energy is $p_{\text{net}} = (E_{+1} - E_{-1})/2$, and it remains no change during the coherent intercon-

version between two $|F = 1, m_F = 0\rangle$ atoms and one $|F = 1, m_F = +1\rangle$ atom with one $|F = 1, m_F = -1\rangle$ atom, which is the only spin changing process we are interested in during the experiment. The quadratic Zeeman energy is [25]

$$q_B = (E_{+1} + E_{-1} - 2E_0)/2 = \frac{gJ\mu_B - gI\mu_I}{16E_{\text{hfs}}} B^2, \quad (1.2)$$

when there is only a magnetic field applied. For ^{23}Na atoms $p(B) \approx -Bh \cdot 0.70$ MHz/G for the adjacent magnetic sublevels with $F = 1$ [26], and $q_B \approx B^2h \cdot 277$ Hz/G² [27].

Besides applying a magnetic field to realize the energy splitting among the Zeeman states, a microwave dressing field can also introduce a quadratic Zeeman shift that can be both positive and negative. This energy shift is due to the AC Start effect, and is state dependent since the microwave frequency is close to the resonance between hyperfine states. As shown in [27–29], the energy shift of $|F = 1, m_F\rangle$ is

$$\begin{aligned} \delta E|_{m_F} &= \frac{h}{4} \sum_{k=0,\pm 1} \frac{\Omega_{m_F, m_F+k}^2}{\Delta_{m_F, m_F+k}} \\ &= \frac{h}{4} \sum_{k=0,\pm 1} \frac{\Omega_{m_F, m_F+k}^2}{\Delta - [(m_F + k)/2 - (-m_F/2)]\mu_B B}. \end{aligned} \quad (1.3)$$

Δ is the detuning from the transition $|F = 1, m_F = 0\rangle \leftrightarrow |F = 2, m_F = 0\rangle$, which is independent of the magnetic field strength. $k = 0$ or ± 1 , depending on the polarization of the microwave pulse. And the transition $|F = 1, m_F\rangle \leftrightarrow |F = 2, m_F + k\rangle$ has the on-resonance Rabi frequency $\Omega_{m_F, m_F+k} \propto \sqrt{I_k} C_{m_F, m_F+k}$, where C_{m_F, m_F+k} is the Clebsch-Gordan coefficient of the transition and I_k is the intensity of the polarized microwave pulse. Then the quadratic Zeeman shift due to this microwave dressing field is [25]

$$q_M = \frac{\delta E|_{m_F=1} + \delta E|_{m_F=-1} + \delta E|_{m_F=0}}{2}. \quad (1.4)$$

By applying a microwave dressing field, the net q would be $q = q_B + q_M$. Then our system is able to study the ground state and dynamics of a sodium BEC at negative q [22, 27], and we can control the ramp curve of q through controlling the frequency of the microwave pulse [22]. The calibration of microwave fields is explained in Chapter 2.

1.1.2 Ground states of spin-one antiferromagnetic spinor condensates

The Hamiltonian of spinor BECs can be written as

$$\hat{H} = \hat{H}_K + \hat{H}_V + \hat{H}_Z + \hat{H}_{\text{int}} , \quad (1.5)$$

Here \hat{H}_K and \hat{H}_V are the kinetic energy and potential energy, and \hat{H}_Z and \hat{H}_{int} are the Zeeman energy and the spin-dependent interaction energy.

Based on the discussion in the last section and by assuming the magnetic field is along the \mathbf{z} axis, \hat{H}_Z can be expressed as [25],

$$\hat{H}_Z = \int d\mathbf{r} (p_{\text{net}} \hat{F}_z + q \hat{F}_z^2) \quad (1.6)$$

where $\hat{F}_\gamma = \sum_{i,j=-1}^1 \hat{\phi}_i^\dagger(\mathbf{r}) (f_\gamma)_{ij} \hat{\phi}_j(\mathbf{r})$ with $\gamma = x, y, z$ is the γ -component of $\hat{\mathbf{F}}$, $\hat{\phi}_{m_F}(\mathbf{r})$ is the field operator that annihilates an atom in an m_F state at the location \mathbf{r} . f_γ are the spin-1 matrices and $(f_\gamma)_{ij}$ is the corresponding (i, j) matrix element.

Only the two-atom s -wave collisions have proven to be useful in deriving an expression for the interaction energy of spin-1 ^{23}Na BECs. Therefore the interaction energy for an atom pair is expressed as [13, 30],

$$V_{\text{pair}} = \sum_{F_{\text{pair}}=0,2} \frac{4\pi\hbar^2 a_{F_{\text{pair}}}}{M} \delta(\mathbf{r} - \mathbf{r}') \hat{P}_{F_{\text{pair}}} , \quad (1.7)$$

with $a_{F_{\text{pair}}}$ being the s -wave scattering length in the total spin F_{pair} and M being the mass of an atom, and $\hat{P}_{F_{\text{pair}}}$ being a projection operator that projects a pair of atoms onto the spin F_{pair} state.

After a second quantization, similar to the discussion in [8], the interaction operator of the whole system is,

$$\hat{H}_{\text{int}} = \frac{1}{2} \int d\mathbf{r} (c_0 : \hat{n}^2 : + c_2 : \hat{\mathbf{F}}^2 :) , \quad (1.8)$$

where $::$ denotes normal ordering, and

$$c_0 = \frac{4\pi\hbar^2}{M} \frac{a_0 + 2a_2}{3}, \quad c_2 = \frac{4\pi\hbar^2}{M} \frac{a_2 - a_0}{3}. \quad (1.9)$$

c_0 therefore is the spin-independent interaction strength while c_2 is the spin-dependent interaction strength.

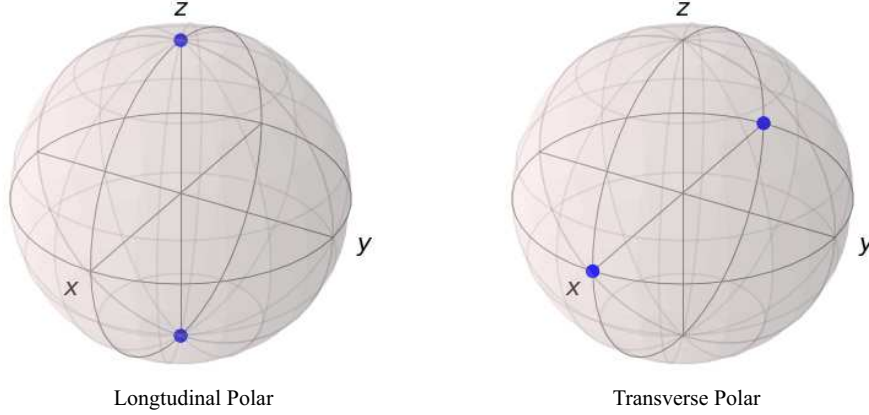


Figure 1.2: Longitudinal polar and transverse polar states on the Bloch sphere.

In the single spatial mode approximation (SMA) [31, 32], all atoms take the same spatial mode $\Phi(\mathbf{r})$ and the wave function $\Psi_{m_F}(\mathbf{r}) = \Phi(\mathbf{r})\psi_{m_F}e^{-\frac{iE_{m_F}t}{\hbar}}$. The mean-field (MF) energy is thus [8]

$$E = \frac{c_2 n}{2} \langle \hat{\mathbf{F}} \rangle^2 + p \langle \hat{F}_z \rangle + q \langle \hat{F}_z^2 \rangle, \quad (1.10)$$

with $n = \int d^3\mathbf{r} |\Phi^4| / \int d^3\mathbf{r} |\Phi^2|$ being the average density.

When no external field is applied, only the first term is considered and the minimum energy is determined by the sign of c_2 . When $c_2 > 0$ (e.g., for $F = 1$ ^{23}Na), the minimum is at $|\langle \hat{\mathbf{F}} \rangle| = 0$. This type of condensates is denoted as “antiferromagnetic”. For $c_2 < 0$ (e.g., for $F = 1$ ^{87}Rb), the condensates favors the “ferromagnetic” state.

When an external field is applied, the MF phase diagram can be found by finding the minimum of E . We can express ρ_{m_F} as the fractional population of the spin state $|F = 1, m_F\rangle$, and $m = \rho_{+1} - \rho_{-1}$ is the magnetization. Typically for $p = 0, m = 0$, the antiferromagnetic ground state is a longitudinal polar (LP) state $\psi = (0, 1, 0)^T$ at $q > 0$ with $\rho_0 = 1$ or a

transverse polar (TP) state $\psi = \frac{(1, 0, e^{i\phi})^T}{\sqrt{2}}$ at $q < 0$ with $\rho_0 = 0$, here ϕ is arbitrary. This has been experimentally tested in several systems [22, 33]. We can express the spin state as two points on the Bloch sphere treating a spin-1 particle as two spin-1/2 particles following [8], then the LP and TP states on a Bloch sphere are shown in Fig. 1.2

The many-body Hamiltonian of a $F = 1$ spinor BEC without the MF approximation have been demonstrated to be analytically solvable [31]. With no external magnetic field, the spin-dependent part of the Hamiltonian is expressed as [8, 31]

$$H_s = \frac{c_2 n}{2} \left(\frac{\hat{\mathbf{F}}_{\text{tot}}^2}{N} - 2 \right), \quad (1.11)$$

with $\mathbf{F}_{\text{tot}} = \sum_i \hat{\mathbf{F}}_i$ the total spin operator and N the atom number. Then apparently for $c_2 > 0$ the ground state with even N is $|F_{\text{tot}} = 0, M_F = 0\rangle$, i.e. a spin singlet is the ground state for antiferromagnetic BECs around $q/h = 0$ [34]. This state is rotational symmetric with large number fluctuation of each sublevel. It can be expressed as the superposition of a chain of Fock state $|k, N - 2k, k\rangle$ with k from 0 to $N/2$. The state is therefore highly entangled and has potential research interests in the quantum information processing [35]. However, its experimental realizations are restricted into a narrowly allowed range of q ($|q|/h < 2 \times 10^{-9}$ Hz) for BECs in free space since the state quickly breaks down under symmetry-breaking perturbations [8, 34]. We have demonstrated that such restriction can be greatly relaxed by loading atoms into optical lattices [36].

1.2 Optical lattices

Lattice structures in crystals are atomic arrays that form periodic potentials and determine the behavior of electrons in them. Similar periodic potentials can be simulated with optical lattices and optical superlattices in ultracold atomic systems. A one-dimensional (1D) monochromatic optical lattice consists of an optical standing wave created by one pair of counter-propagating laser beams at a fixed wavelength. When BECs are loaded in an optical lattice, periodic confinements can enhance the interaction among atoms and the system may

become strongly correlated. The interatomic interactions U and tunnelling rate J among neighboring lattice sites in lattice-confined BECs can be precisely controlled by changing the lattice potential depth. Lattice-trapped BECs thus provide an opportunity to study physics beyond the MF theory that can well explain weakly interacting dilute gases. So far lattice-trapped cold atomic gases have found their applications in various fields like optical lattice clocks for precise measurement of time [37], or quantum information processing as quantum memories or quantum registers [38, 39]. And such systems can work as quantum simulators to simulate many models originally proposed for strongly interacting electronic systems [40]. For example, studies of Fermi-Hubbard model using Fermions in optical lattices will enhance the understanding of high-temperature superconductors [41]. The ground-breaking work is the experimental study of lattice-confined scalar BECs of rubidium atoms by Ref. [42]. They confirmed a superfluid (SF) to Mott-insulator (MI) quantum phase transition happening at a critical value of U/J .

Due to the additional spin degree of freedom, spinor BECs confined in optical lattices display richer phases than scalar BECs and allow interesting spin dynamics [43–46]. For example, because of the appearance of meta-stable superfluid and Mott-insulator phases, quantum SF-MI phase transitions in lattice-confined antiferromagnetic spinor BECs are predicted to be first order around the tip of even filling Mott lobes [47–49]. In contrast, only second-order quantum SF-MI phase transitions occur in scalar BECs. The dynamics of spinor gas in optical lattices also has special features, for example when the density dynamics and spin-mixing dynamics happen simultaneously [50].

Atoms in optical lattices can be localized in each site, and their hyperfine states can serve as the two levels of a quantum qubit. Atoms with spin degree of freedom in the optical lattices can be used to build up large-scale entanglement. Thus such lattice-confined spinor atomic system is one of the candidates for quantum information processing and quantum computing [39].

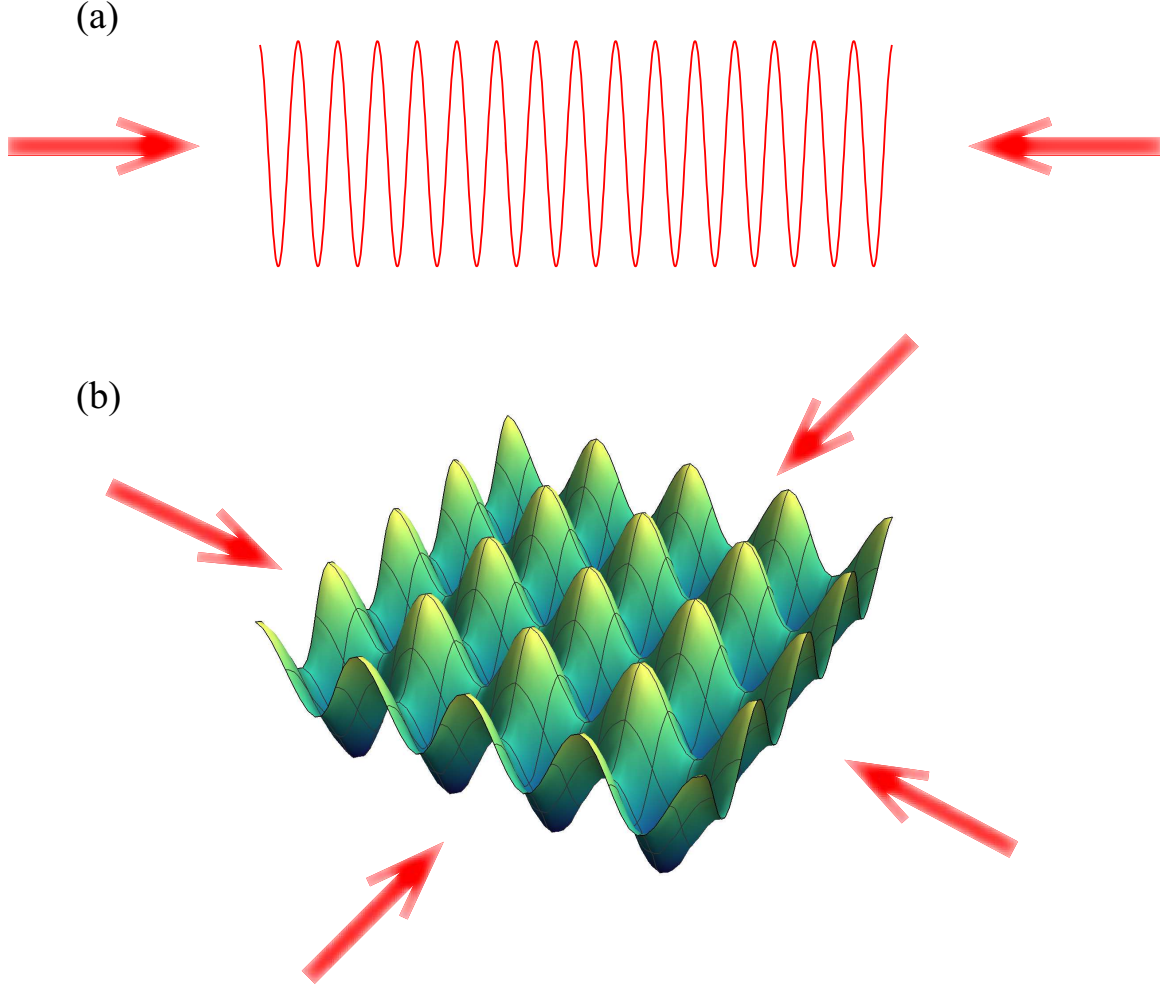


Figure 1.3: (a) Two counter-propagating laser beams form a standing wave. (b) 2D optical lattices are formed by two pairs of optical standing waves along different directions.

Optical dipole traps and optical lattices

When an atom is placed in a light field, the interaction between the light-induced dipole moment and the light field induces the AC-Stark energy shift. When the applied light field is off resonant, such energy shift can create a trapping potential [51],

$$V(\mathbf{r}) = \frac{3\pi c^3 \hbar \Gamma}{2\omega_R^2 \Delta} I(\mathbf{r}) , \quad (1.12)$$

where Γ is the nature linewidth, ω_R is the resonance frequency, and Δ is the detuning. This is similar to an optical dipole trap used in the laser cooling process. A one-dimensional optical lattice potential can be created by a superposition of two laser beams. For example,

by retro-reflecting one ODT laser beam with a mirror, we can generate a 1D optical lattice. The following descriptions of lattice potentials are mainly based on [25, 52].

Assume the laser light is a Gaussian beam at a wavelength λ_L , the Gaussian beam's intensity is expressed as [52]

$$I(r, z) = \frac{2P}{\pi\omega_0^2} \left[1 - 2 \left(\frac{r}{\omega_0} \right)^2 - \left(\frac{z}{z_R} \right)^2 \right]. \quad (1.13)$$

Then the one-dimensional lattice potential can be written as

$$V_{lat}(r, z) = 4V_s \cos^2 \left(\frac{2\pi z}{\lambda_L} \right) \left[1 - 2 \left(\frac{r}{\omega_0} \right)^2 - \left(\frac{z}{z_R} \right)^2 \right], \quad (1.14)$$

$$\text{where } V_s = \frac{3\pi c^3 \hbar \Gamma}{2\omega_R^2 \Delta} \frac{2P}{\pi\omega_0^2}, \quad (1.15)$$

P is the power of the lattice beam, ω_0 is the Gaussian beam waist, and $z_R = \pi\omega_0^2/\lambda_L$.

Usually we describe the lattice potential depth with a dimensionless factor $u_L = 4V_s/E_R$. Here $E_R = \hbar^2 k_L^2 / (2M)$ is the recoil energy, M is the mass of the atom, and $k_L = 2\pi/\lambda_L$ is the wave vector of the lattice beam. Considering the overlapping of a pair of lattice beams and ignoring the slowly varying harmonic term, the lattice potential can be expressed as

$$V_{lat}(x) = \frac{1}{2} u_L E_R [1 + \cos(2k_L x)]. \quad (1.16)$$

Different lattice potentials can be formed by changing the number of laser beams as well as their relative frequencies and directions. The 1D and 2D lattice potentials are shown in Fig. 1.3(a) and Fig. 1.3(b) respectively. A 1D optical lattice forms a 2D pancake structure, while a 2D optical lattice constructs a 1D tube structure. Within a 3D optical lattice, the potentials in each lattice site are similar to zero-dimensional dots. In our experiment, we construct a cubic lattice with three pairs of counter-propagating lattice beams perpendicular to each other. The lattice potential depth for such cubic lattices, based on the above discussion, can be easily expressed as

$$V_{lat}(\mathbf{r}) = u_L E_R \sum_{\alpha=x,y,z} \frac{1}{2} [1 + \cos(2k_L r_\alpha)]. \quad (1.17)$$

1.2.1 Band structures

To describe the BEC system trapped in optical lattices, we first neglect the interaction between atoms and investigate the movement of single atom in the periodic lattice potentials. For convenience, I will show the calculation of wave functions in a 1D lattice potential, which is constructed by one pair of counter-propagating laser beams along the x direction. Since the potential V_{lat} is periodical, the Bloch theorem can be used and the solution of the wave function has the following form [53],

$$\Psi_{n\mathbf{q}}(\mathbf{x}) = e^{i\mathbf{q}\cdot\mathbf{x}} u_{n\mathbf{q}}(\mathbf{x}) . \quad (1.18)$$

Here \mathbf{q} is the quasimomentum, n is the band index, and $u_{n\mathbf{q}}(\mathbf{x})$ has the same periodicity as the lattice. And its Schrödinger equation can be easily expressed as

$$H\Psi_{n\mathbf{q}}(\mathbf{x}) = E_{n\mathbf{q}}\Psi_{n\mathbf{q}}(\mathbf{x}), \quad H = \frac{1}{2m}\hat{p} + V_{\text{lat}}. \quad (1.19)$$

Substituting Eq. 1.18 into Eq. 1.19, u and V can be extended with their Fourier series as [25, 52]

$$\begin{cases} u_{nq}(x) = \frac{1}{\sqrt{2\pi}} \sum_{j=-\infty}^{\infty} c_{j,nq} e^{-ijk_L x} , \\ V(x) = \sum_r V_r e^{-ijk_L r} . \end{cases}$$

As $V_{\text{lat}} = \frac{1}{4}u_L E_R (e^{-2ik_L x} + e^{-2ik_L x} + 2)$, Eq. 1.19 can be expressed in the matrix form as follows,

$$H_{j,j'} = \begin{cases} [(2j + q/k_L)^2 + u_L/2]E_R , & \text{if } j = j' ; \\ -u_L E_R/4 , & \text{if } |j - j'| = 1 ; \\ 0 , & \text{if } |j - j'| > 1 . \end{cases} \quad (1.20)$$

For a given quasi-momentum q , the energy bands are characterized by the eigenvalues E . These eigenvalues and corresponding eigenstates can be calculated numerically if the Hamiltonian is truncated at a typical value like 20 in our calculations. Figure 1.4 shows

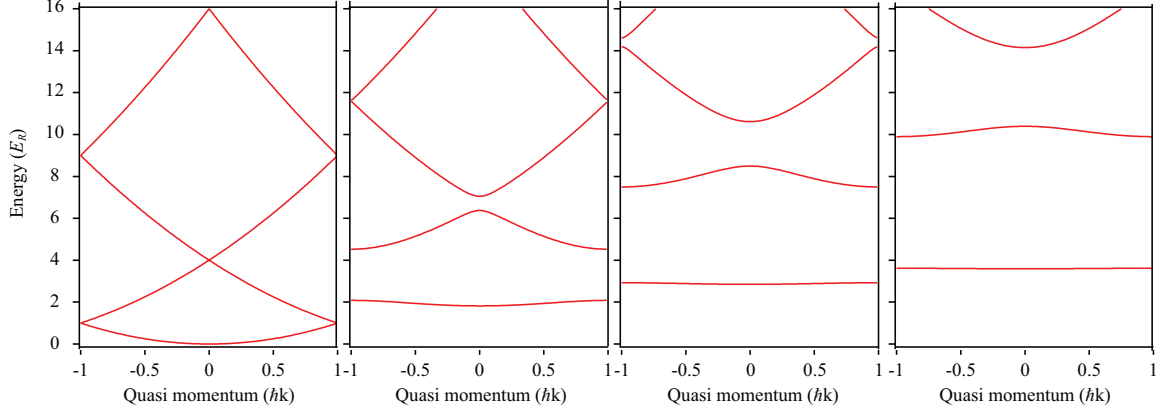


Figure 1.4: Band structures of ultracold atoms in a 1D optical lattice at $u_L = 0E_R$, $u_L = 5E_R$, $u_L = 10E_R$, and $u_L = 15E_R$.

the band structure calculated at different lattice depths [25]. When the lattice depth is 0, it shows the energy-momentum relationship of atoms in free space. As the lattice depth arises, the bands flatten and the band gaps are increased.

For cubic lattices, the equation is separable along each direction. So the wave function can be calculated separately and the energy is the sum of the eigenenergy along each direction.

1.2.2 Bose-Hubbard model

The discussion in the previous subsection does not consider interactions among atoms. In fact, interatomic interactions are important and determine the formation of various phases for BECs in optical lattices, such as superfluid phases, nematic insulator phases, and spin-singlet phases for $F = 1$ spinor condensates confined in cubic optical lattices [44]. To better describe lattice Bose gases, I will discuss the widely-used Bose-Hubbard model.

The system of bosonic atoms in 3D optical lattices can be well described by the Bose-Hubbard model, which was introduced from the work of John Hubbard in solid state physics and has been widely used in lattice-confined bosonic systems [42, 54–57]. If the lattice depth is deep enough and atoms are localized, the Bloch wave basis should be substituted by a

set of localized basis, i.e., Wannier functions [25, 52],

$$u_{n\mathbf{q}}(\mathbf{r}) = \frac{1}{\sqrt{v_B}} \sum_{\mathbf{R}} w_n(\mathbf{r} - \mathbf{R}) e^{i\mathbf{q}\cdot\mathbf{R}} . \quad (1.21)$$

Here v_B is the volume of the first Brillouin zone, $\mathbf{R} = \sum_{\alpha} n_{\alpha} \mathbf{a}_{\alpha}$ is the position of each lattice site with the unit lattice vector \mathbf{a}_{α} in α -axis. And the Wannier functions are expressed after a Fourier transform as follows [25, 52],

$$w_n(\mathbf{r} - \mathbf{R})(\mathbf{r}) = \frac{1}{\sqrt{v_B}} \int d\mathbf{q} u_{n\mathbf{q}}(\mathbf{r}) e^{-i\mathbf{q}\cdot\mathbf{R}} , \quad (1.22)$$

If the system energy is smaller than the excitation energy to the second band, it is good to consider only the lowest band Wannier functions and the field operator $\hat{\phi}(\mathbf{r}) = \sum_i \hat{b}_i w_0(\mathbf{r} - \mathbf{R}_i)$ for scalar BECs without spin degrees of freedom. Here \hat{b}_i denotes the operator annihilating a particle at i th site. Then based on Eq. 1.22, in second quantization the Hamiltonian can be written as [57],

$$H = \frac{U_0}{2} \sum_i n_i(n_i - 1) - J \sum_{\langle i,j \rangle} b_i^\dagger b_j - \mu \sum_i n_i . \quad (1.23)$$

The first term is the spin-independent interaction term tending to localize atoms to lattice sites. Its strength is characterized by $U_0 = c_0 \int d\mathbf{r} |w_0(\mathbf{r})|^4$. And $n_i = b_i^\dagger b_i$ is the atom number at site i . The factor $J = \int d\mathbf{r} w_0^*(\mathbf{r} - \mathbf{R}_i) [-\frac{\hbar^2}{2M} \nabla^2 + V_{lat}(\mathbf{r})] w_0(\mathbf{r} - \mathbf{R}_j)$ in second term describes tunnelling among neighboring lattice sites and this term is the hopping term tending to delocalize atoms over the lattice. μ is the chemical potential. By changing u_L , we are able to conveniently control U_0 and J and hence, the ratio between them.

1.2.3 Superfluid to Mott-insulator quantum phase transitions

If the tunnelling term in the BH model is dominant, which means J is much larger than U_0 , the system behaves similar to a non-interacting case and atoms are delocalized over the whole lattice to minimize their kinetic energy. So the ground state is a superfluid (SF)

state and can be expressed as the product of identical single atom states with N atoms at m lattice sites [42]

$$\Psi_{SF} \propto \sum_{i=1}^m b_i^\dagger |0\rangle, \quad (1.24)$$

where b_i^\dagger is the creation operator in site i .

Apparently we can use a macroscopic wave function to describe the system. Therefore when we take a time-of-flight (TOF) image after an abrupt release of the trap potential, we are able to see sharp momentum peaks resulting from the interference among multiple matter waves with a same constant macroscopic phase.

In the opposite limit where $U/J \gg 1$, the ground state has a fixed atom number n at each site for minimizing the interaction energy. This is called a Mott-insulator (MI) state and is simply expressed as [42]

$$\Psi_{MI} \propto \prod_{i=1}^m (b_i^\dagger)^n |0\rangle. \quad (1.25)$$

In the MI phase, strong interatomic interactions eliminate the macroscopic phase coherence and the theories for weak-interacting atoms are no longer applicable.

As described above, the ratio of U_0 to J for BECs in optical lattices can be manipulated by varying the lattice potential u_L . When U_0/J reaches critical values, transitions between the SF and MI phases could happen. Such a quantum phase transition is driven by quantum fluctuations rather than thermal effects, and thus happens at extremely low temperature.

Based on the Hamiltonian shown in Eq. 1.23, we can calculate the ground state at every set of μ/U_0 and u_L [58, 59]. A predicted phase diagram for scalar BECs in cubic optical lattices is shown in Fig. 1.5. The value of μ/U_0 determines the filling factor n in a lattice site. And the transition point u_c for each filling factor can be easily read from the edge of each Mott lobe. As also can be seen from Fig. 1.5 inset, superfluid states in shallow lattices demonstrate distinct interference peaks in the TOF absorption images, showing trustworthy evidence for a long-range phase coherence. As u_L is increased beyond u_c , interference peaks vanish and only a uniform broad background is left in TOF images, indicating atoms enter the MI phase. If u_L is reduced and atoms get back to a superfluid phase, a revival of the

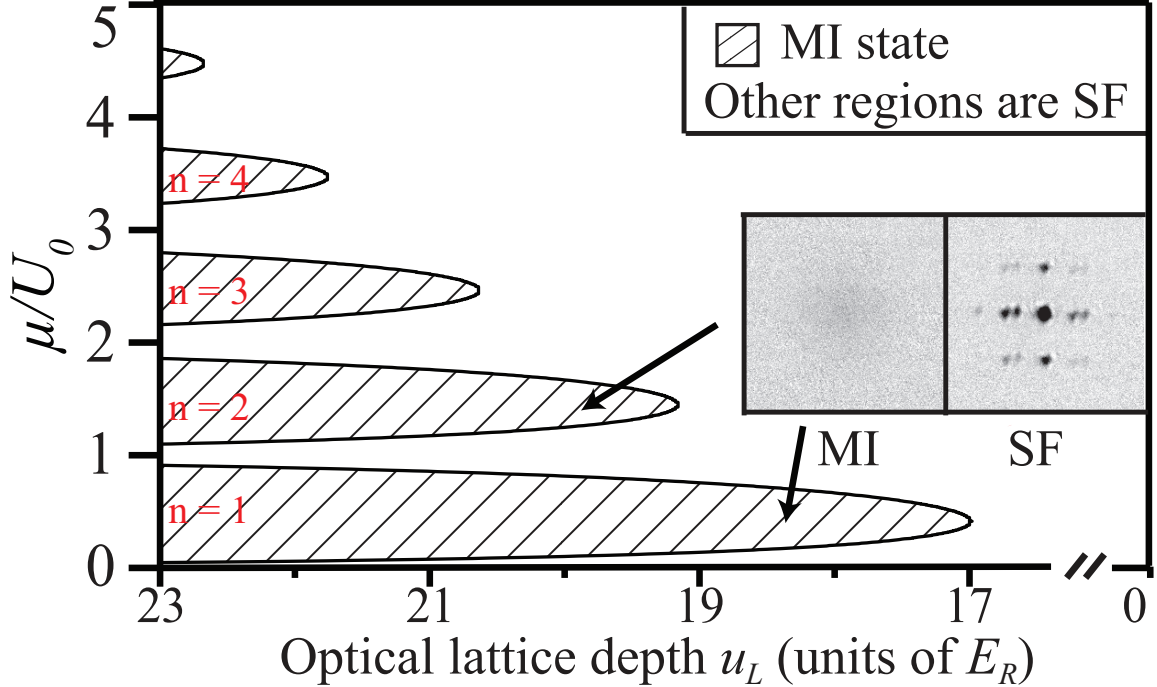


Figure 1.5: A typical phase diagram of scalar BECs. The shaded regions are Mott lobes with various filling factors from $n = 1$ to $n = 5$ determined by the ceiling of μ/U_0 . Inside (outside) each Mott lobe the ground state is a MI (SF) phase. Inset: typical TOF pictures showing the SF and MI states.

interference peaks is expected as the phase coherence is restored. Such a loss and revival of the phase coherence in ultracold atomic systems has been used to test if atoms have undergone a SF-MI phase transition. For example, this method was applied to confirm the first experimental observation of a SF-MI phase transition in 2002 [42].

In principle a quantum phase transition only happens at the quantum critical point (QCP) when the temperature $T = 0$. For real experimental systems with $T > 0$, there is a quantum critical region above the QCP where $\hbar\omega_c > k_B T$ with ω_c the characteristic frequency of the quantum oscillation. Therefore the quantum fluctuations inside the quantum critical region still dominate. And the corresponding states are influence by the QCP [60]. Studies of the finite temperature properties of the systems enables thermometry and testing the finite-temperature phase diagrams [61–63].

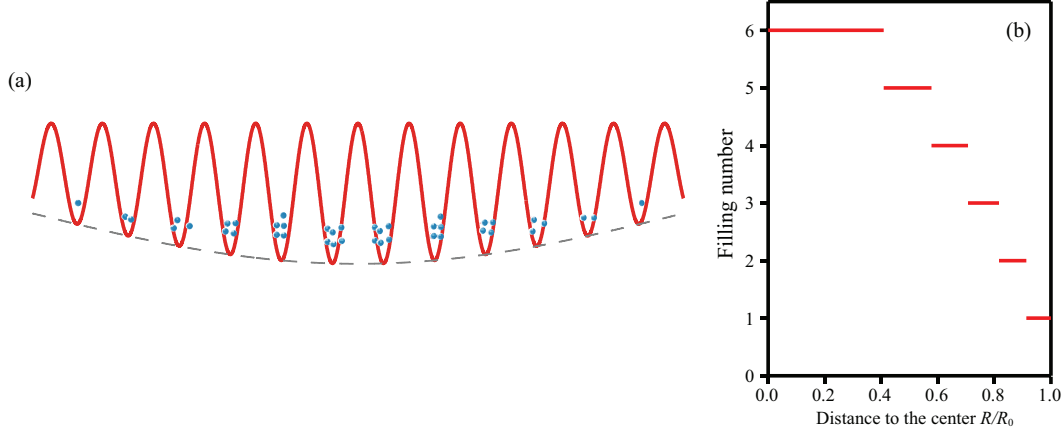


Figure 1.6: (a) Schematic of spatial distributions in a lattice-trapped inhomogeneous system. (b) The calculated filling numbers depending on the position of the atoms show shell structure for atoms in a harmonic trap.

1.2.4 Mott insulators in an inhomogeneous system

As Fig. 1.5 shows and the above discussion mentioned, the filling number of a lattice site is determined by the ceiling of μ/U_0 when the system is in the MI phase. If we consider an external confinement or the Gaussian profile of the lattice beams, the system should be inhomogeneous as shown in Fig. 1.6(a) where in lattice site i there is an energy offset ϵ_i . So it is the local chemical potential $\mu_i = \mu - \epsilon$ that determines the filling number in site i . Therefore the center of the trap has the largest μ_i and the largest n , while the border of the atom cloud has μ_i decreasing to 0, so does the n . This is often referred as a shell structure or 'wedding cake' structure. The corresponding diagram is shown in Fig. 1.6(b). Such density distribution has been tested via different simulation methods [57, 64], and has also been verified in the experimental systems [65–67].

In our system the peak occupation number n_{peak} is tunable as we can change the total atom number of the system. We can then calculate the corresponding atom number distribution at each n for a fixed n_{peak} , as shown in Table. 1.1 for $n_{\text{peak}} = 6$. These distributions are used in taking weighted averages of individual Mott lobes [68].

n	1	2	3	4	5	6
χ_n	0.081968	0.148261	0.196065	0.220757	0.213094	0.139854

Table 1.1: Atom number distributions at $n_{\text{peak}} = 6$.

1.2.5 First-order Superfluid to Mott-insulator phase transitions in lattice-confined antiferromagnetic spinor condensates

Different from scalar BECs, the Bose-Hubbard model predicts that the SF-MI phase transitions can be first (second) order in antiferromagnetic spinor BECs, as the order parameter abruptly (continuously) changes at the phase transition point. The nature of SF-MI phase transitions is determined by the competition between spin-dependent interactions U_2 and the quadratic Zeeman energy q_B .

By including q_B and U_2 , the Bose-Hubbard model for a $F = 1$ spinor BEC can be expressed as [46, 68–70],

$$\begin{aligned}
 H = & \frac{U_0}{2} \sum_i n_i(n_i - 1) - J \sum_{\langle i,j \rangle, m_F} b_{i, m_F}^\dagger b_{j, m_F} - \mu \sum_i n_i \\
 & + \frac{U_2}{2} \sum_i (\vec{S}_i^2 - 2n_i) + q_B \sum_{i, m_F} m_F^2 n_{i, m_F}.
 \end{aligned} \tag{1.26}$$

The first three terms are similar to those shown in the Bose-Hubbard model for scalar BECs. U_2 marks the strength of spin-dependent interactions. In fact, $U_2/U_0 = c_2/c_0 \simeq 0.04$ for ^{23}Na [67, 68]. The term \vec{S}_i is the spin operator at site i , with $S_{ix,y} = \frac{1}{\sqrt{2}} (b_{i,0}^\dagger b_{i,1} \pm b_{i,1}^\dagger b_{i,0} + b_{i,-1}^\dagger b_{i,0} \pm b_{i,0}^\dagger b_{i,-1})$, $S_{iz} = b_{i,1}^\dagger b_{i,1} - b_{i,-1}^\dagger b_{i,-1}$. The linear Zeeman energy is not counted since it remains the same during the spin interconversions. The last term q_B is the quadratic Zeeman energy. If we neglect the hopping term $(b_{i, m_F}^\dagger - \langle b_{i, m_F}^\dagger \rangle)(b_{j, m_F} - \langle b_{j, m_F} \rangle)$, the decoupling MF theory can simplify the above Hamiltonian to a site-independent form [46], and the phase diagram can be calculated based on it.

The experimental study of the ground state properties for antiferromagnetic BECs in cubic optical lattices has been conducted in our lab [68]. Signatures of the first-order SF-MI phase transitions have been observed in our system, including the hysteresis effect of the transition point, significant heatings across the phase transitions, and changes in spin populations with the phase transitions [68]. The last term is interesting for two reasons. First, the theory predicts that spin singlet states exist in even filled sites in deep lattices. The singlet state is

an entangled state, which can potentially be applied to quantum information processing [36]. This is related to the content in chapter 5. Second, changes in spin populations across the phase transitions enable studies on few-body non-equilibrium spin dynamics, which will be discussed later.

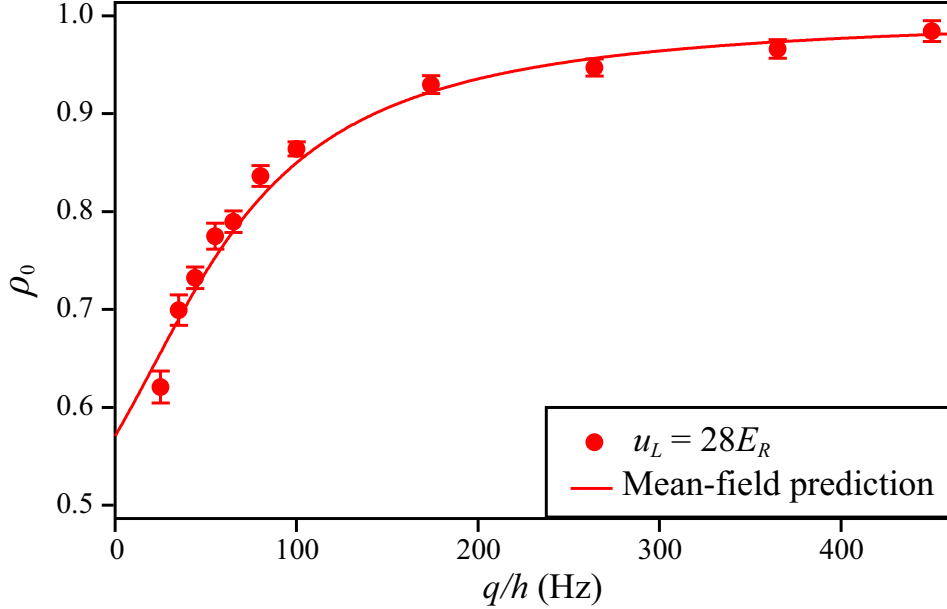


Figure 1.7: Measured ρ_0 versus q_B with u_L ramping up to $28E_R$ (in the MI phase). The solid line is the prediction for $n_{\text{peak}} = 6$.

By solving the site-independent Hamiltonian in deep lattices ($J = 0$), one is able to find the ground state at given q and μ . For example, for $\mu = 1.4U_0$ corresponding to the $n = 2$ Mott lobe, the Hamiltonian can be diagonalized and expressed in a matrix form in the occupation basis $|\vec{n}\rangle = |n_1, n_0, n_{-1}\rangle$. Then we can find the ground state of this Hamiltonian as $|\psi_g\rangle = \frac{U_2 - 2q_B + \sqrt{4q_B^2 - 4q_B U_2 + 9U_2^2}}{2\sqrt{2}U_2} |101\rangle - |020\rangle$ (non-normalized), with the eigenvalue $E_g = \frac{1}{2} \left(2q_B - U_2 - \sqrt{4q_B^2 - 4q_B U_2 + 9U_2^2} \right)$ [36, 68]. These formulas are also useful when we calculate the spin-mixing dynamics in individual lattice sites since they follow the same Hamiltonian. Fig. 1.7 shows the measured ρ_0 at $u_L = 28E_R$ with q varying over a large range. Our data agree with the prediction at $n_{\text{peak}} = 6$ (red line). Such an agreement indicates the change of ρ_0 after the first-order SF-MI transition at low magnetic fields is probably due to the formation of the spin singlets in even filling Mott lobes. This ρ_0 dependence on q and u_L can also be used to initialize spin dynamics in such

systems, as elaborated in Chapters 3 and 4.

1.3 Non-equilibrium dynamics in cold atomic gases

Systems in equilibrium are usually studied with the MF approximation in theory and with various macroscopic observables in experiments. However systems away from equilibrium are often less explored especially for quantum non-equilibrium systems where there are limited tools for analyzing the dynamics. For a closed quantum system out of equilibrium, people are particularly interested in questions like the mechanism for the system to reach the steady state and the timescale for thermalization after a quantum quench, the universality in the dynamics, and the integrability of the system, etc [71]. The understanding of these questions are not only of fundamental interests in fields like condensed matter physics [72, 73], quantum statistical physics [74], high-energy physics [75, 76] and cosmology [77, 78], but are also important for applications like quantum information and quantum computing [71, 79]. For example, quantum computers manipulate such interacting quantum system in real time so the dynamical processes always get involved. Cold atomic gases are ideal systems to study some of these questions due to many of their advantages. Such systems can usually be isolated from the environment. The coherence time during dynamical evolutions of dilute gases is usually long enough (a few milliseconds or longer). There are many tunable parameters to prepare the system far from equilibrium and versatile probing methods. Therefore versatile non-equilibrium dynamics has been investigated in the cold atomic gases, e.g. quantum quench dynamics [8, 11, 67, 71, 80, 81], floquet dynamics [82–86], and dissipative dynamics [87–91], etc. Spinor quantum gases, in combination with tools like optical lattices and microwave dressing fields, are even superior in some of those aspects mentioned above. The non-equilibrium spin-mixing dynamics in spinor Bose gases are usually associated with interchanges of different spin species, spin domain formation, and phase transitions [8].

One topic of non-equilibrium dynamics in spinor Bose gases that was early investigated is the coherent spin-mixing dynamics by preparing the initial state away from the ground state.

This includes the microscopic case with a pair of $F = 1$ atoms oscillating between the Fock state $|0, 2, 0\rangle$ and $|1, 0, 1\rangle$ [45, 92], and in the macroscopic collections of atoms [19, 32]. The former can be explained using a Rabi-type model and the latter is appropriately analyzed with a pendulumlike model with MF approximation [8]. An analytical solution of the spin-mixing dynamics considering the exact energy spectrum of the system with the SMA has also been theoretically obtained [31, 93]. Based on Eq. 1.11, the frequency of the ρ_0 oscillation is determined by energy gap between states with total spin number F_{tot} and $F_{\text{tot}} - 2$, i.e. $f = \frac{c_2 n}{2\hbar N}(4F_{\text{tot}} - 2)$ [8]. This result agrees with both the two-atom Rabi-type model and the pendulumlike model for near the ferromagnetic initial state with $F_{\text{tot}} = N$. The discrete energy spectrum not only describes the short time oscillations of spin populations but also predicts long time equilibration and quantum recurrences for specific initial states [31, 94]. Some other nonequilibrium phenomena have also been experimentally observed in spinor BECs, i.e. spin domains [95], topological defects [96], and spin-nematic squeezing [97, 98].

Due to the theoretical advances and new experimental capabilities, there are rapidly growing interests in non-equilibrium dynamics considering the quantum quench scenarios [71]. Here the initial state is usually the ground state $|\psi_0\rangle$ for $H_0 = H(t = 0)$, and the Hamiltonian is quenched to $H(t)$ by tuning one or several parameters in the Hamiltonian. This is often related to topics like quantum Kibble-Zurek mechanism [71], dynamical quantum phase transitions [81], thermalization of closed quantum systems [94], and many-body localization [11]. The quantum Kibble-Zurek mechanism is usually related to the scaling law of some observables when the ramp time varies and the system crosses a phase transition point corresponding to a ground state phase transition. The dynamical quantum phase transition for certain Hamiltonian (e.g. the transverse-field Ising model) usually refers to the non-analyticity of the Loschmidt amplitude as a function of time, which is defined as $g = \langle \psi_0 | \psi_0(t) \rangle = \langle \psi_0 | e^{-iHt} | \psi_0 \rangle$ when H is time independent [81]. Studies of thermalization of isolated quantum systems is related to the emergence of the eigenstate thermalization [71]. Many-body localization refers to the localized phase of certain system, which is the only robust mechanism found so far to avoid thermalization of the system [11]. More recent experimental studies in spinor BECs related to these topics include the observations of

dynamical quantum phase transitions in ^{23}Na antiferromagnetic BECs related to both the ground phase diagram and the highest energy level phase diagram [99, 100], the emergence of the quantum Kibble-Zurek mechanism in ^{87}Rb BECs across a second order polar to broken-axisymmetry phase transition [80], and in ^{23}Na BECs across a first order polar to antiferromagnetic phase transition. Evidences of many-body localized phase and transitions to thermal phases have been reported in Ref. [101] using ^{87}Rb in a two-dimensional disordered optical lattice.

1.4 Outline

This dissertation has five more chapters in addition to this introduction chapter. In Chapter-II, I will briefly introduce our experimental procedures for creating and detecting spinor BECs. I will also introduce the constructions and calibrations of optical lattices and microwave dressing fields.

Chapter-III will discuss the spin-mixing dynamics of BECs confined in deep lattices. The well-established theory and experimental results of this topic are introduced first. Then I will explain our experimental sequences and the intricate spin dynamics observed in our system. Our experiment agrees well with the theory and we are able to confirm atom number distributions of a lattice-confined inhomogeneous system in the MI phase.

Chapter-IV will focus on the spin dynamics after a quantum quench through the phase transition point from the superfluid phase to the Mott-insulator phase. The complicated spin-mixing dynamics enable us to precisely measure a key parameter in spinor physics, U_2/U_0 , the ratio of the spin-dependent and spin-independent interactions. Our work conducted the first experimental study on few-body spin dynamics, which provides transitions between the well-studied two-body and many-body dynamics in antiferromagnetic spinor BECs. The similarity and difference between this experimental sequence and the one in chapter-III will be discussed. I will also review some studies on the universality during the non-equilibrium dynamics, especially the scaling law for a quench across a phase transition. Topics related to the thermalization and equilibration is discussed in the end.

In chapter-V I will introduce the optical superlattice setup in our lab. Such a system is promising for applications in quantum information processing. I will introduce some generic methods developed recently to realize atom entanglement.

In the last chapter, I will discuss a couple of future research directions related to the spinor BECs in optical lattices. Applications of the entanglement in lattice-confined cold atoms are discussed, including quantum computing and magnetometry.

CHAPTER II

EXPERIMENTAL SETUPS AND PROCEDURES

This chapter describes our apparatus for creating lattice-confined sodium spinor BECs and relevant experimental techniques. Two papers related to these topics were published:

- J. Jiang, L. Zhao, S.-T. Wang, Z. Chen, T. Tang, L.-M. Duan, and Y. Liu, *First-order superfluid-to-Mott-insulator phase transitions in spinor condensates*, Phys. Rev. A **93**, 063607 (2016). Included in Appendix B.
- L. Zhao, T. Tang, Z. Chen, and Y. Liu, *Lattice-induced rapid formation of spin singlets in spin-1 spinor condensates*, arXiv:1801.00773. Included in Appendix C.

Lattice-confined cold atoms, as a highly controllable system, have been applied to simulate models in condensed matter physics, quantum statistical physics [74], cosmology [77, 78], and quantum information [7–9]. In this chapter, I will describe our experimental BEC apparatus and the setup of cubic optical lattices. I will also introduce the controls and calibrations of some frequently used tools in our experiments.

2.1 Experimental setups

Figure 2.1 shows our sodium spinor BEC apparatus, same as what is described in our previous work [102]. The whole vacuum apparatus leads to a 10^{-12} torr ultra-high vacuum in the main chamber, which is essential for creating a BEC with a lifetime longer than 10 s. Hot sodium atoms at an initial temperature around 310 K are created in the sodium oven. Hot atoms are first slowed down through the Zeeman slower via Doppler cooling

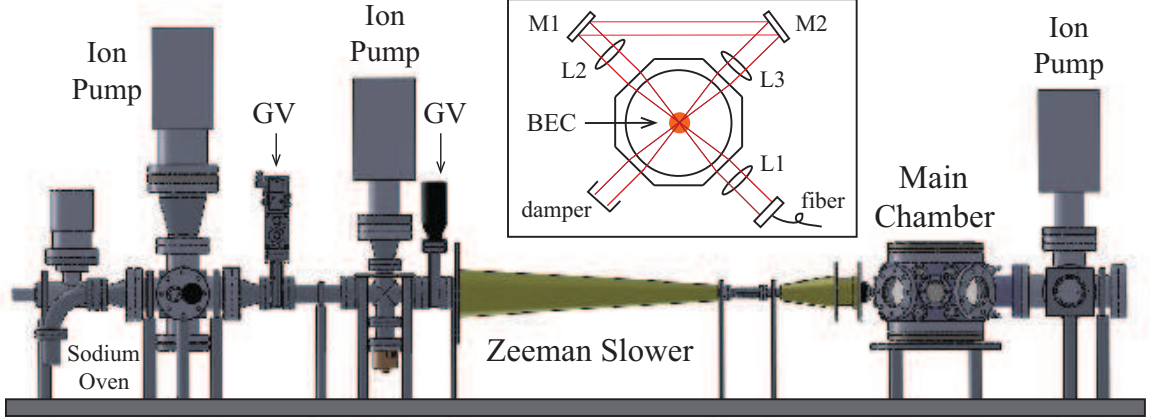


Figure 2.1: Schematics of our BEC apparatus including vacuum pumps, a sodium oven, a Zeeman slower, and a main vacuum chamber. Inset: the setup of a crossed optical trap.

that uses the inhomogeneous magnetic fields for compensation to keep the laser beam on resonant. Slowed atoms then enter the main chamber and get captured by a magneto-optical trap (MOT). There is a pair of MOT coils to generate the magnetic quadrupole field that provides a position dependent force to trap atoms at the center. Three pairs of counter-propagating cooling laser beams provide a force opposite to the direction of atom movement to further cool down atoms, and each of them is detuned by $\delta_{\text{cooling}} = -20$ MHz from the cycling transition. Correspondingly there are six MOT repumping beams and each of the repumping beams is detuned by $\delta_{\text{repump}} = -5$ MHz from the $|F' = 1\rangle$ to $|F' = 2\rangle$ transition, keeping the cooling cycle running. After the MOT loading process, a polarization gradient cooling process helps further cool atoms down to $\sim 40 \mu\text{K}$. The final evaporative cooling process is conducted by applying a crossed optical dipole trap (ODT) then gradually reducing the depth of it. This ODT consists of two high-power far-detuned linearly polarized beams at 1064 nm. A pure $F = 1$ sodium BEC containing up to 1.5×10^5 atoms can be created through this all-optical BEC formation procedure. By applying a weak magnetic field gradient during the first half of the forced evaporation, atoms can be fully polarized to the certain spin state we desire.

Our three-dimensional optical lattice is constructed by three standing waves along orthogonal directions. The lattice beams are originated from a single-mode laser at 1064 nm so lattice spacing is 532 nm, and each beam is frequency-shifted by at least 20 MHz with re-

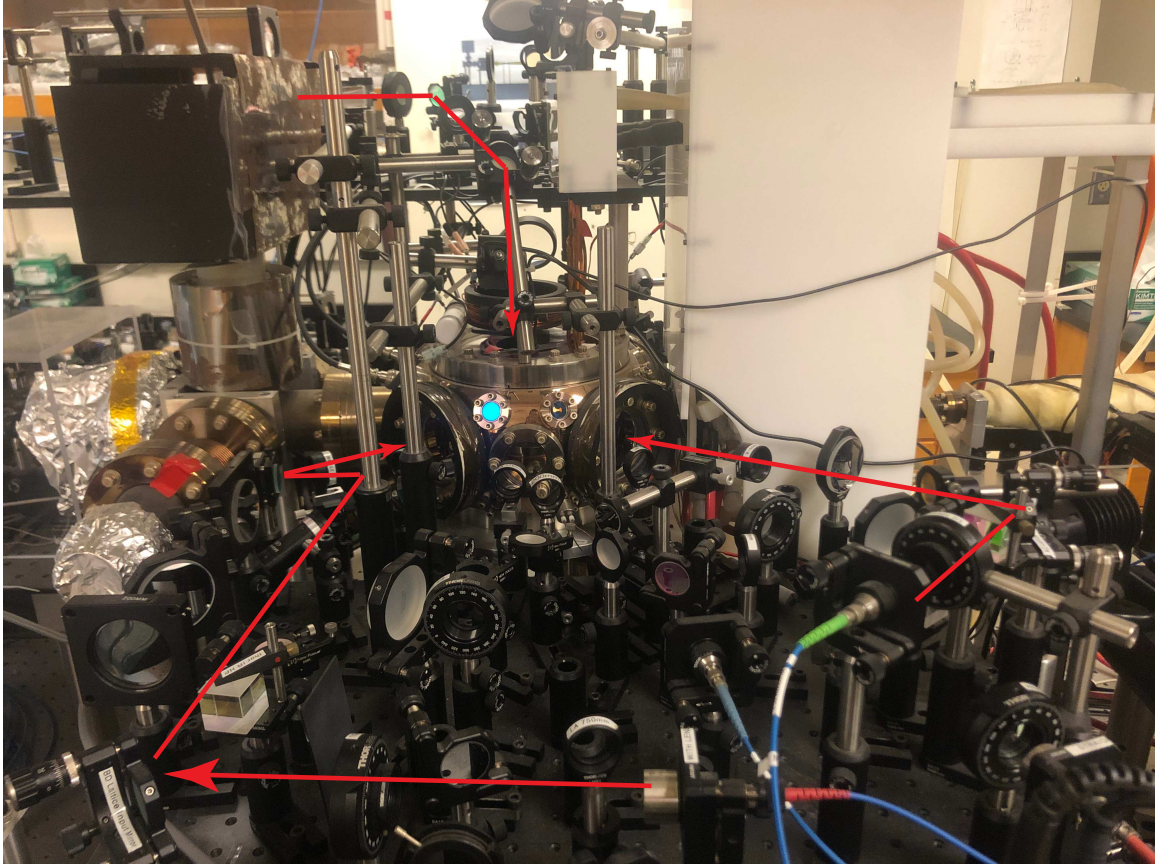


Figure 2.2: Optical layouts of our cubic optical lattices.

spect to each other. Figure 2.2 shows the optical setup of the optics for three lattice beams. After getting out the single-mode fiber, each lattice beam passes through a polarizing beam-splitter to purify the polarization then through a lens mounted on translation stage to get focused. Mirrors for retro-reflecting beams are on the opposite side of the vacuum chamber.

2.2 Experimental procedures

Daily calibrations and precise control are necessary for our system to perform at a desired status. Here I choose to introduce the three most frequently used techniques in our experiments.

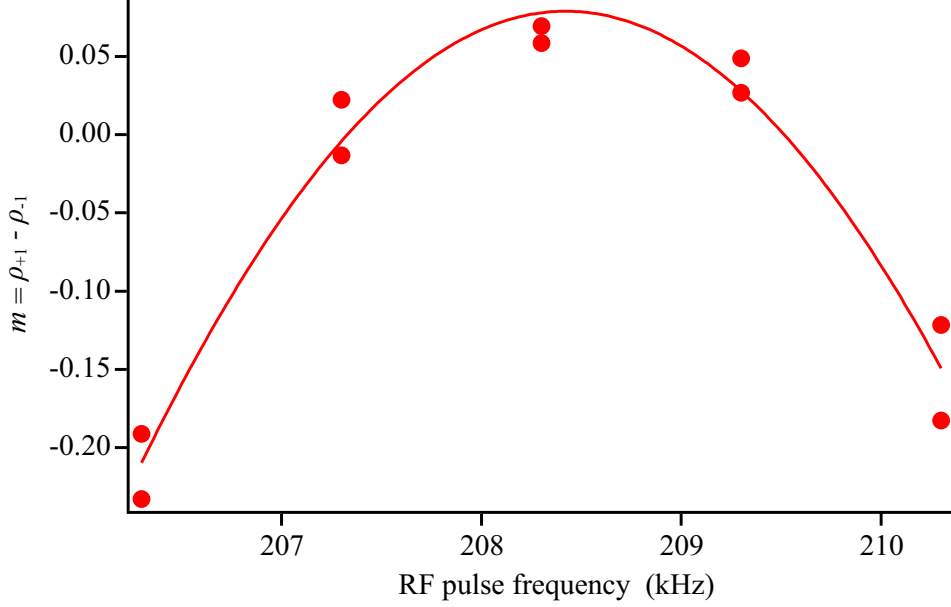


Figure 2.3: The magnetization versus the frequency of an applied RF pulse, which couples $F = 1$ hyperfine states, at a fixed pulse duration. The solid line is a Gaussian fit.

2.2.1 Magnetic field calibrations

Magnetic field always exists in our system since we do not block the Earth's magnetic field. The external magnetic field is generated by three pairs of Helmholtz coils in three orthogonal directions, their currents are controlled by our Labview program [25]. To find the exact settings for a certain quadratic Zeeman energy q_B , we simply use the linear Zeeman energy and the quadratic Zeeman energy for sodium to find the relationship $\Delta E = h\nu = 700h\sqrt{\frac{q/h}{277 \times 10^{-6}\text{Hz}^{-1}}}$, where E is the energy splitting between adjacent $F = 1$ Zeeman states and ν is the frequency of the resonant radio-frequency (RF) pulse. Thus we can find q if we have ν and vice versa. During the experiment, we prepare a pure $|F = 1, m_F = -1\rangle$ state, monitor $m = \rho_{+1} - \rho_{-1}$ versus the RF pulse frequency, then the peak position of a Gaussian fit yields ν . A numerical example is shown in Fig. 2.3, which indicates $\nu = 208.42(5)$ kHz and thus $q/h = 24.56(1)\text{Hz}$. Inversely, we can keep ν fixed and find its corresponding q_B by scanning the current of magnetic coils.

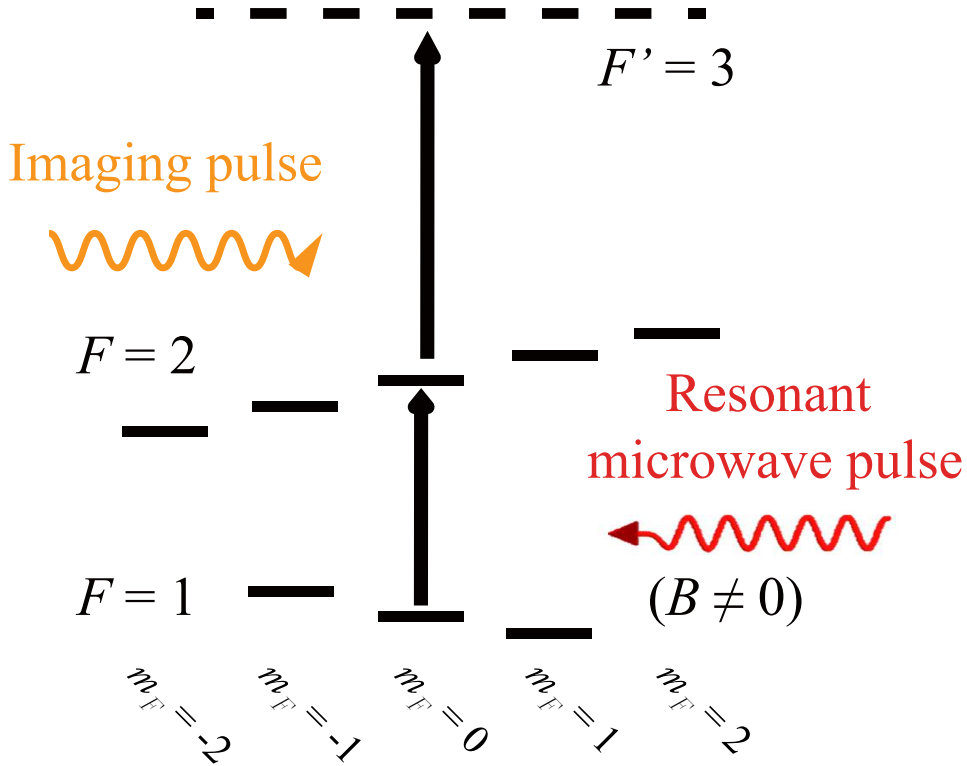


Figure 2.4: Schematic of the two-stage microwave imaging method.

2.2.2 Microwave imaging and microwave dressing field calibrations

In our experiments, the Stern-Gerlach (S-G) absorption imaging and the microwave imaging are applied to detect ρ_0 , the fractional population of the spin-0 atoms. For the S-G imaging, a small gradient magnetic field applied during a TOF separates the three spin components. We can fit the three spin components separately and then extract ρ_0 for BECs in superfluid states. However when BECs are in the Mott-insulator state, the three broad peaks are hard to be well separated by the gradient field. And the number loss due to induced heating leads to a smaller signal to noise ratio and is unfavorable for extracting the experimental signature. We develop a two-step microwave imaging to overcome this problem, as shown in Fig. 2.4. We first apply a microwave pulse resonant with the $|F = 1, m_F = 0\rangle$ to $|F = 2, m_F = 0\rangle$ transition and use the first imaging light resonant with the $F = 2$ and $F' = 3$ transition to count the number of atoms in the $m_F = 0$ level. We then count all remaining atoms with the second imaging light. The total number of atoms is the sum of

the detected atoms from the two imaging processes.

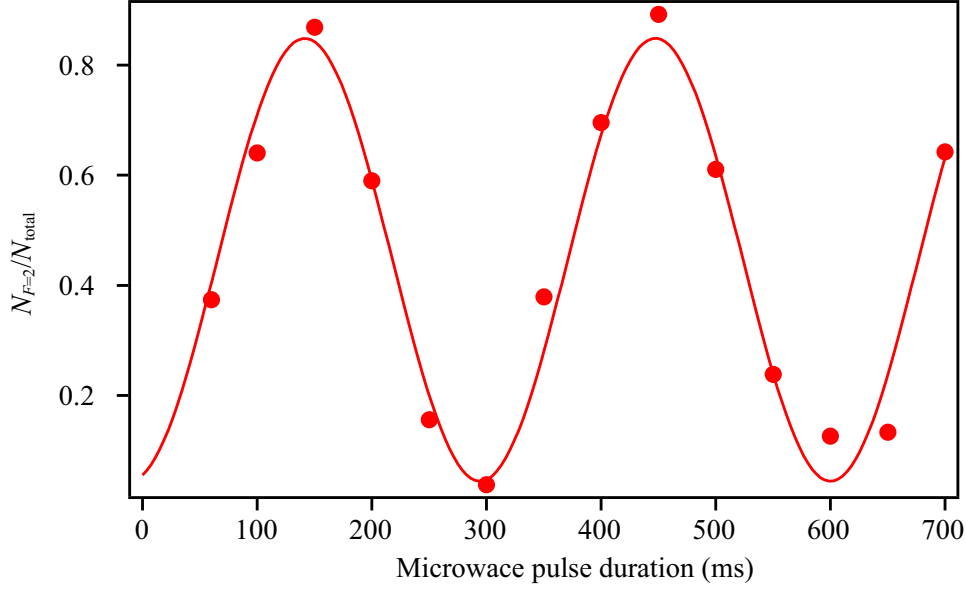


Figure 2.5: The Rabi oscillation of atoms excited to the $F = 2$ state. The on-resonance Rabi frequency is extracted by a sinusoidal fit as the solid line shows.

We have two sets of microwave antennas and microwave function generators in our system, so one is used for the two-stage imaging and the other one for generating the dressing field. The frequency of the function generator can be controlled to either quickly switch between two values or gradually ramp following the settings. The first case is useful when for example, we first set the two frequencies resonant with the $|F = 1, m_F = -1\rangle \rightarrow |F = 2, m_F = 0\rangle$ and $|F = 1, m_F = 1\rangle \rightarrow |F = 2, m_F = 0\rangle$ transitions respectively to pump and remove these atoms for creating a pure $|F = 1, m_F = 0\rangle$ initial state, then the frequencies are quickly switched to the desired values to serve as the dressing field or the two-stage imaging pulse, respectively. The second case allows us to continuously sweep the quadratic Zeeman energy q through the whole range [22].

To find the resonant microwave frequency at a given q , we use Eq. (1.1) and Eq. (1.2) together with the measured Rabi frequencies of the nine transitions between the hyperfine states in $F = 1$ and $F = 2$. Figure 2.5 shows the calibration of the Rabi frequency for one of the nine transitions. With the similar two-stage imaging method we can monitor the fraction of atoms excited to the $F = 2$, therefore this method is independent of atom number fluctuations. To find the exact microwave frequency for $q/h = 0$ Hz, BECs are

prepared at the LP ($\rho_0 = 1$) or TP ($\rho_0 = 0$) state with $m = 0$. Then q is quenched around 0 Hz. If $q/h > 0$, the LP state is the ground state so ρ_0 stays at 1 while the TP state is not stable so ρ_0 changes. If $q/h < 0$, then the TP state is stable and the LP state can not maintain. $q/h = 0$ Hz is where the phase transition happens. One thing worth noting is that when for example a LP state is prepared while q/h is quenched to a negative value, it is necessary to hold the BEC for a while before ρ_0 starts to evolve. This is related to the "freeze-out" property for non-adiabatic phase transitions and the quantum Kibble-Zurek mechanism [33, 103].

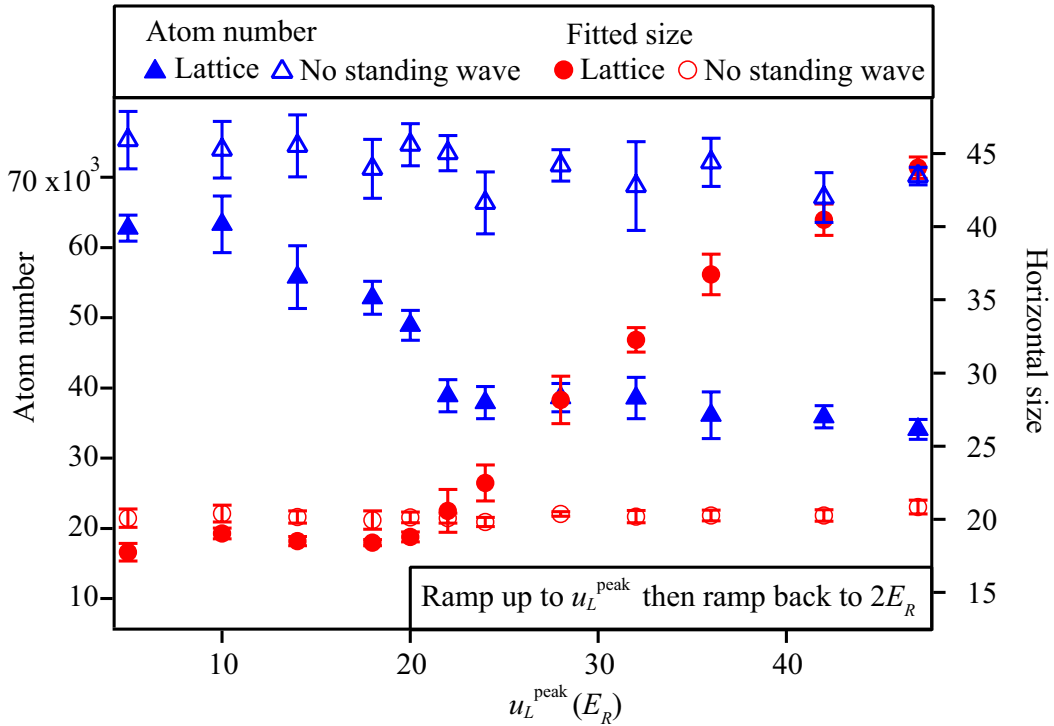


Figure 2.6: The atom number (blue) and fitted size (red) after a ramp-up and ramp-back sequence using optical lattices (solid markers) or optical traps (open markers).

$F = 1$ sodium BECs usually have long lifetimes up to tens of seconds [102, 104]. But it is worth noting that microwave pulses combined with deep optical lattices could induce significant heating and number losses. We monitor the atom number and fitted size after such a sequence: the lattice depth linearly ramps up to u_L^{peak} then ramps back to $2E_R$ at a certain ramp speed, the microwave dressing field is applied during the lattice ramp with a detuning $\Delta = 11$ kHz from the $|F = 1, m_F = 0\rangle \rightarrow |F = 2, m_F = 0\rangle$ transition. There

are obvious number loss and heating indicated by the increase of the fitted size, as shown in Fig. 2.6. In a contrast experiment we rotate the polarization of the three retro-reflected beams by $\pi/2$ so the laser beams, without interfering with each other, only provide trapping potentials. Open markers in Fig. 2.6 show the results of this contrast experiment, which indicates no obvious number loss or heating. The microwave-induced number loss can be explained by the fact that the microwave frequency is close to the $|F = 1\rangle \rightarrow |F = 2\rangle$ transition and sodium atoms at the $F = 2$ state decay rapidly [23]. The lattice-enhanced atom density could have enlarged the microwave-induced atom losses.

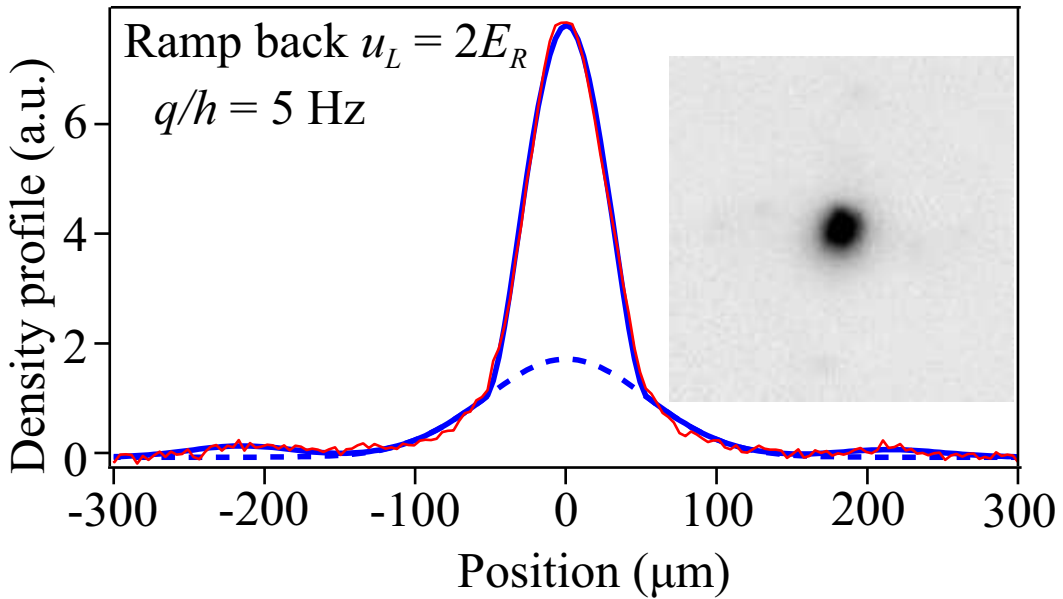


Figure 2.7: The red line is the density profile integrating over a certain region of the picture along one direction. The blue solid (dashed) line represents the fit for the condensate (thermal) part. The condensate fraction can then be extracted from such a bimodal fit. Inset: a TOF picture at $q/h = 5$ Hz after a ramp-up then ramp-down sequence to $2E_R$.

We further investigated this process by extracting the condensate fraction of a BEC after a lattice ramp-back sequence with the microwave pulse set at different frequencies. A bimodal fit is applied to extract the condensate fraction, as shown in Fig. 2.7. The value of condensate fraction can be used to extract the BEC temperature around the transition point T_c . When $T > T_c$ the condensate fraction is around 0, and when T gets smaller than T_c , the value quickly increases to around 1. We found the heating effect strongly depended on the frequency detuning Δ , i.e., the condensate fraction decreases when Δ gets smaller,

indicating there are more heating. Although we have not been able to analytically describe this process, it is clear that an off-resonant microwave pulses together with deep lattices can introduce severe heating. Therefore designing an experimental sequence using microwave dressing fields and high power optical lattice beams needs to take this problem into account.

2.2.3 Lattice calibrations via Kapitza-Dirac diffraction patterns

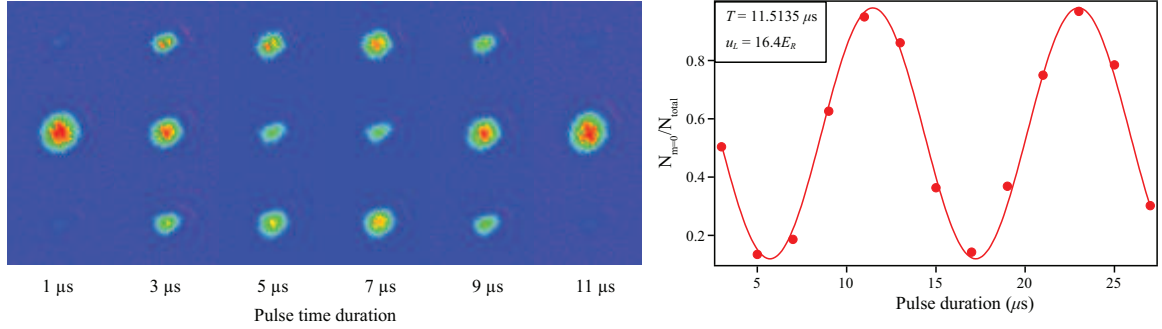


Figure 2.8: Left: typical Kapitza-Dirac diffraction patterns with a single lattice beam pulsing on BECs when $u_L = 16.4E_R$. The fractional population of the zero-momentum ($p = 0$) component oscillates with the pulse duration. Right: a sinusoidal fit is applied to extract the oscillation frequency and hence the lattice depth u_L .

For a given lattice beam with a fixed power and waist, the lattice depth can be directly calculated from Eq. [3.4]. But this method turns out to be unreliable due to some technical problems, such as imperfect lattice alignments and an attenuated retro-reflected beam. On the other hand, Kapitza-Dirac (K-D) diffraction patterns provide an easy and direct way to calibrate the lattice depth. Like what is discussed in [105], pulsing on a single lattice beam for a variable amount of time τ gives a time-dependent diffraction pattern. When we suddenly load a BEC into a lattice and then suddenly release it, the wave function (initially can be treated as a plane wave with $\mathbf{p} = 0$) is first projected into the Bloch states as the sum of $|n, 0\rangle$: $|\Psi(t = 0)\rangle = \sum_{n=0}^{\infty} |n, 0\rangle \langle n, 0 | \phi_0\rangle$. During the pulse time τ , each band n has its phase factor evolving at $\exp\{-iE_n(q=0)\tau/\hbar\}$, where $E_{n,0}$ is the energy at the n band. And then the final state after the TOF measurement is the projection back into the plane wave basis. Calculation shows the interference of these phase factors cause the oscillation of populations for each plane wave $\phi_{2m\hbar k_L}$ ($m = 0, \pm 1, \pm 2\dots$) with the corresponding coefficient $b_0(m) = \sum_{n=0}^{\infty} a_{n,0}^*(0) a_{n,0}(m) \exp\{-iE_n(0)\tau/\hbar\}$, where $\langle n, 0 | \phi_0\rangle = a_{n,0}^*(0)$. [105].

Figure 2.8 shows an example of the oscillation of atoms between zero momentum $p = 0$ and $p = 2\hbar k$ at a certain u_L . When u_L is shallow enough ($< 20E_R$), only $n = 0$ and $n = 2$ bands need to be considered and atoms oscillate sinusoidally at the frequency of $(E_{0,0} - E_{2,0})/h$. Based on the extracted oscillation frequency and the predicted $E_{n,0}$, we can find u_L at a certain laser power, as shown in Fig 2.8 where the calibrated $u_L = 16.4E_R$. We then repeat the above step at one or two different laser powers to find the coefficient power divided by lattice depth, as u_L linearly depends on the laser power.

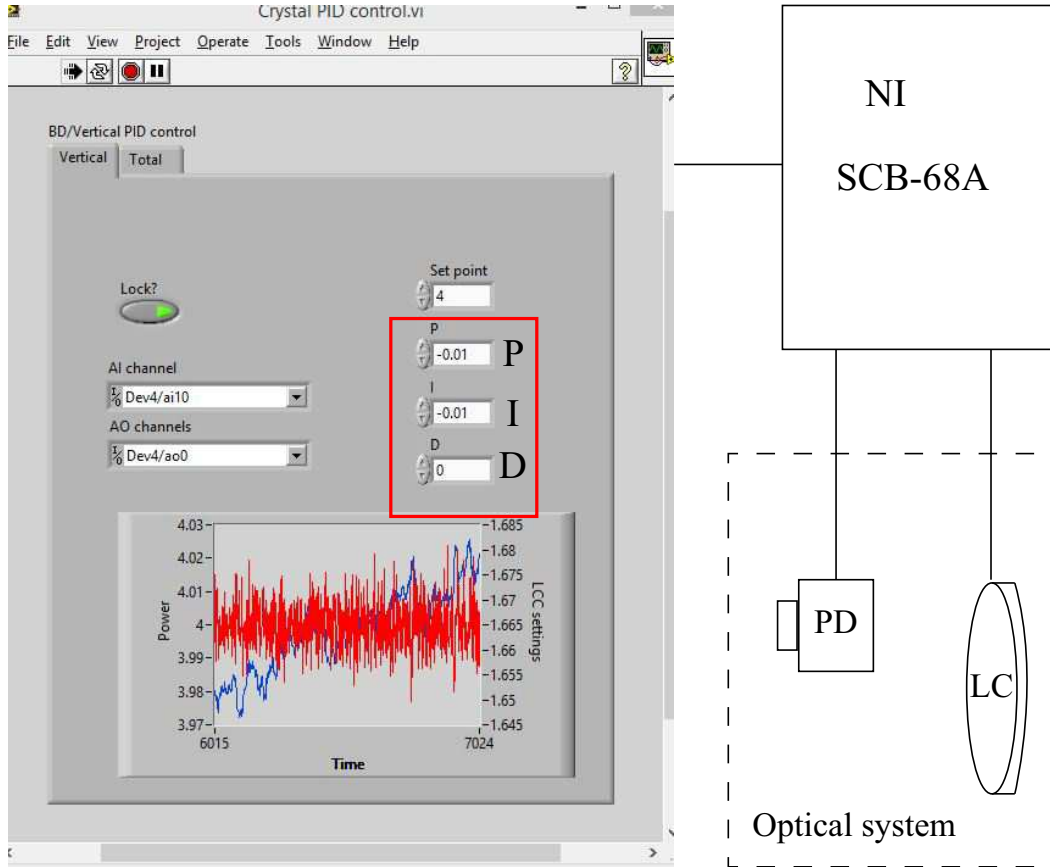


Figure 2.9: Schematic of our feedback control system to stabilize the lattice beam power.

The lattice power fluctuations lead to errors in the lattice depth calibration. Each lattice beam has been controlled independently with a feed-back servo loop, as shown in Fig. 2.9. The photo-detectors (PD) monitors the power and a feedback signal is generated through our Labview PID program. The input and output signals are processed by a DAQ Multifunction I/O Accessory (NI SCB-68A). The output signal goes to the half-wave liquid crystal (LC) wave plates that can stabilize the lattice power by slowly varying the polarization state.

The systematic error of our lattice calibration is $6\% \sim 7\%$. A lattice ramp is realized by altering the input signal of an acousto-optics modulator (AOM) in each lattice beam path.

CHAPTER III

DYNAMICS OF SPINOR BECS IN DEEP LATTICES

This chapter discusses our experimental studies on the spin-mixing dynamics of spinor BECs in cubic optical lattices when the initial state is prepared far from the equilibrium states. One paper related to these topics was published:

- Z. Chen, T. Tang, J. Austin, Z. Shaw, L. Zhao, and Y. Liu, *Quantum Quench and non-equilibrium Dynamics in Lattice-Confined Spinor Condensates*, Phys. Rev. Lett **123**, 113002 (2019). Included in Appendix A.

As mentioned in the introduction, cold atom systems are ideal system for the study of non-equilibrium dynamics for many reasons. There are many state preparation techniques and difference kinds of methods for measurements. Such a system can be easily prepared far away from equilibrium through quenching one of its highly-controllable parameters, e.g., the number of atoms, temperature, total spin of the system, the dimensionality of the system, or the lattice potential when it is combined with optical lattices [8, 22, 25, 27, 46, 94, 106, 106–108]. In lattice-confined spinor gases, interesting dynamics have been investigated by preparing non-equilibrium initial states. Dynamics in different dimensional systems also have interesting differences, for example in 1D Ising spin chains interaction-driven revival dynamics were observed [109], in 2D lattices the dynamics and equilibration of spin-mixing process were studied [25], and coherent spin-mixing dynamics of tightly confined atom pairs existed in cubic lattices [45, 92]. The long equilibration time of spinor systems, ranging from tens of milliseconds to several seconds [8, 25], is another notable advantage of investigating non-equilibrium dynamics. This chapter will mainly focus on the coherent spin-mixing

dynamics in the MI phase after the initial state is prepared far-away from the ground state via quenching the magnetic field strength. No phase transition point is crossed during this quench sequence, so this is a simple and clean experiment with no complicated phenomena induced by a symmetry breaking. I will introduce our experimental sequences based on the system discussed above. Then I will discuss the important observations related to the many-particle spin oscillations.

3.1 Spin dynamics in two extremes

The spin-mixing dynamics in spinor gases are related to the spin exchanging collisions between a pair of atoms. Two $|F = 1, m_F = \pm 0\rangle$ atoms become one $|F = 1, m_F = +1\rangle$ and one $|F = 1, m_F = -1\rangle$ and vice versa. The linear Zeeman energy remains the same during the process and we usually only consider the quadratic Zeeman energy q , which can be manipulated by changing the external magnetic fields or applying a microwave dressing fields. The competition between q and spin-dependent interactions c_2 determines the nature of the spin dynamics[8]. Experimental studies on non-equilibrium dynamics have been conducted in spinor gases extensively at two extremes. Ref. [45, 92] mainly focused on the dynamics in a clean two-body system isolated in a lattice site when the system is in the Mott-insulator phase, and many other works investigated a many-body system with more than 10^4 atoms in the superfluid (SF) phase [8, 25, 27, 106]. But transitions between these two extremes remain less explored [46].

3.1.1 Single spatial mode approximation

The coherent spin dynamics of BECs in optical trap have been well studied both theoretically and experimentally [19, 20, 27, 32, 110, 111]. To limit discussions within the spin degree of freedom, the single-spatial-mode approximation (SMA) is usually considered. This requires the size of BECs smaller than the spin healing length. The condensate wave function

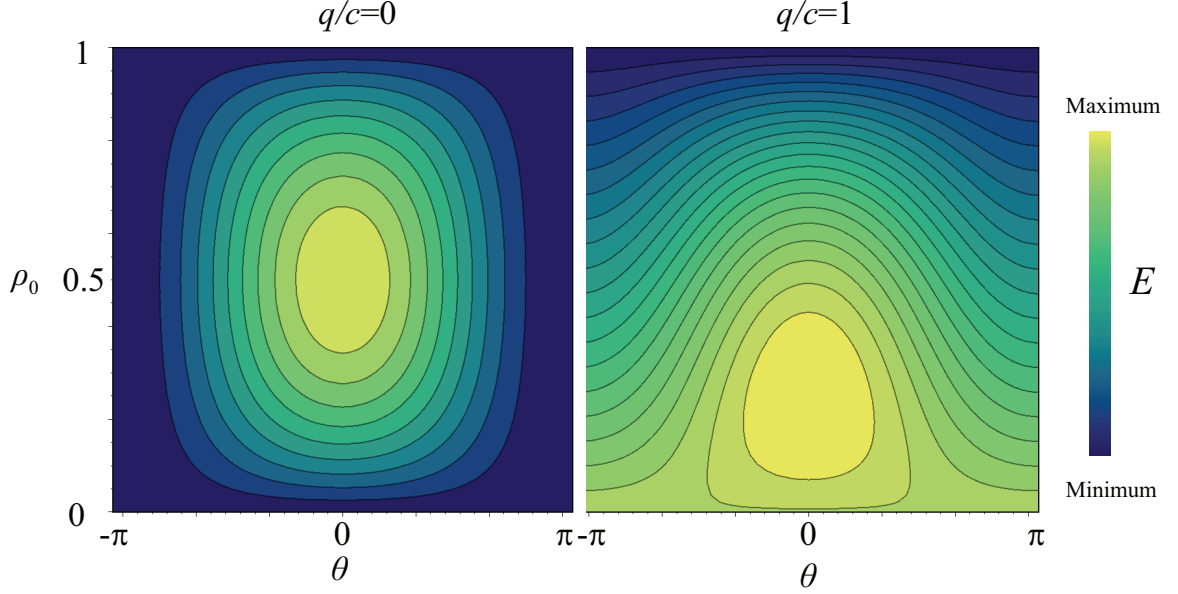


Figure 3.1: Equal-energy plots based on Eq. 3.2 with $m = 0$, $q/c = 0$ (left) and 1 (right). The spin-mixing dynamics evolve along the equal-energy contours.

under SMA can be written as [25]

$$\Phi_{m_F}(\mathbf{r}) = \Psi(\mathbf{r})\psi_{m_F}e^{-\frac{iE_{m_F}t}{\hbar}}, \quad (3.1)$$

where the spacial mode $\Psi(\mathbf{r})$ is fixed and the spin state varies as the rest terms indicate. The spin population fraction for m_F state is $\rho_0 = |\psi_{m_F}|^2$. ψ_{m_F} can thus be expressed as $\psi_{m_F} = \sqrt{\rho_{m_F}}\exp(-i\theta_{m_F})$, where θ_{m_F} is the corresponding phase. With the conservation of both total atom number N and magnetization m , the energy of the system is [8, 32]

$$E = q(1 - \rho_0) + c\rho_0[(1 - \rho_0) + \sqrt{(1 - \rho_0)^2 - m^2} \cos \theta], \quad (3.2)$$

where $\theta = \theta_{+1} + \theta_{-1} - 2\theta_0$ is the phase difference, $c = c_2n$ is the spin-dependent interaction, n is the density of the condensate. And the equations of motion are $\dot{\rho}_0 = -(2/\hbar)\partial E/\partial\theta$, $\dot{\theta} = (2/\hbar)\partial E/\partial\rho_0$. Figure 3.1 shows the energy plot as a function of ρ_0 and θ with $m = 0$ based on Eq. 3.2. The energy is conserved during the spin-mixing dynamics, and the evolution of ρ_0 and θ is along the equal-energy contours depending on the initial states.

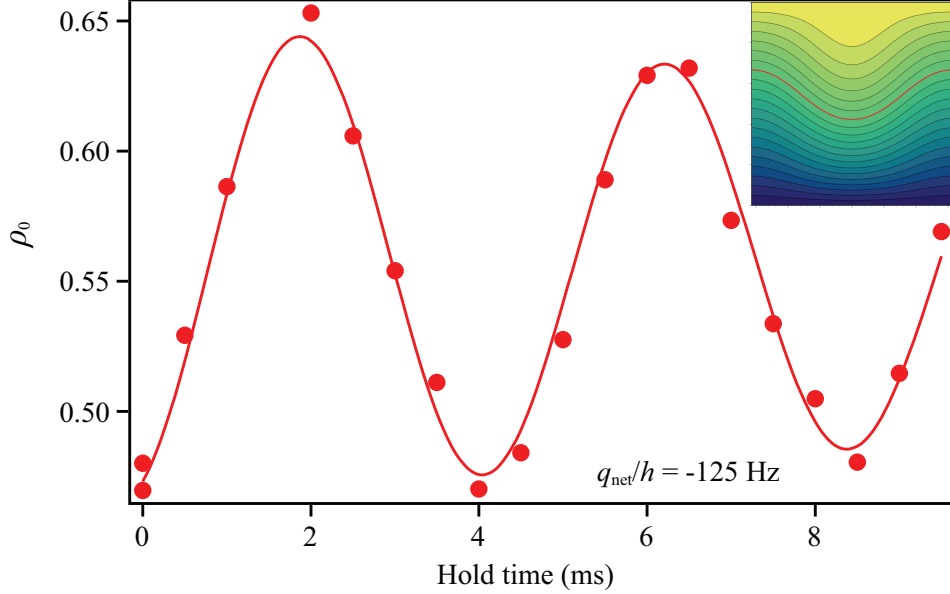


Figure 3.2: A typical spin-mixing dynamics observed at $q = -125$ Hz. Inset shows the equal-energy plots with $m = 0$, $q/c = -2$.

The time evolution of ρ_0 depends on the initial spin state, c and q . It can be seen from Fig. 3.1 and inset of Fig. 3.2 how the value of q changes the constant-energy contours, so does the evolution of the dynamics. The comparison between $|q|$ and $2c$ determines two different dynamical regimes. Large $|q|$ corresponds to the "Zeeman regime" with running phase while the opposite limit is the "interaction regime" where the phase space is divided in two regions by the separatrix $\dot{\rho}_0 = \dot{\theta} = 0$. One region has oscillating phase solutions while the other has running phase solutions. Such spin dynamics have been observed in different atom species [19, 20], and over both positive and negative q [27]. There are also observations of BECs with certain initial conditions crossing the separatrix during the time evolution due to the energy dissipation [112]. Figure 3.2 shows a typical spin oscillation represented by the time evolution of ρ_0 at $q = -125$ Hz. The solid line is a damped sine fit to the data.

3.1.2 Spin-exchanging collisions in few atoms

The simplest case of spin-mixing dynamics happens if we consider there are only two tightly confined $|F = 1\rangle$ atoms satisfying the SMA. For two $m_F = 0$ atoms, the initial state can

be expressed as $|0, 2, 0\rangle$ in Fock basis. The state can also be described under angular-momentum basis $|n, F_{\text{tot}}, M\rangle$ where n is the total number, M is the total spin projection along z axis and F_{tot} is the total spin. Then the initial state for two $m_F = 0$ atoms is a superposition of $F_{\text{tot}} = 0$ and $F_{\text{tot}} = 2$. So the subsequent spin mixing should be a Rabi-type oscillation between these two states, with the frequency and amplitude determined by the energy difference.

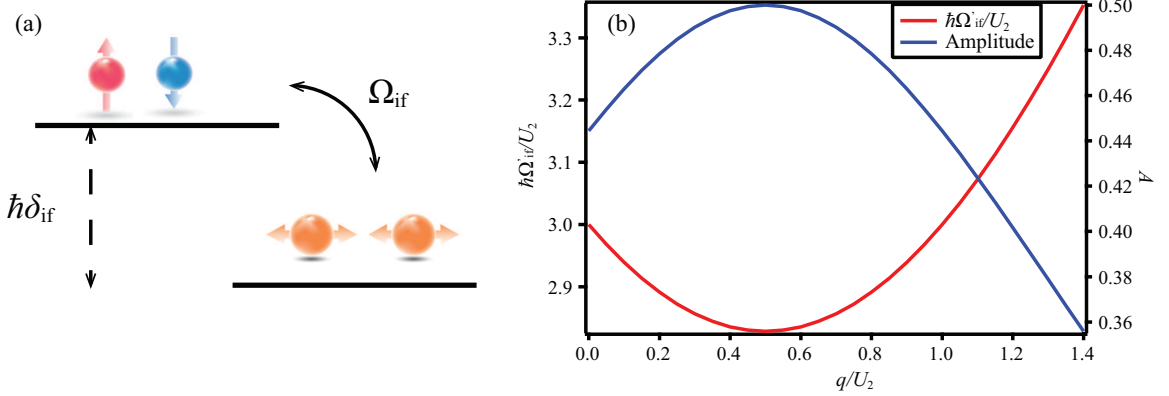


Figure 3.3: (a) Diagram of the spin-changing collisions between two atoms. (b) The calculated oscillation frequency Ω'_{if} and amplitude A as a function of q and U_2 .

Reference [45] studied such two-atom coherent spin dynamics by preparing many ^{87}Rb atom pairs in an optical lattice and initialize the dynamics using ratio-frequency pulses to transfer atoms to one of the $|F = 2\rangle$ hyperfine states. They directly employed a Rabi-like model to describe the dynamics in each site. As Fig. 3.3(a) shows, the system starting from $|0, 2, 0\rangle$ state can only access $|1, 0, 1\rangle$ state. Therefore the transfer matrix can be reduced to [113]

$$H = \frac{\hbar}{2} \begin{pmatrix} 0 & \Omega_{if} \\ \Omega_{if} & 2\delta_{if} \end{pmatrix}, \quad (3.3)$$

where Ω_{if} is the interaction Hamiltonian between the initial and final states, which depends on the spin-dependent interaction U_2 . The detuning δ_{if} is the interaction energy difference of the two states which can be tuned by the quadratic Zeeman energy as $\delta_{if} = \delta_0 + \delta(B^2)$. The transition probability can be expressed as $P_f = \frac{\Omega_{if}^2}{\Omega_{if}'^2} \frac{1}{2} [1 - \cos(\Omega_{if}' t) e^{-\gamma_{if} t}]$. Here $\Omega_{if}' = \sqrt{\Omega_{if}^2 + \delta_{if}^2}$ is the effective Rabi frequency, and the last exponential is a phenomenological

term with γ_{if} the damping rate. The calculated oscillation frequency Ω'_{if} and amplitude $A = \frac{\Omega_{if}^2}{2\Omega_{if}'}_2$ are shown in Fig. 3.3(b) as a function of q and U_2 . This model explained their experimental data well, as the oscillation of the observed spin component is a simple damped sine wave. The extracted frequencies was used to precisely measure spin-dependent interaction strength and the scattering length differences [92].

3.2 Spin dynamics in an inhomogeneous system

Aforementioned coherent spin-mixing dynamics have been experimentally studied in a clean two-body system and in a many-body system over the past 15 years [8, 27, 45, 106, 114]. Transitions between these two extremes are less explored due to some technique challenges. For example, multiple ^{87}Rb atoms trapped in the same lattice site have short lifetime [45].

In our inhomogeneous system, a large fraction of lattice sites are occupied by more than 2 atoms, which enables us to study transitions between two-body and many-body spin dynamics. We observe dynamics consisting of spin-mixing oscillations at multiple frequencies in spinor BECs after the quantum quench sequence. The spin-mixing spectra reveals atom number distributions of an inhomogeneous system indicating a Mott-shell structure. Every observed spin dynamics is well described by summing up multiple Rabi-type spin-mixing oscillations in individual lattice sites. This enables us to precisely measure the ratio of U_0 (the spin-independent interaction) to U_2 (the spin-dependent interaction), an important factor in the spinor physics.

The site-independent Bose-Hubbard model has successfully described lattice-confined spinor BECs [8, 36, 68]. Since our data are taken in deep lattices, we consider the simplified Bose-Hubbard model ignoring the tunnelling energy J [46],

$$H = \frac{U_0}{2}n(n-1) + \frac{U_2}{2}(\vec{S}^2 - 2n) + q(n_1 + n_{-1}) - \mu n . \quad (3.4)$$

$n = \sum_{m_F} n_{m_F}$ is the atom number in each lattice site, m_F stands for the specific spin state. \vec{S} is the spin operator. q is the net quadratic Zeeman energy induced by the magnetic field

and/or a microwave dressing field [36, 46].

3.2.1 Experimental sequences

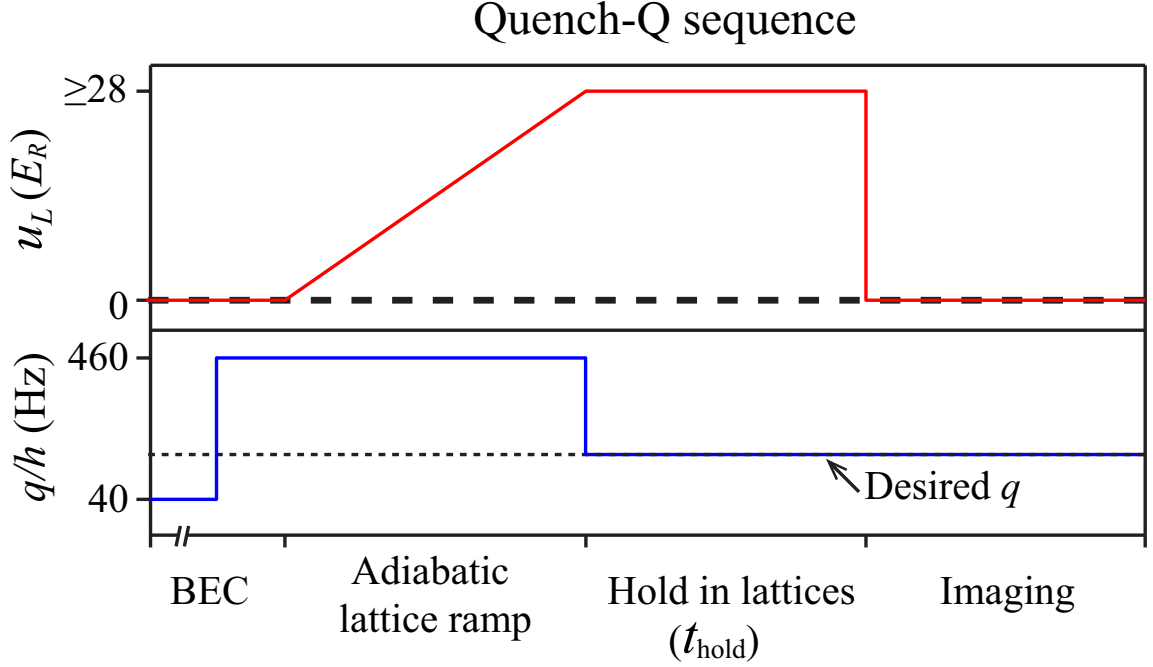


Figure 3.4: Schematic of our Quench-Q sequence (see text). All axes are not to scale. (This figure is adapted from our published work [67].)

Figure 3.4 illustrates the experimental sequence (Quench-Q sequence), used in this work. The sequence starts in free space at $q/h = 40$ Hz with a BEC of up to 10^5 sodium (^{23}Na) atoms. The spin-1 antiferromagnetic spinor BEC is in its ground state for positive q , the longitudinal polar (LP) state with $\rho_0 = 1$ and $m = 0$. As mentioned in the last chapter, we eliminate all $|F = 1, m_F = \pm 1\rangle$ atoms with resonant microwave and laser pulses to prepare a pure $|F = 1, m_F = 0\rangle$ state [36, 68]. Atoms in the LP state are then loaded at a given q into a cubic lattice. We calibrate the lattice depth u_L with Kapitza-Dirac diffraction patterns as mentioned in the last chapter. We first adiabatically ramp up cubic lattices to a final depth of $u_L \geq 28E_R$ in a high field (where $q \gg U_2$). This ensures atoms cross SF-MI transitions and enter into their ground states (where $\rho_0 \simeq 1$) in the MI phase [68]; and we then suddenly quench magnetic fields to a desired smaller q . Since the state with $\rho_0 \simeq 1$ is no longer the ground state, a non-equilibrium dynamics is initialized. Atoms are

held in lattices for a certain time t_{hold} for evolution, then are abruptly released from the lattices for measurement. ρ_0 can be measured with Stern-Gerlach absorption imaging and our two-step microwave imaging after a given time of flight [36].

3.2.2 Spin oscillations at multiple frequencies

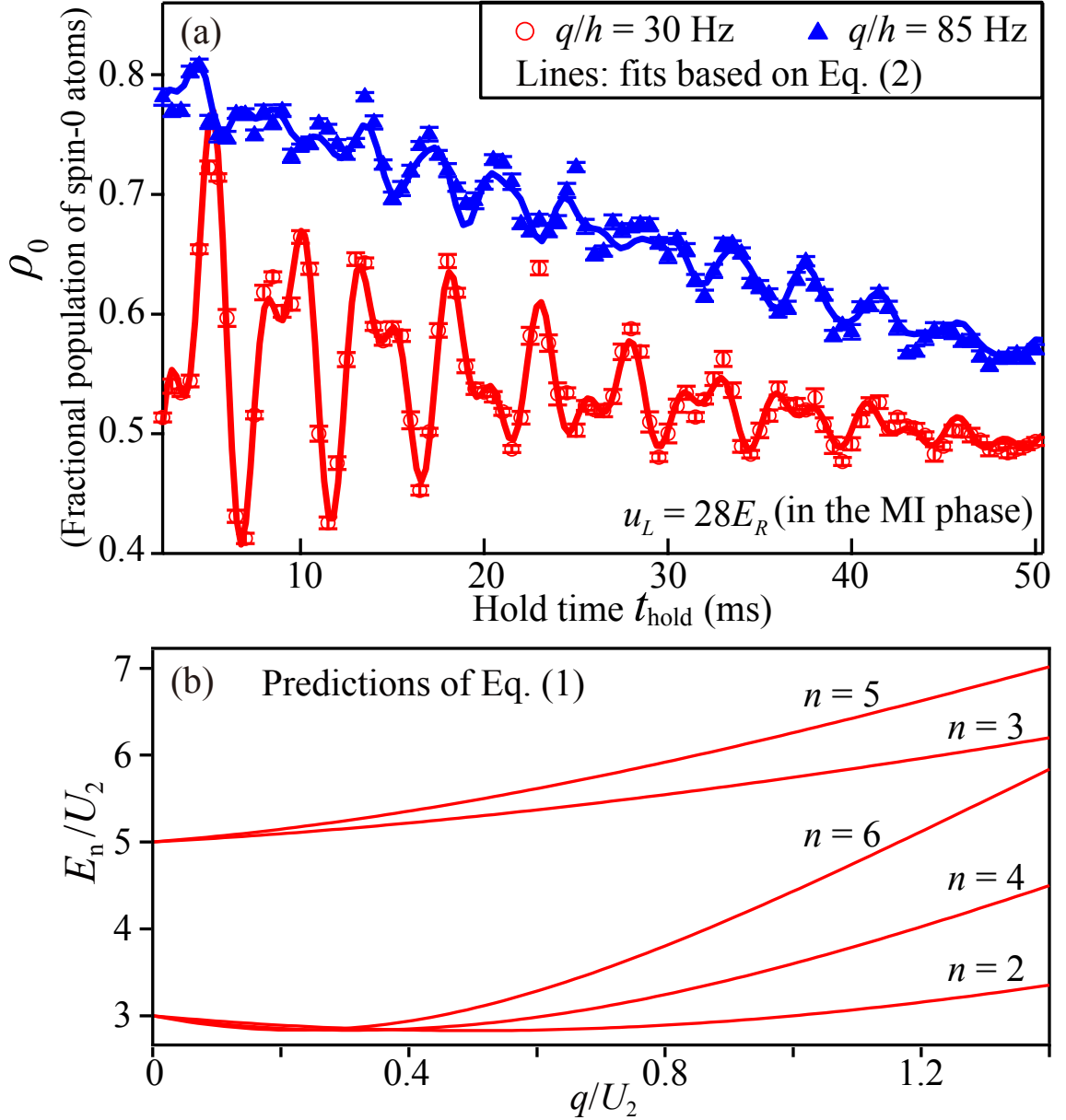


Figure 3.5: (a) Observed spin dynamics after Quench-Q sequences to different q . Lines are fits based on Eq. (3.5). (b) Lines denote the predicted energy $E_n = h \cdot f_n$ (see text). (This figure is adapted from our published work [67].)

Spin-mixing oscillations at multiple frequencies are observed after Quench-Q sequences at $q/h < 100$ Hz. Two typical time evolutions of ρ_0 are shown in Fig. 3.5(a). Each value of ρ_0 presented on the graph is extracted from averaging approximately 15 repeated measurements. All quoted uncertainties of ρ_0 are estimated one standard error. Here we treat the n atoms tightly confined in one lattice site using a Rabi-type oscillation with a fixed frequency f_n . Then the time evolutions occurring in individual lattice sites for our inhomogeneous system get combined together for the observed dynamics.

Here we only consider the two level case, the ground state and the first excited state in the subspace of $m = 0$ at a given n (see Fig. 3.5(b)). Based on Eq. (3.4), the energy gap E_n can be calculated, and $f_n = E_n/h$. Analytical expressions for f_n can be found at $n = 2$ and $n = 3$, i.e., $f_2 = U_2\sqrt{9 - 4(q/U_2) + 4(q/U_2)^2}/h$ and $f_3 = U_2\sqrt{25 + 4(q/U_2) + 4(q/U_2)^2}/h$ [67]. The oscillation amplitude D_n for n atoms in single site can also be derived from Eq. (3.4). The calculated results for $q/h = 85$ Hz are listed in Table 3.1. Then such an evolution appears to be fit by a composition of multiple Rabi-type oscillations (see solid lines in Fig. 3.5(a) and Eq. (3.5)). More detailed discussion of the fitting parameters can be found in the last section of this chapter. One noticeable difference in Fig. 3.5(a) is that the 30 Hz data oscillation is much like an overlapping of two sinusoidal wave but the 85 Hz data are more complicated, although they have the same number distributions. This can be explained by Fig. 3.5(b): when q is small the oscillation frequencies for different n are too close to be separated.

3.3 Spectra analysis and atom number distributions

n	1	2	3	4	5	6
D_n	0	0.413	0.229	0.269	0.215	0.199

Table 3.1: Calculated amplitudes D_n for n atoms in a single site at $q/h = 85$ Hz.

Fast Fourier transformations (FFT) is a good method to analyze signals with multiple frequencies. Therefore we conduct FFT onto all observed time evolutions to better illustrate the spin-mixing dynamics. For the 85 Hz data set in Fig. 3.5(a), typical FFT spectra

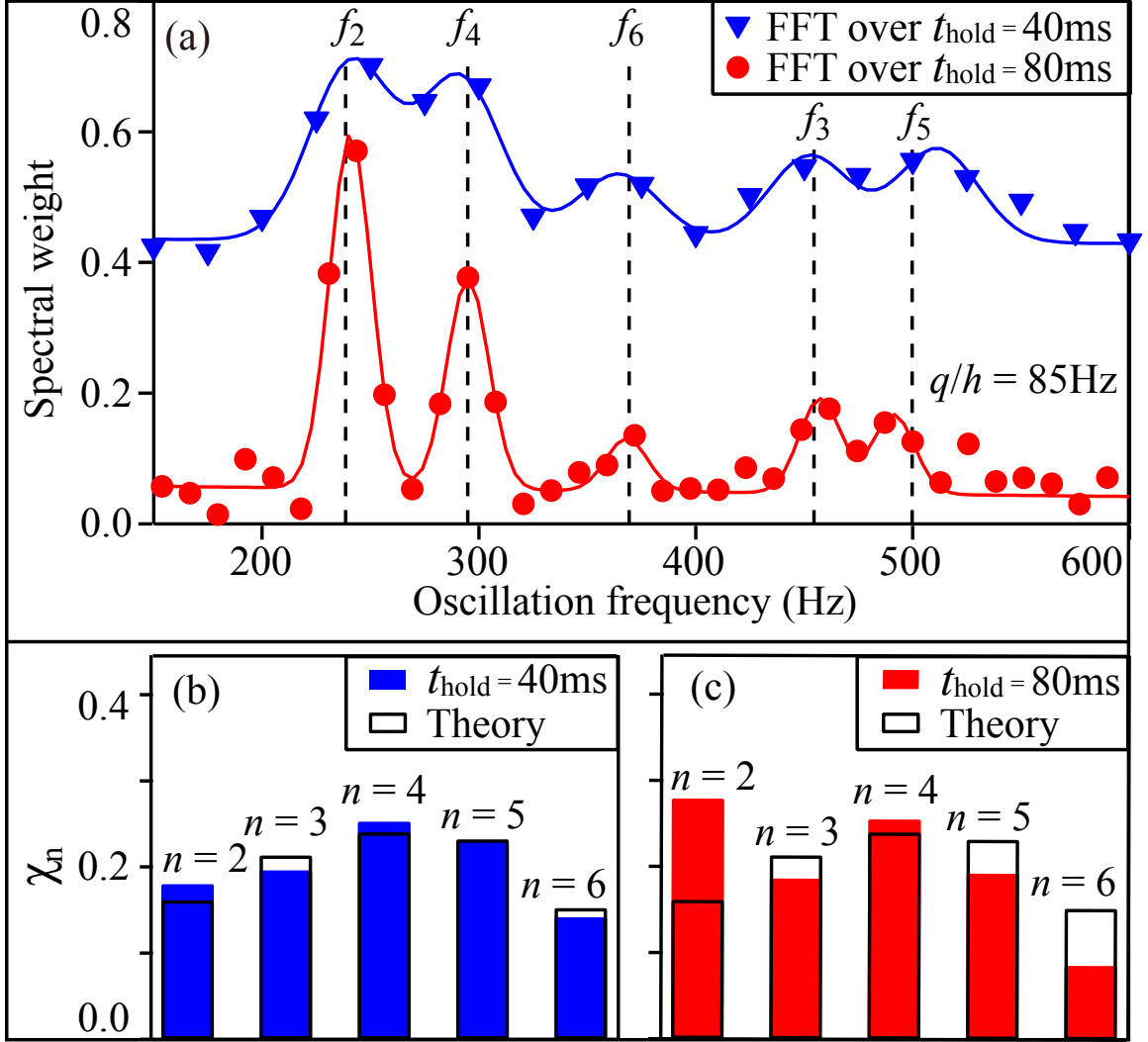


Figure 3.6: (a) Triangles (circles) represent fast Fourier transformations (FFT) over the first 40 ms (80 ms) of t_{hold} on the $q/h = 85\text{Hz}$ data set shown in Fig. 3.5 (a). Vertical lines mark the predicted f_n (see text). Solid lines are five-Gaussian fits. Results obtained at $t_{\text{hold}} = 40\text{ms}$ are shifted up by 0.4 for visual clarity. (b) Atom number distributions extracted from the $t_{\text{hold}} = 40\text{ms}$ FFT spectrum in Panel (a). We define χ_n as the fraction of atoms localized in lattice sites having n atoms, and extract χ_n from dividing the area below the corresponding peak in a FFT spectrum by the spin oscillation amplitude D_n (see text). Black bars mark the predicted χ_n in Mott-insulator shells at $n_{\text{peak}} = 6$ based on Eq. (3.4) and the Thomas-Fermi approximation. (c) Similar to Panel (b) but extracted from the $t_{\text{hold}} = 80\text{ms}$ FFT spectrum in Panel (a). (This figure is adapted from our published work [67].)

extracted over different time durations are shown in Fig. 3.6(a). Each of these two FFT spectra has five distinguished peaks agreeing well with the predictions (the vertical lines) of Eq. (3.4). The spin components in the even Mott lobes oscillate at lower frequencies, which

corresponds to the three peaks between $200 \sim 400$ Hz. Particles in the two odd Mott lobes display higher spin oscillation frequencies when $q/U_2 < 1.55$ like the other two peaks show. Atom number distributions together with the oscillation amplitudes in each individual site determine the observed total amplitude, which is revealed from the FFT spectra. The number distributions can also be extracted from a FFT spectrum, as shown in Figs. 3.6(b) and 3.6(c). The spin oscillation amplitudes D_n for n atoms in a single site is listed in Table. 3.1. The comparison of these two figures indicates the number distributions χ_n in our system quickly change with time t_{hold} and the $n = 2$ Mott lobe becomes more dominating after atoms are held in deep lattices for a longer time. This implies atoms in the $n = 2$ Mott lobe decay more slowly. This is possibly because of the lack of three-body inelastic collisions in this lobe. Another notable result in Fig. 3.6(b) is that each experimental χ_n extracted from the FFT spectrum over a short time duration (i.e., $t_{\text{hold}} = 40$ ms) coincides with the theoretical χ_n at $n_{\text{peak}} = 6$. The theoretical values of χ_n are listed in Table 1.1, derived from Eq. (3.4) and the Thomas-Fermi approximation for Mott-insulator shells. Since the initial states are the ground states of the MI phase, it is reasonable to consider that atoms follow the predicted Mott shell structure during the Quench-Q sequences.

Our data thus experimentally confirm a new approach to probe the initial Fock-state distributions: by analyzing the spin-mixing dynamics and their corresponding FFT spectra over a short t_{hold} after a sufficiently fast quench sequence. Although for small q where the frequencies differences are small, the peaks at multiple frequencies cannot be separated within the t_{hold} used in the experiment. As Fig. 3.7 shows, the $q/h = 30$ Hz FFT spectra has only two distinguished peaks rather than the predicted five peaks, i.e., the wide peaks at around 220 Hz correspond to the oscillations of even n atoms and the wide peaks at around 400 Hz to the oscillations of odd n atoms. The reason is similar to the discussion of the 30 Hz data in the time-domain, and t_{hold} needs to be much longer (greater than 160 ms for all even n) to reduce the aliasing effect of the spectrum analysis, but t_{hold} in our system is limited by lattice heatings and atom losses. Thus to find the number distribution of a system, the choice of q and u_L is critical to ensure the amplitude is larger than the noise while different f_n are well separated within t_{hold} . Based on Fig. 3.5(b), q should be large

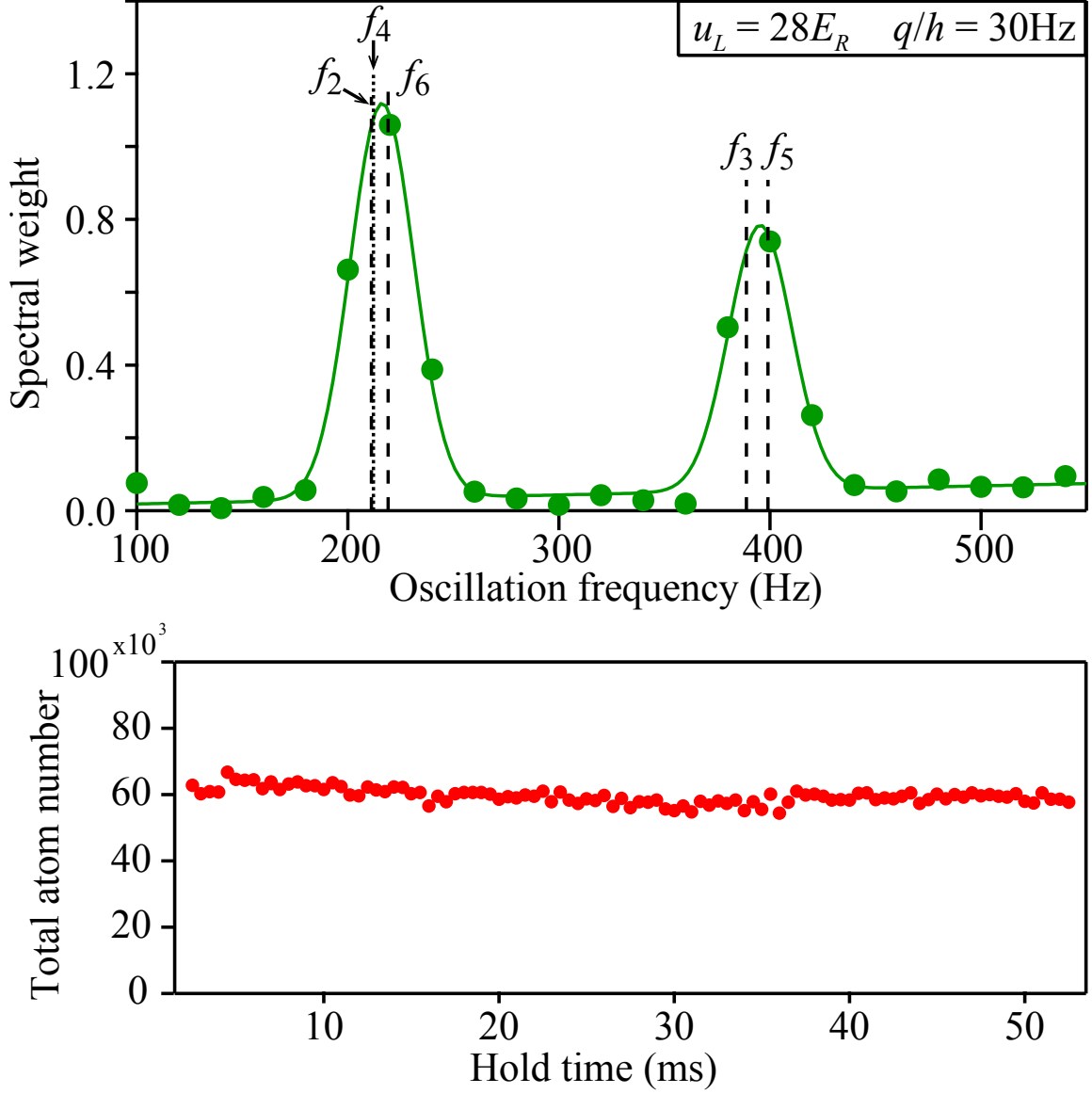


Figure 3.7: (a) Circles represents the FFT on the $q/h = 30\text{ Hz}$ data set shown in Fig. 3.5 (a). Vertical lines mark the predicted f_n . (b) The atom number of the same group of data.

enough to separate f_n while not too large since the oscillation amplitudes decrease as q increases. u_L should be deep enough to yield separable f_n , but too much lattice power could heat up atoms significantly.

3.4 Empirical model for damped spin oscillations

We develop the following empirical formula based on the predicted f_n for an inhomogeneous system with a certain n_{peak} , and find all observed spin dynamics can be fit by this formula [67]

$$\rho_0(t) = \sum_{n=2}^{n_{\text{peak}}} A_n \exp(-t/\tau_n) \sin [2\pi f_n(t - t_0)] + \Delta\rho_0 \exp(-t/\tau_0) + \frac{1}{3}. \quad (3.5)$$

Here the first term sums up individual Rabi-type oscillations at all possible n . We define the damp rate of oscillation amplitudes as $1/\tau_n$. t_0 marks the beginning of oscillations since the magnetic field needs some time to get stabilized after the quench. The second term describes an overall decay of ρ_0 at a decay rate of $1/\tau_0$. This decay may be mainly due to unavoidable lattice-induced heatings. The third term indicates that the three spin components eventually equally distribute in equilibrium states when $t_{\text{hold}} \rightarrow \infty$ [114, 115]. Typical fitting results can be found in Fig. 3.5(a). The observed atom losses are less than 10% within every time evolution studied in this work, as shown in Fig. 3.7(b). This serves as a justification for the validity of Eq. (3.5), a conservative model.

We keep τ_n in Eq. (3.5) at fixed values to improve and simplify the fittings. Figure 3.8 uses the $q/h = 85$ Hz data set in Fig. 3.5(a) to illustrate how we can extract τ_n from a series of FFT spectra. Starting at $t_{\text{hold}}^{\text{start}}$ and ending at $t_{\text{hold}}^{\text{end}} = t_{\text{hold}}^{\text{start}} + 40$ ms, we can divide the $q/h = 85$ Hz data into different time region, so we can conduct Fourier transformations onto the data set over various regions. Similar to those FFT results shown in Fig. 3.6(a), the obtained FFT spectra has five distinguished peaks and their peak positions agree with the predictions. The height of the peak p_n centered at oscillation frequency f_n in a FFT spectrum is extracted. The plot of p_n has dependence on $t_{\text{hold}}^{\text{start}}$ for each fixed n as the two typical examples shows in Fig. 3.8. The damping of the spin-mixing oscillations is reflected by the decays of p_n . The constant τ_n can thus be extracted from an exponential fit to the data at a fixed n , as shown by solid lines in Fig. 3.8. For the $q/h = 85$ Hz data,

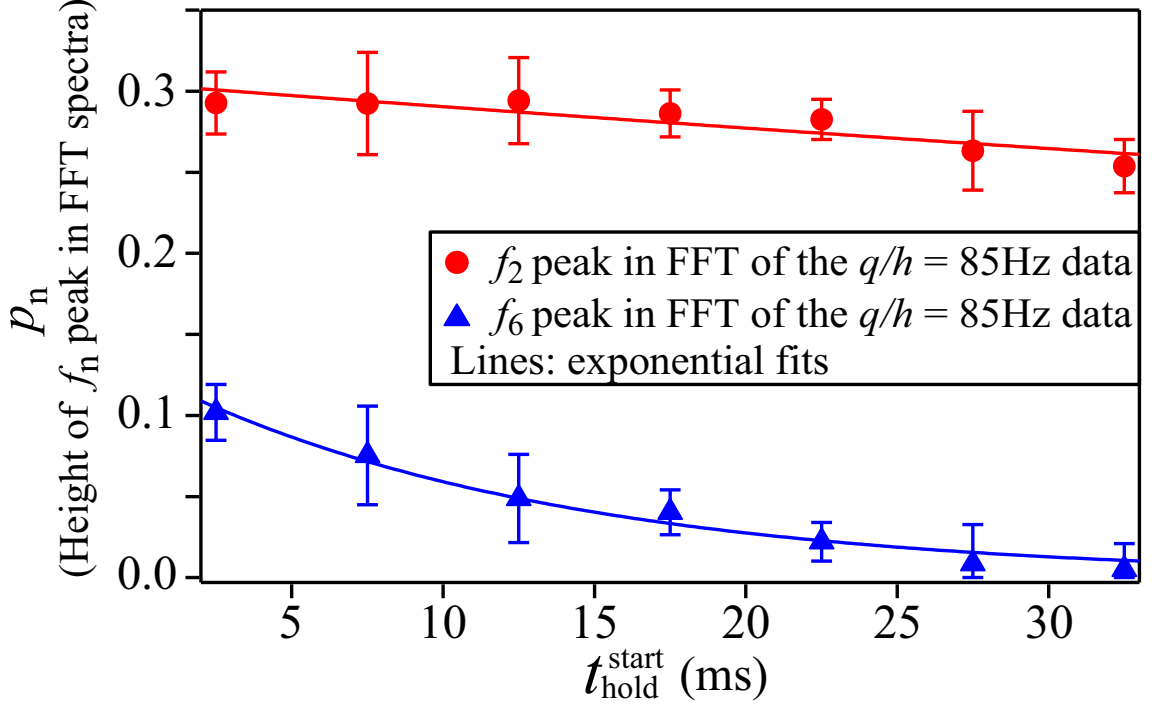


Figure 3.8: Circles (triangles) represent p_2 (p_6) as a function of $t_{\text{hold}}^{\text{start}}$. Here p_n is the height of the peak centered at f_n in a FFT spectrum of the $q/h = 85\text{Hz}$ data set shown in Fig. 1(a), and each FFT starts at $t_{\text{hold}}^{\text{start}}$ (see text). Lines are exponential fits. (This figure is adapted from our published work [67].)

τ_n are fixed at these extracted values, as listed in Table 3.2. The damping of oscillations represented by τ_n may be due to several different mechanisms. For example the atoms losses and heating to higher bands can terminate the dynamics of atoms in the certain site. The relative dephasing of lattice sites also leads to the decay of revivals of the spin states. This is possibly related to the inhomogeneity of the trap, and the finite tunneling coupling J . The τ_n in Table 3.2 shows that $n = 2$ sites have much smaller damp rate comparing with $n \geq 3$ sites, indicating the three-body interactions or higher-body interactions may play a major role in inducing the damping of the oscillations.

Other fitting parameters used in a good fitting curve (i.e., the blue solid line in Fig. 3.5(a) for the $q/h = 85\text{Hz}$ data) are also listed in Table 3.2. The decay constant τ_0 for ρ_0 reduces with hold time as the table shows, which indicates that more induced heatings at longer t_{hold} make the spin oscillation decays more quickly. The best fits for other data sets taken at smaller q , however, all yield constant τ_0 . The underlying physics of this field-dependent

Fixed parameters:

τ_2 (ms)	τ_3 (ms)	τ_4 (ms)	τ_5 (ms)	τ_6 (ms)
214	30	34	12	13

Fitting parameters:

U_2/h (Hz)	A_2	A_3	A_4	A_5	A_6	t_0 (ms)	τ_0 (ms)	$\Delta\rho_0$
79.4	0.017	0.012	0.02	0.012	0.01	0.48	$87-0.34t_{\text{hold}}$	0.472

Table 3.2: Parameters used in the blue solid line in Fig. 3.5(a) (see text). (This table is adapted from our published work [67].)

heating may be interesting for further study. The deduced atom number distributions χ_n can also be extracted by dividing the fitting parameters A_n listed in Table 3.2 with the spin oscillation amplitude D_n in Table 3.1. These values agree with the results deduced by the FFT spectra shown in Fig. 2(b). The last term in Table 3.2, value of $\Delta\rho_0$, confirms a connection of our data to the MF predicted ground state: $\Delta\rho_0 + 1/3 \approx \rho_0^T$. Here ρ_0^T is the predicted ρ_0 in the ground state of the spinor gases at the given q and u_L as discussed in Chapter 1. This experiment can be used to precisely measure important parameters U_2 and U_2/U_0 , which will be elaborated in Chapter 4.

CHAPTER IV

QUANTUM QUENCH ACROSS SUPERFLUID TO MOTT-INSULATOR PHASE TRANSITIONS

This chapter discusses our experimental studies on the spin-mixing dynamics of spinor BECs in cubic optical lattices when the system is quenched across the SF-MI phase transitions. One paper related to these topics was published:

- Z. Chen, T. Tang, J. Austin, Z. Shaw, L. Zhao, and Y. Liu, *Quantum Quench and nonequilibrium Dynamics in Lattice-Confined Spinor Condensates*, Phys. Rev. Lett **123**, 113002 (2019). Included in Appendix A.

Besides those early experimental works that studied non-equilibrium spin dynamics with coherent spin mixing, more attention has been paid to the topics like dynamic phase transitions, universality, equilibrations, which are usually beyond the description of hydrodynamics and the MF physics [8]. When a system is taken out of equilibrium by quenching one or several parameters of the Hamiltonian across a phase transition, the unitary time evolution of the system is difficult to be theoretically simulated. Ref. [42, 116] conducted landmark experiments in this direction, which observed the first SF-MI phase transition and the coherent atomic matter-wave field dynamics by ramping the lattice depth at different speeds. In the spinor systems, Ref. [95] first experimentally studied the dynamics of ^{87}Rb driven across the polar and ferromagnetic phases, observed the formation of spin textures, ferromagnetic domains and domain walls. Ref. [80, 103] studied the quantum Kibble-Zurek mechanism in the spin degree of freedom. Here we consider a sequence that quenches the lattice depth across the superfluid to Mott-insulator phase transitions in spinor gases. I

will show the short time coherent spin-mixing dynamics and the calculation of the spin-dependent interaction strength. I will also discuss the long time equilibrations and the tunnelling effects during the quench.

4.1 Dynamics after quenching across SF-MI transitions

Our experiments are performed in a quantum quench scenario starting with an antiferromagnetic spinor BEC at its SF ground state, based on a theoretical proposal in [46]. We continuously quench the potential of a cubic lattice to a very large value, completely suppressing tunnellings to freeze atom number distributions in individual lattice sites. Reference [46] predicted several observables to analyze such non-equilibrium dynamics of the system. It includes the evolution of different spin populations characterized by ρ_0 and the visibility of the TOF pictures. The single-site Hamiltonian neglecting J can still be applied here, as Eq. 3.4 shows. This is mainly because the spin evolution after quench is also in the deep lattice. Meanwhile the exact numerical simulations of the Bose-Hubbard model are still limited in 1-D and 2-D conditions [117]. Therefore the spin-mixing dynamics in a single site with the Quench-L sequence are expected to have the same frequency and amplitude as the case with the Quench-Q sequence at same u_L and q . The oscillation of the visibility is due to the collapse and revival of the matter wave field [116]. The initial coherent state $|\alpha\rangle$ is decomposed into different Fock states $|n\rangle$ in the optical lattices as $|\alpha\rangle = \exp(-|\alpha|^2/2) \sum_n \frac{\alpha^n}{\sqrt{n!}} |n\rangle$, with $|\alpha|^2 = \hat{n}$ the average atom number [116]. After the quench of the lattice depth, atoms in different sites start time evolution with the term $\exp(-iE_n t/\hbar)$. The eigenenergy $E_n = U_0 n(n-1)/2$ for the scalar case considering only two-body interaction, and the oscillation of the visibility features a single frequency U/h . Such collapse and revival of the matter wave field have been observed in Ref. [116]. Experiment with effective multi-body interactions up to six-body case have also been studied [118], which can be used to precisely measure the multi-body interaction energies. For antiferromagnetic spinor BECs the results are expected to be more complex [46], since there is extra U_2 term that alters the eigenenergies. However, for $q = 0$ case there is a dominant

frequency at $(U_0 + U_2)$, which can be used to determine the important parameter U_2/U_0 of the system regardless of the lattice parameters [46].

4.1.1 Experimental sequences

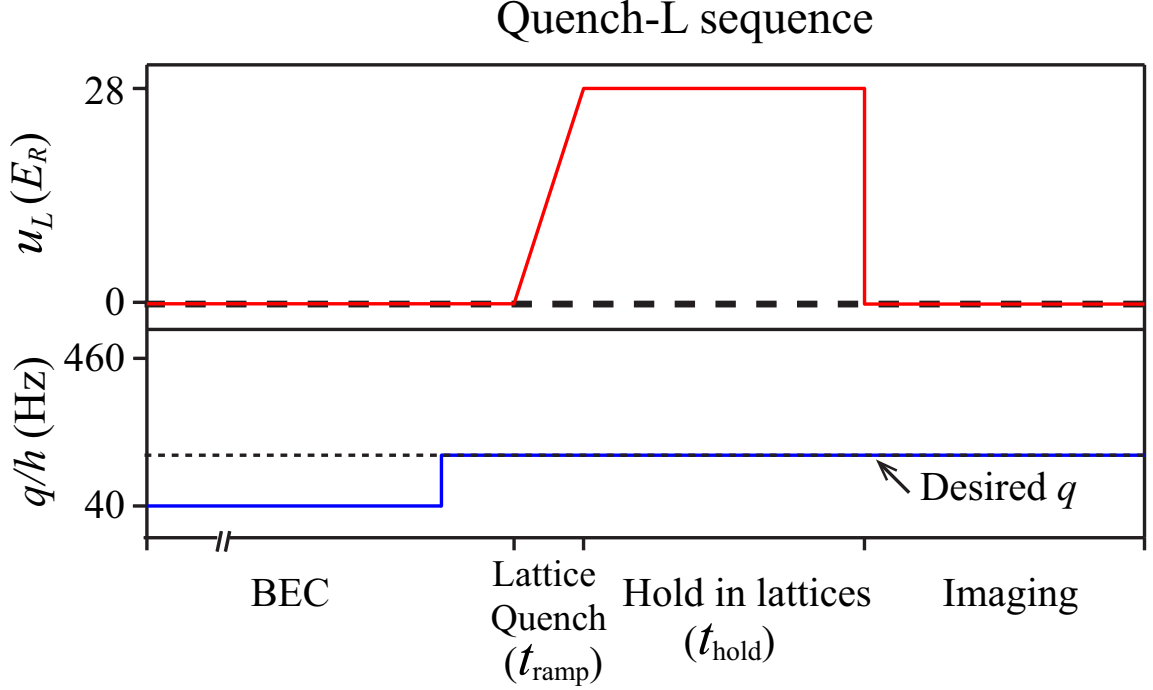


Figure 4.1: Schematic of our Quench-L sequence (see text). All axes are not to scale. (This figure is adapted from our published work [67].)

Figure 4.1 illustrates the experimental sequence (Quench-L sequence) used in this work. Similar to the Quench-Q sequence, the sequence starts in free space at $q/h = 40\text{Hz}$ with up to 10^5 sodium (^{23}Na) atoms in the LP state. After the initial state preparation we tune magnetic fields to a desired q and then quench up the lattice depth u_L from 0 to $28(2)E_R$ within a time duration t_{ramp} . Similarly atoms are localized into individual lattice sites after the lattice loading. In a Quench-L sequence, we have two criteria for choosing the lattice ramp time t_{ramp} . First, t_{ramp} is long enough, $du_L/dt \ll 32\pi E_R^2/h$, to satisfy the interband adiabaticity requirement [36]. Second, t_{ramp} is short enough to make the ramp non-adiabatic for spin-mixing oscillations, but is not too short so we can limit the discussion of oscillations between the ground states and the first excited states. After certain hold times we apply

the two-step microwave imaging method to monitor the time evolution of ρ_0 .

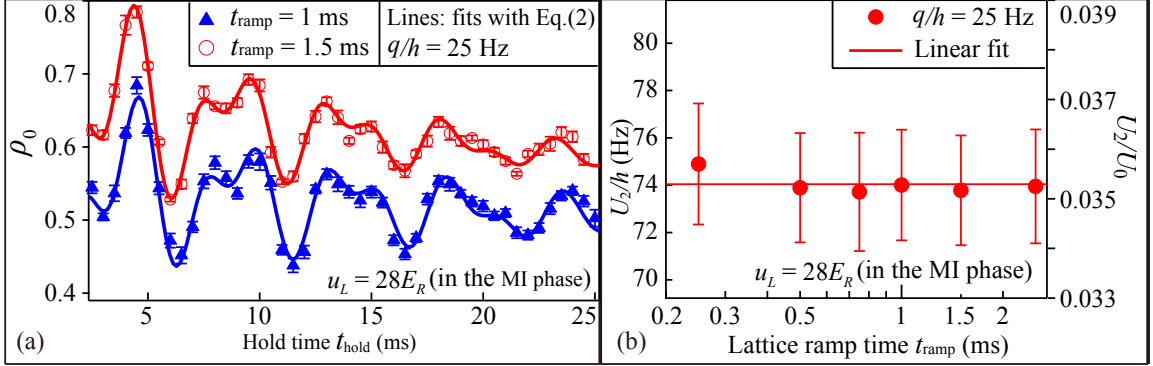


Figure 4.2: (a) Observed spin dynamics after Quench-L sequences at two t_{ramp} . Lines are fits based on Eq. (3.5). Data taken at $t_{\text{ramp}} = 1.5$ ms are shifted up by 0.1 for visual clarity. (b) Extracted U_2 and U_2/U_0 from fitting observed dynamics with Eq. (3.5) at various t_{ramp} . The horizontal line is a linear fit. (This figure is adapted from our published work [67].)

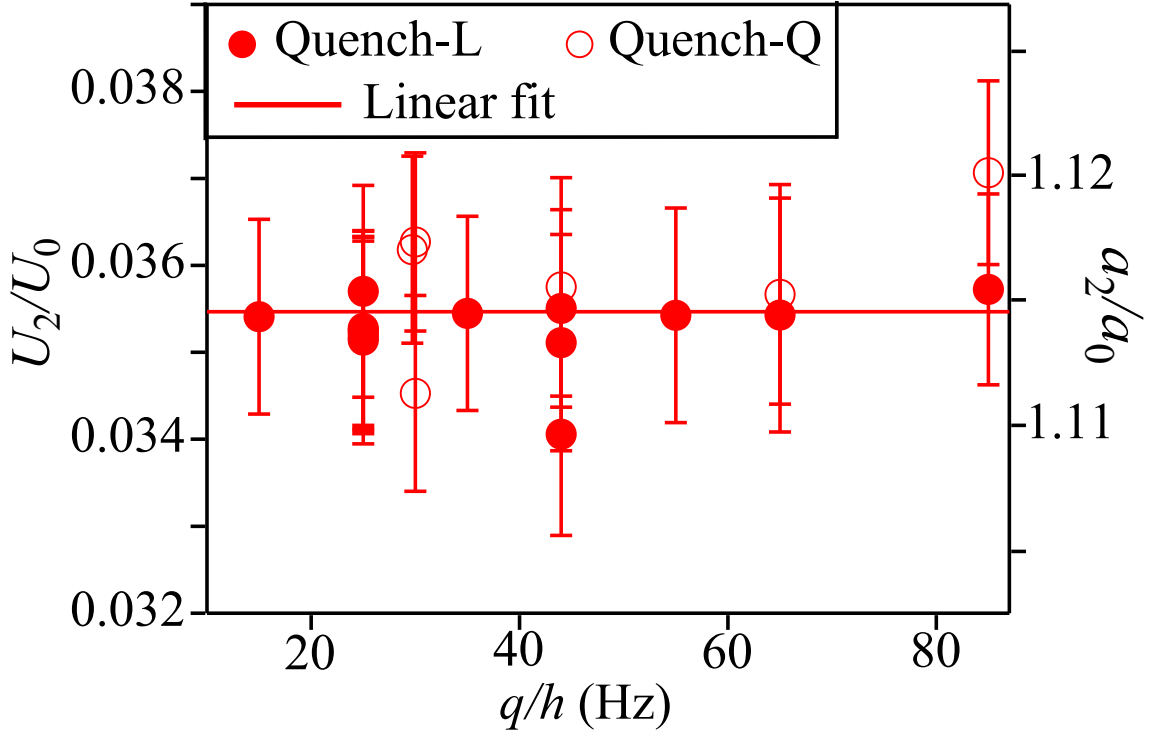


Figure 4.3: U_2/U_0 extracted from the spin dynamics observed under 20 different conditions. The right axis marks the corresponding ratio $a_2/a_0 = (U_2 + U_0)/(U_0 - 2U_2)$, where a_0 and a_2 are scattering lengths. (This figure is adapted from our published work [67].)

4.1.2 Precisely measure spin-dependent interactions

Non-equilibrium spin dynamics are also detected in time evolutions of spinor gases after Quench-L sequences. Figure 4.2 and 4.3 show results after such quench sequence with a wide range of magnetic fields. Although the theoretical model has been studied by Ref. [46], we are the first group to experimentally observe such complicated spin-mixing dynamics. For very short quench time like $t_{\text{ramp}} < 1$ ms, atoms in our system need additional 1 ms to completely lose their phase coherence, which is similar to the phenomenon reported in rubidium systems [119]. We did not observe the revival of the matter wave phase coherence for several possible reasons. First, the typical quench time in our experiment is longer than Ref. [116, 118], and part of the system could dynamically cross the phase transitions [120]. Second, the revival amplitude may quickly damp due to reasons like the inhomogeneities in the lattice and the finite tunneling coupling. Since we typically sampled the time evolution every 0.5 ms, we may not be able to capture the featured frequencies $U_0/h \sim 10^3$ Hz [46]. Third, the effect of q may alter this process which has not been studied yet. For longer quench times the spin dynamics very weakly depend on t_{ramp} . Figure 4.3(a) shows two examples, in which the oscillation frequencies are almost the same and the oscillation amplitudes are slightly different. This is an interesting phenomenon since when the quench time is very long the ramp becomes adiabatic. The transition from non-adiabatic ramps to adiabatic ramps is to be explored.

Eq. (3.5) is also applied to fit the spin oscillations observed after Quench-L sequences since the spin dynamics still happen in deep lattices. We can extract the spin-dependent interaction U_2 from these fitting curves for both quench sequences. This is simply because when $n \geq 2$ at a fixed q , U_2 decides frequency f_n . Figures 4.2(b) and Fig. 4.3 show the extracted U_2 from 20 experimental data sets taken under very different conditions. U_0 is derived by following [57], and the predicted values of U_0 at typical u_L are listed in Table 4.1. A linear fit to the data points in Fig. 4.3 gives the precise values for two key parameters determining the spinor physics, i.e., $U_2/U_0 \simeq 0.035(3)$ and $a_2/a_0 \simeq 1.115(10)$ for ^{23}Na atoms. Here a_2 and a_0 are s-wave scattering lengths, and $a_2/a_0 = (U_2+U_0)/(U_0-2U_2)$ based

on Ref. [13, 30]. The published values of U_2/U_0 were usually derived from the scattering lengths [46, 121–127]. For example, [121, 122] respectively found scattering lengths that would lead to $U_2/U_0 = 0.032(14)$ and $0.035(11)$. Another common method is to measure the scattering lengths through Feshbach spectroscopy, which could yield $U_2/U_0 = 0.037(6)$ [124] and $0.036(3)$ [123]. By comparing with the published U_2/U_0 values, we can conclude that our method can conveniently measure U_2/U_0 with a good resolution.

u_L	U/E_R	J/E_R	$h/4J(\text{ms})$
12	0.131380845	0.012252082	2.661713449
14	0.15095208	0.008004102	4.074352306
19	0.197163798	0.002996508	10.8831785
25	0.248915214	0.001038582	31.40005453
28	0.273656588	0.000635039	51.35358842
33	0.313553907	0.000292616	111.4482169

Table 4.1: Calculated U , J and $h/4J$ for different u_L with 20 plane waves and 10 lattice sites. The wavelength is 1064 nm and the s -wave scattering length for ^{23}Na is $a_s = 2.75$ nm.

4.2 Comparisons among quantum quench sequences

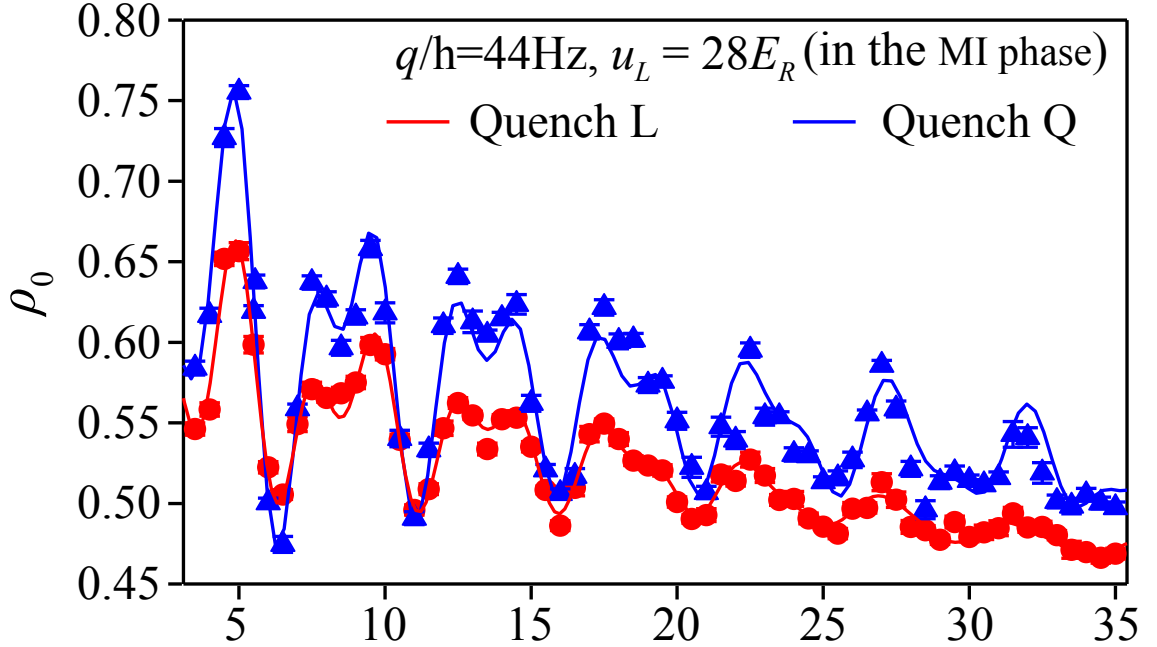


Figure 4.4: The spin dynamics after Quench-Q and Quench-L sequences. The final lattice depth ($28E_R$) and the q (44 Hz) are the same for both sequences.

One difference is noticed between the non-equilibrium spin dynamics initiated by Quench-L and Quench-Q sequences: despite having the same frequencies when spinor gases are prepared into the same final u_L and q , atoms appear to oscillate with a larger amplitude after the Quench-Q sequence. This is shown in Fig. 4.4 for $q = 44$ Hz and $u_L = 28E_R$. We consider this amplitude difference caused by the biggest difference of the two ramp sequences that the Quench-Q sequence starts in the deep lattice while the Quench-L sequence starts in the superfluid phase. Therefore the dephasing and energy dissipations can be induced during the Quench-L sequence by a number of tunnelling processes. Since for Quench-Q sequences atoms are fully localized in individual lattice sites with negligible tunnellings. In contrast, a Quench-L sequence ramps the system across the SF-MI phase transitions, tunnellings among adjacent sites thus cannot be ignored during a certain part of this sequence. Other possible reasons besides the tunnelling induced effect may include significant heatings during first-order SF-MI phase transitions at a small q for Quench-L sequences [68], non-adiabatic lattice ramps in Quench-L sequences, and different atom number distributions introduced by the quench sequences. The last term is interesting for further studying since it could potentially be used to manipulate the density distribution of the system. Since the Quench-L gets the system across the SF-MI phase transitions, we may expect the spin dynamics to show some features related to the transition, although somehow it is not apparent in our current data. This will be discussed in the last two sections of this chapter.

To understand how tunnellings affect the spin-mixing dynamics, we monitor spin oscillations after varying the tunnelling energy J in a well-controlled way [128]. As Fig. 4.5 shows we first prepare a non-equilibrium initial state to $q/h = 30$ Hz following a Quench-Q sequence, and we ramp lattices to a very deep cubic lattice of $u_{L,x} = u_{L,y} = u_{L,z} = 33(3)E_R$ with $J \simeq 0$ for the subsequent quench. The only difference is during the quench of q J is suddenly increased to a desired value by properly reducing only one lattice depth $u_{L,z}$. Here $u_{L,i}$ with $i = x, y, z$ are depths of the three lattice beams along orthogonal directions, respectively.

Fig. 4.6 are results collected at four signature $u_{L,z}$ and their fittings. $u_{L,z}$ gradually spans from the few-body dynamics for spinor gases tightly localized in deep lattices ($u_{L,z} = 33E_R$ with $J \simeq 0$), to the many-body dynamics for atoms loosely confined in shallow lattices

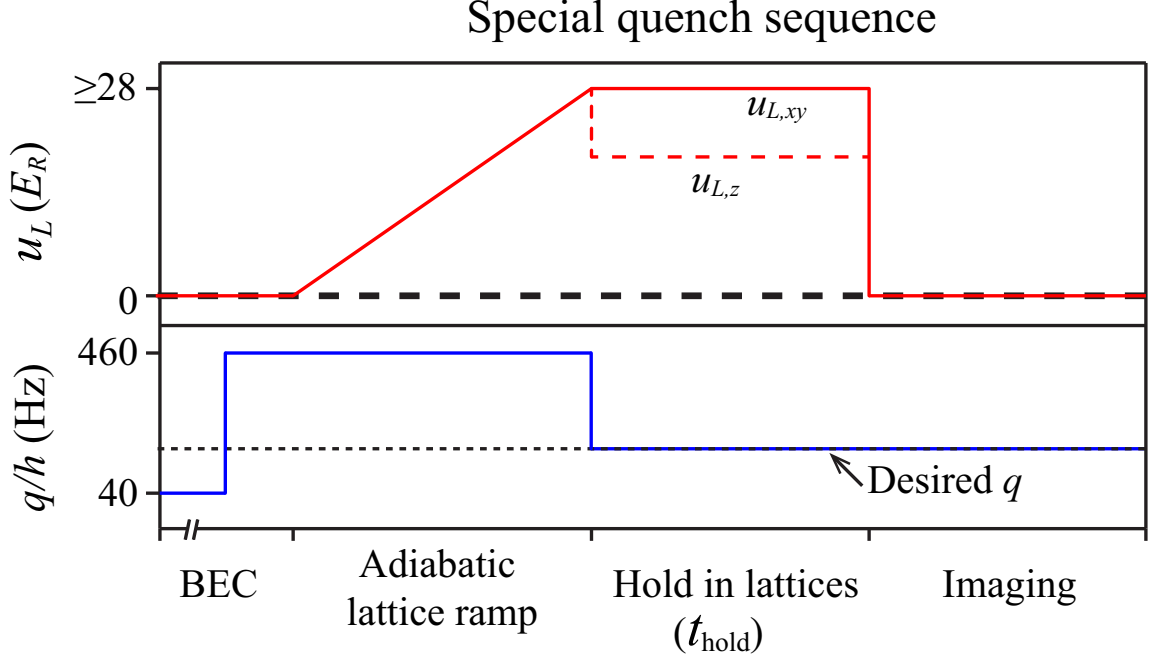


Figure 4.5: A new sequence that quench q and $u_{L,z}$ at the same time. All axes are not to scale.

($J \gg 0$ at $u_{L,z} = 12E_R$) as shown in Table. 4.1. Amplitudes of spin-mixing oscillations appear to quickly decrease during such reduction of $u_{L,z}$, until they completely vanish when $u_{L,z} < 14E_R$. We may consider two scenarios to understand these observations. In the first scenario, consider two atoms oscillating at the frequency f_2 in an $n = 2$ lattice site, so the spin oscillation can stop as one of the two atoms tunnels out of the site. In another scenario, $n > 2$ atoms oscillate in a lattice site at frequency f_n while one atom hops out of this site. Then spin oscillations occurring in this site and the adjacent site that accepts the atom should be changed. The occurrence of many of such tunnelling events could cause phase difference and destroy the collective observed spin-mixing dynamics. As J increases with the reduction of $u_{L,z}$, the damping is enhanced and eventually stops the spin oscillations. A numerical example shows the predicted damp time constant due to tunnellings is 11 ms at $u_{L,z} = 19E_R$ in Table 4.1 [128], which is comparable to the experimentally extracted τ_n of around 15 ms extracted from Fig. 4.6(a). Therefore our use of deep lattices and subsequent neglecting of J in Eq. (3.4) are experimentally justified. However, the demonstration of the underlying physics of the damped spin dynamics remains to be solved. Its connection with

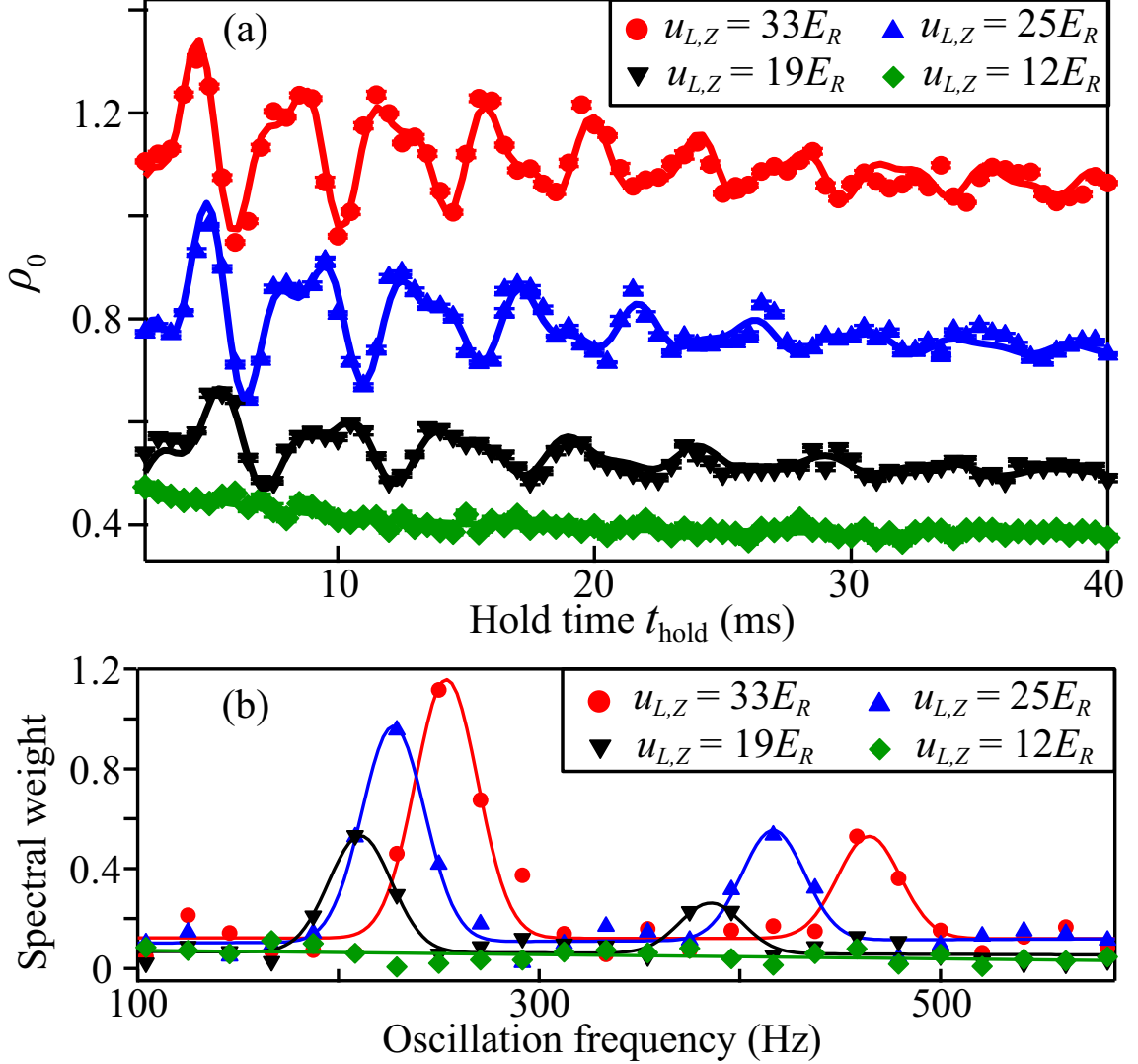


Figure 4.6: (a) Observed spin dynamics after Quench-Q sequences to $q/h = 30$ Hz at various $u_{L,z}$ while $u_{L,x} = u_{L,y} = 33(3)E_R$ (see text). Results obtained at $u_{L,z} = 33(3)E_R$, $25(2)E_R$, and $19(2)E_R$ are respectively shifted up by 0.55, 0.25, and 0.06 for visual clarity. Lines are fits based on Eq. (3.5). (b) FFT spectra of the dynamics shown in Panel (a). Lines are two-Gaussian fits. (This figure is adapted from our published work [67].)

the Schwinger boson model [129, 130] are suggested to be worthy of further investigation.

Figure 4.6(b) shows the FFT spectra extracted from panel (a) at all four $u_{L,z}$. These FFT spectra all have only two distinguished peaks rather than the predicted five peaks, i.e., the wide peaks at around 250 Hz correspond to the oscillations of even n atoms and the wide peaks at around 450 Hz to the oscillations of odd n atoms. One possible reason for this discrepancy has been mentioned during the discussion of the Quench-Q 30 Hz data, that

t_{hold} needs to be much longer to reduce the aliasing effect of the spectrum analysis, but t_{hold} is limited in our system. In addition, The FFT spectra in Fig. 4.6(b) show that a larger $u_{L,z}$ leads to spin oscillations of higher frequencies, which can be interpreted by the effective lattice depth $u_L = \sqrt[3]{u_{L,x}u_{L,y}u_{L,z}}$. Our calculations of f_n based on effective U_2 verify this, as the calculated oscillation frequencies fall into those broad peaks.

Another difference between the observed spin dynamics initiated by Quench-L and Quench-Q sequences is the extracted number distribution based on FFT spectra, especially for the high q data where peaks for each n can be resolved in the spectra (the spectrum for Quench-L data is not shown). It has been demonstrated that for Quench-Q sequence where the lattice ramp is adiabatic, the Mott-insulator state is number-squeezed and follows the shell distribution. For Quench-L sequence, the number distribution is expected to be frozen at the initial condition when the ramp is fast enough [118], which follows the Poisson distribution [131]. This has been verified in different systems [65, 119]. When the lattice ramp changes from sudden quench to continuous quench, we should expect the gradual change of the number distribution. The quantitative analysis of this problem will be published in our future work.

4.3 Universality and the Kibble-Zurek scaling law

Universality is crucial in studying the continuous phase transition as it allows us to neglect many microscopic details of the system and do calculations. It usually manifests in the scaling behavior of parameters related to the phase transition, for example the order parameter. An universal power-law scaling was predicted in the Kibble-Zurek mechanism (KZM) to understand such non-equilibrium situation when system is quenched across a phase transition point. The excitations respond to the quench rate as a power function, and the exponent is related to the equilibrium critical exponent [71]. For example if there is a critical temperature T_c , and T is tuned as $T = T_c - vt$. The relaxation time diverges as $\tau_{\text{rel}} \sim 1/|T - T_c|^{zv}$ where z is the critical exponent. The time $t = \tau_{\text{rel}}$ determines when adiabaticity is violated. Then the critical length scale is $\xi_c \sim 1/|v|^{v/(zv+1)}$ and density of

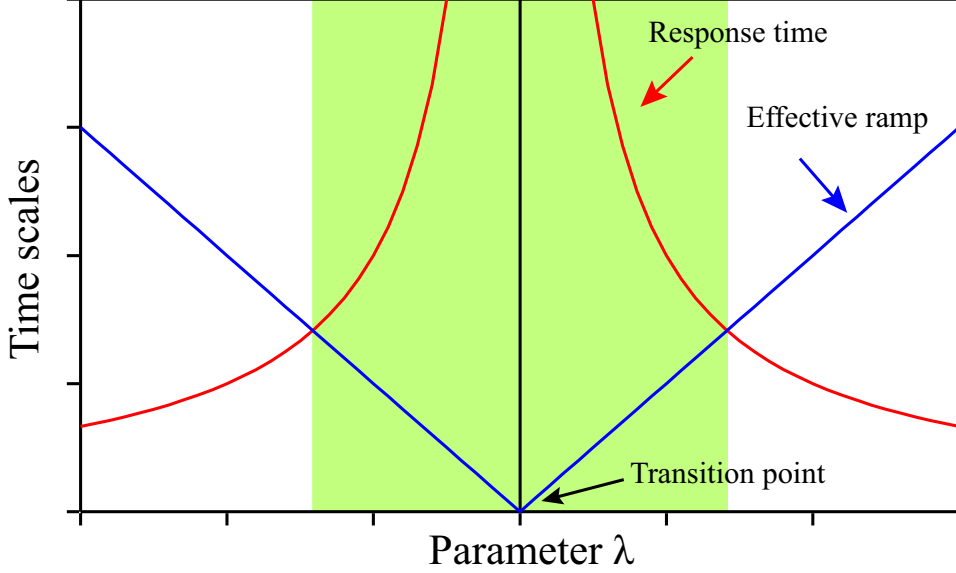


Figure 4.7: Schematic diagram of the freeze out region. The reaction time diverges as the red line shows. The ramp of λ is represented by the blue line, and the two intersections of the lines determine the freeze-out region (green shaded) [71, 80]

defects for d -dimensional system is $n_{\text{ex}} \sim 1/|v|^{dv/(zv+1)}$. The idea was first introduced by Ref. [132, 133], then it was extended by Ref. [134–136]. And the following experimental studies have been conducted in many different systems to confirm this theory [137–139].

Recently interest has been increasing in extending the KZM to the quench across a quantum phase transition. Then it is the quantum fluctuation that drives the system across the phase transition, and the tuning parameter should be one or more terms in the Hamiltonian. Considering the tuning parameter λ , and the quantum critical point (QCP) at λ_c . For a continuous quantum phase transition, the energy gap Δ diminishes toward 0 as the system getting close to the QCP by $\Delta(\lambda) \sim |\lambda - \lambda_c|^{z\nu} \sim |vt|^{z\nu}$. The reaction time of the system to the change Δ is proportional to $1/\Delta$, and the energy scale at $1/\Delta = \frac{\Delta}{\dot{\Delta}}$ is where the adiabaticity breaks down, here $\dot{\Delta} = d\Delta/dt$ [71]. Then the density of defects can be derived. The system can stay in the original state after passing the QCP when the reaction time is still large until the adiabaticity resumes. So there is a freeze out region as Fig. 4.7 shows. The experimental observations of power law scaling were first conducted in the lattice-trap scalar BECs. Ref. [140] measured the excitations in the BECs and Ref. [120] measure the growth of coherence. In spinor BECs, Ref. [80] verified the quantum KZM by measuring

the evolution spin populations during the quench from the polar phase to the broken-axis-symmetry phase of ^{87}Rb . For ^{23}Na there exists a first order transition between the polar phase and the antiferromagnetic phase, Ref. [103] was able to find a scaling law following the generalized quantum KZM.

For our Quench-L sequence, the ratio J/U_0 (as does J/U_2 as $U_2 = 0.035U_0$) is quenched across the SF-MI phase transition. The amount of excitation is generally expected to have a scaling effect. The related observable is the oscillation amplitude in our system. The observed amplitude decreases when the quench time is long and the ramp is close to adiabatic, but for the short quench time cases, we does not observe a power law dependence, neither does any other extracted information during the spinor evolution after the quench. It maybe related with the first-order nature of the transition for even Mott lobes. Or we should check the spin dynamics during the quench rather than after the quench. The experimental studies of this problem will be published in our future work.

We also designed a different method to study the scaling law in our system. As predicted in [68], the SF-MI transition could also happen when u_L is fixed and q changes, since the phase transition happens earlier for small q . So a possible sequence is like what Fig. 4.8(a) shows. u_L ramp to an intermediate values u_L^{inter} at small q so for example only $n = 2$ atoms across the phase transition to form Mott-insulator state, then if q gradually increase and the transition point at q_{final} becomes larger than u_L^{inter} , then $n = 2$ atoms are expected to get back to the superfluid state. Since q is a parameter can be easily manipulated by either applying a magnetic field or a microwave dressing field, we can precisely control its quench speed and study whether scaling law appears during such transition. We designed such a different quench q sequence with $u_L^{\text{inter}} = 18.5E_R$, q/h starts from 10 Hz and is quenched to 150 Hz. The depletion fraction D is extracted and D is around 0 (1) for atoms in the superfluid (Mott-insulator) state. Therefore D should decrease when atoms cross the MI-SF transition by increasing q . The observed depletion fraction however, does not follow the expected trend. For long ramp time corresponding to the adiabatic case, the state should have D as the blue marker shows on the graph, which is the depletion fraction after a direct ramp to $u_L^{\text{inter}} = 18.5E_R$ at $q/h = 150$ Hz. However the data show a increased D after the

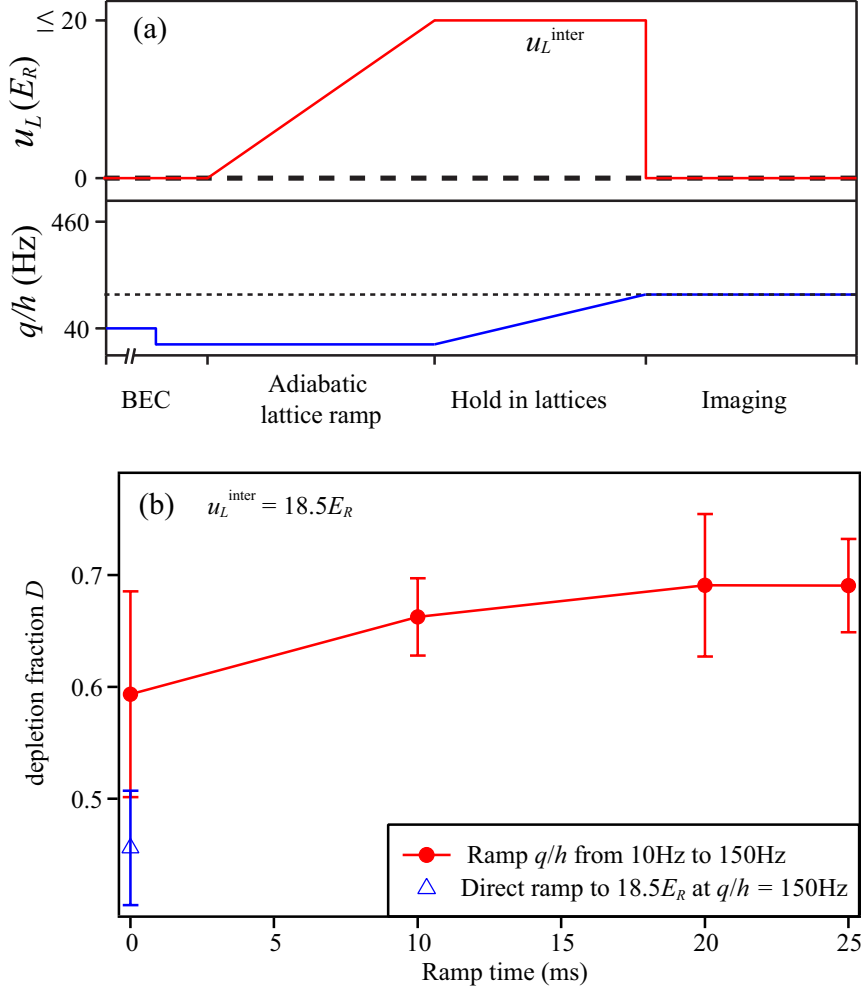


Figure 4.8: (a) Schematic of the special quench q sequence at an intermediate lattice depth. All axes are not to scale. (b) The extracted depleted fraction at different ramp time.

ramp, meaning the final state is not getting back to the expected ground state, or the phase transition does not happen. One possible reason is that there are too much heating induced during the ramp q time. One of the solution is to further cool down our system. Several methods have been demonstrated to cool down atoms in optical lattices [62, 141, 142]. This is not only important for study of the dynamic process of the system, but is also significant for researches of the ground state properties, quantum magnetism, and applications like quantum information processing [62, 143].

4.4 Equilibration and thermalization of isolated quantum many-body system

The equilibration of our system after the quench sequences shows ρ_0 reached $\sim 1/3$ when t_{hold} is long enough. This is possibly related to the appearance of the normal state, the degeneracy of different spin components and the heating in the system [61, 114, 115]. In the previous experiments at free space, Reference. [19] observed the damping of the spin population oscillations after a few cycles. It could be explained as the inhomogeneous broadening of the spin-mixing frequency [144], which is also supported by the emergence of the spatial mode along the long axis observed in their experiment. In Ref. [112], the time evolution of ρ_0 and the Faraday signal both indicated a separatrix crossing in phase space driven by the energy dissipation. And the system gradually evolved to the ground state [20]. The dissipation associated with the coupling between condensate and noncondensate atoms suggested by Ref. [145] remains to be experimentally tested.

Another intriguing question is how the unitary time evolution of a nonequilibrium initial state of a non-integrable many-body quantum system evolve to a ‘thermal state’ so statistic physics could apply, or does it happen at all [7, 11, 71, 146]. More specifically, when the state evolve under $|\Psi(t)\rangle = e^{-i\hat{H}t}|\Psi(0)\rangle$, will there be a thermalized local observable. Ref. [147] first experimentally studied the dynamics of Bose gas in 1-D tubes and demonstrated that the momentum distributions persist without noticeably equilibration. And they pointed out its possible connection with the integrability of such 1-D system, a important concept in the thermalization of classical systems. Ref. [148] was able to numerically solve the dynamics in such a system with the integrability represented by the full set of conserved quantities. And they explained the properties of the special equilibrium state, which carries more memory of the initial conditions but is still in equilibration.

The many-body localized (MBL) system is such a disordered system with interacting particles localized, and it does not thermalize since thermalization requires the transfer of energies and particles. New integrability, which is represented by an extensive set of quasi-local

integrals of motion, shows up in MBL systems to explain their dynamical properties. This is not only of fundamental interesting for quantum statistics for its unique property, but is also potentially significant for quantum information processing as the quantum information of the initial state can be preserved [11].

As it has been discussed, a spinor cold atom system in optical lattices is weak-coupled to the environment, highly controllable and have long decoherence time. Such system is ideal for studies of non-equilibrium dynamics and its thermalization, or the existence of the many-body localization. Ref. [149] first demonstrated the non-thermalization in the one-dimensional Fermi chains of interacting spin mixtures of two spin components, where the number imbalance, determined by number of atoms occupying even and odd sites, can be monitored. It is observed that above a critical disorder strength, a substantial portion of the initial ordering persists, indicating the non-ergodic evolution of the system and the phase of MBL. For $F = 1$ spinor Bosons in a disordered 2-D optical lattice, Ref. [101] explored the localized phases appeared above a critical disorder strength by monitoring the atom number imbalance between atoms on the left and right side of the domain wall. While there are still some arguments whether MBL exists in the higher dimension than 1-D [11], this is an interesting topic to be further explored experimentally.

$F = 1$ spinor BECs are expected to exhibit a variety of quench-dynamical behaviors including thermalization following the eigenstate thermalization hypothesis, nonthermal equilibration and no equilibration, depending on the initial states and the quench conditions [94]. These predictions are suitable to be verified in our system.

CHAPTER V

SPINOR BECS IN OPTICAL SUPERLATTICES

More complicated optical lattices can also be constructed with various lattice geometry, e.g. the hexagonal lattices [106, 150] and the disordered optical lattices [101, 151]. Specially, we can construct an optical superlattice by simply overlapping a short $\lambda/2$ -wavelength lattice beam with a long λ -wavelength lattice beam. A double well structure is formed in such a superlattice, which is interesting not only because the ground state phase diagram is different from the regular cubic lattice [59, 152–154], but also because it provides an extra freedom to manipulate atoms to move between the two wells for quantum state engineering [155, 156]. Therefore atoms in the superlattices can be used to study the tunneling dynamics including both normal tunneling and second-order tunneling processes [157], or to realize entanglement between atoms in the double well [158]. Over the last decade, bichromatic lattices have been applied to study many intriguing phenomena, such as the preparation of magnetic quantum phases [155], probing long-range magnetic correlations [152, 159], controlling the superexchange interactions and detecting spin correlations of ultracold atoms [160, 161], and realizing spin-orbit coupling with ultracold atoms [162]. My particular interests lie in the ground state properties and many-particle non-equilibrium dynamics for spinor BECs in optical superlattices [152, 154]. In this chapter, I will first introduce the construction and control of our optical superlattice using 532 nm and 1064 nm laser beams. Then I will discuss the ground state phase diagram for such a system. An increasing fraction of spin singlets are expected for the MI state at small q , which is an interesting entangled state as introduced in the first chapter. In the end I will summarize some other methods generating spin entanglement and the detection.

5.1 Experimental setup of a bichromatic superlattice

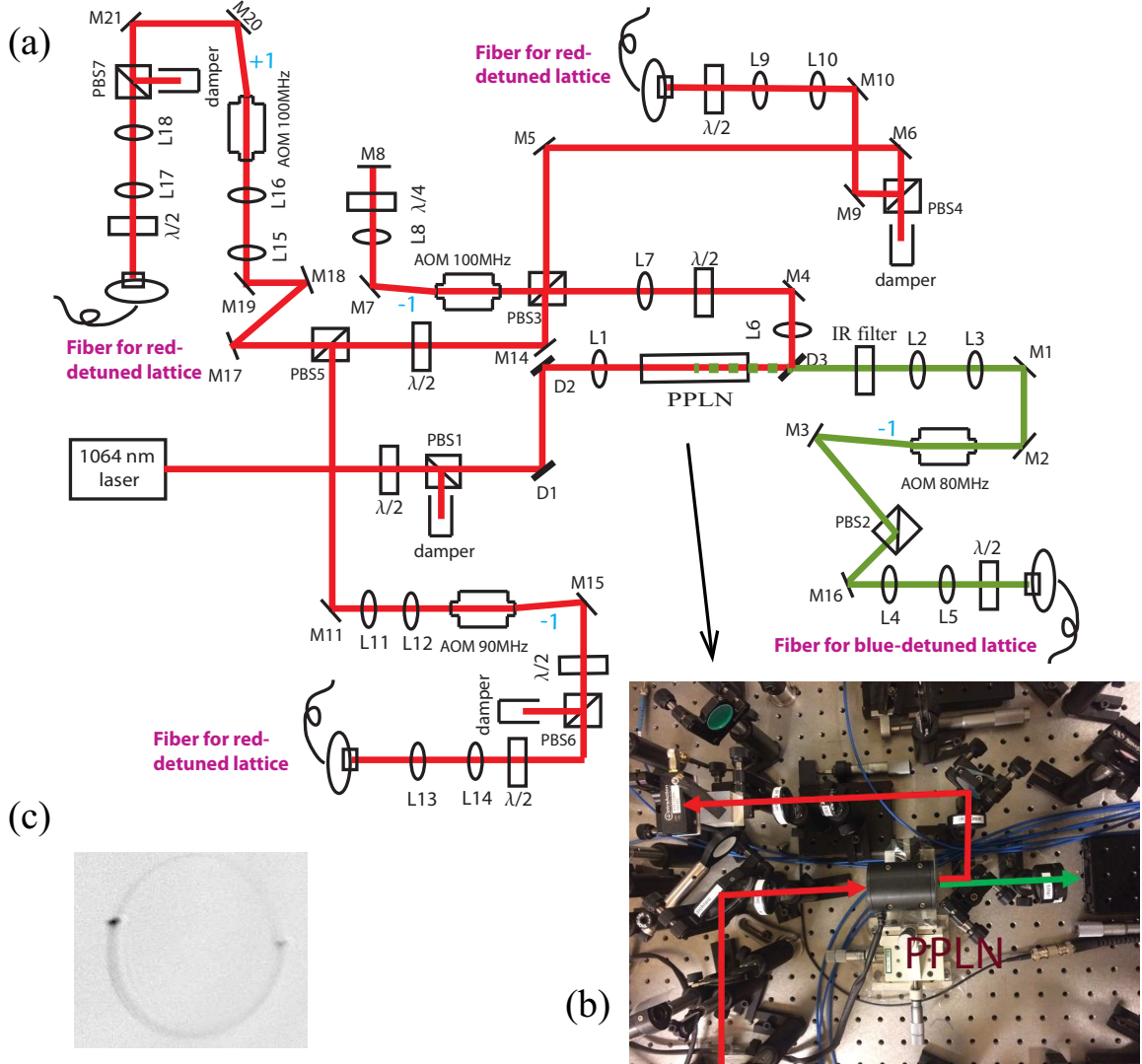


Figure 5.1: (a) Optical layout of all four lattice beams from one laser. The PPLN crystal for second harmonic generation of the green light is highlighted in (b). (c) The blue-detuned green beam is aligned to the center of the BEC and it pushes atoms away to form a ring during time-of-flight.

Based on our cubic lattice setup with the 1064 nm laser beam, we constructed the superlattice structure by overlapping a 532 nm laser beam with one of the horizontal long lattice beams. A single-mode high-power laser is a good option to generate the 532 nm green light. However a phase locking between the green and IR lights is required to stabilize the superlattice potential. A more convenient method is to frequency double the 1064 nm light beam

with a nonlinear crystal through a second harmonic generation using one high-power IR lattice laser. What we used in Fig. 5.1(a) and (b) is a magnesium-doped PPLN nonlinear crystal from Covision Ltd. This PPLN crystal assembly includes five passes with different grating periods and thus five phase matching curves, which enable us to optimize the optical pass. The specified conversion efficiency is up to 2%/W/cm for a low gain CW laser, which indicates a 8%/W conversion efficiency for our 4 cm crystal. The actual conversion efficiency is a bit lower but is still acceptable. With an output power of up to 350 mW at 532 nm, we are able to construct a bichromatic superlattice with a lattice depth up to $25E_R^{\text{Blue}}$. Here E_R^{Blue} is the recoil energy of the blue-detuned lattice created by a pair of counter-propagating laser beam at 532 nm, which is four time of the unit E_R for the 1064 nm lattices. When this blue-detuned lattice beam is aligned to the center of the BEC, atoms are pushed way to all directions as shown in Fig. 5.1 (c).

Our one-dimensional superlattice layout is shown in Fig. 5.2(a). We align the IR and green laser beams along the same optical path horizontally, and retro-reflect them with one same mirror. To minimize the optical distortions, all lenses and mirrors are coated with an anti-reflection film for Nd:YAG laser lines at 532 nm and 1064 nm. By changing the frequency of the acousto-optic modulators (AOMs) before fibers we are able to shift the light frequency and thus control the phase of superlattices. As a node of the standing wave can always be found at the retro-reflection mirror, we can precisely calculate how much frequency shift is needed to realize a desired phase control.

With the relative phase between the two lattice beams being ϕ_l , the 1D superlattice potential can be written as [163],

$$V(x) = -\frac{V_l}{2} \cos(2k_l x + 2\pi\phi_l) - \frac{V_s}{2} \cos(2k_s x). \quad (5.1)$$

Based on Eq. 5.1, the bichromatic superlattice potentials at various relative phases between the two lattice beams can be easily constructed, as shown in Fig. 5.2(b). Shifting the superlattice phase by a half of the period changes the unit cell of the superlattice structure from a symmetric double well to a totally asymmetric one. We realize this in the experiment

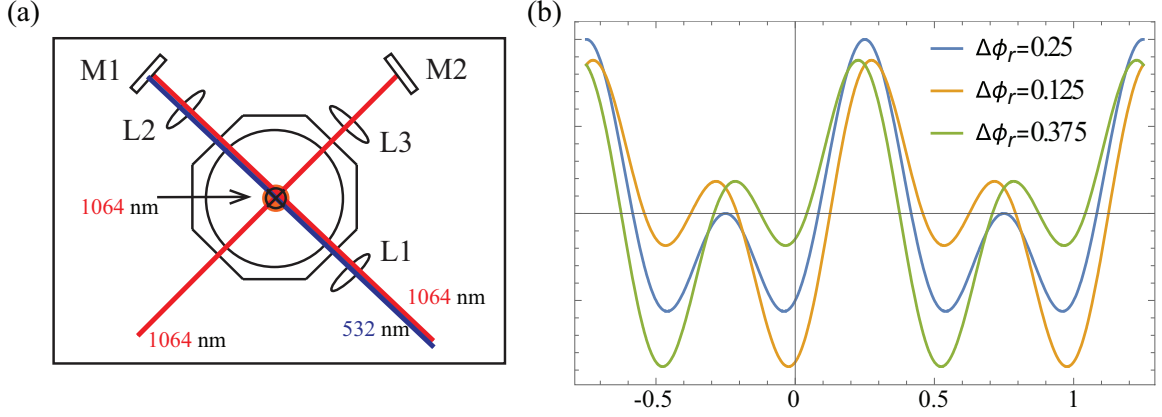


Figure 5.2: (a) Our superlattice setup around the main chamber consisting of a 1064 nm red-detuned and a 532 nm blue-detuned lattice beams along a horizontal direction. Two monochromatic lattices at 1064nm are along two orthogonal directions, another horizontal direction and a vertical direction. (b) The superlattice structure controlled by shifting the relative phase between the blue-detuned and the red-detuned lattices with a fixed power ratio at $V_r/V_g = 1$.

by controlling the frequency shift of the long lattice beam via the AOM on the optical path. This half period shift corresponds to changing the relative phase by $\Delta\phi_r = \phi_l = 0.25$ or $\Delta N_r = 0.25$, where $N_r = 2L/\lambda$ is the number of nodes between the retro-reflection mirror and the BEC in the chamber in the IR lattice beam path. In our setup, $L \simeq 500$ mm and thus $N_r \simeq 9.4 \times 10^5$. Also the corresponding frequency shift is $\frac{\Delta f_r}{f_r} = \frac{\Delta N_r}{N_r}$ with $f_r = 2.8 \times 10^{14}$ Hz. Then $\Delta f_r = 74.5$ MHz. And the frequency shift of the AOM is 37.2 MHz for our double-pass AOM setup.

We also apply the K-D diffraction pattern to calibrate the relative phase of the blue-detuned and red-detuned optical lattices along the same direction. Due to the effect of blue-detuned lattices, we need to consider the Bloch states with the momentum $|p|$ being up to $4\hbar k_L$ as Figure 5.3 (c) shows. Figure 5.3(a) and (b) shows a good agreement between our experimental data and theoretical calculations of $(N_1 - N_{-1})/N_{\text{total}}$ and N_1/N_2 determined by the energy shift ε/h . Here ε/h is the energy offset between left and right sites, determined by $\Delta\phi_r$, and experimentally tuned with the frequency of the IR lattice beams through a double-pass AOM. $N_{\pm 1}$ is the number of atoms with momentum $p = \pm 2\hbar k_L$ and N_2 is the number of atoms with momentum $|p| = 4\hbar k_L$. This method has been applied to conveniently and precisely calibrate a superlattice lattice potential.

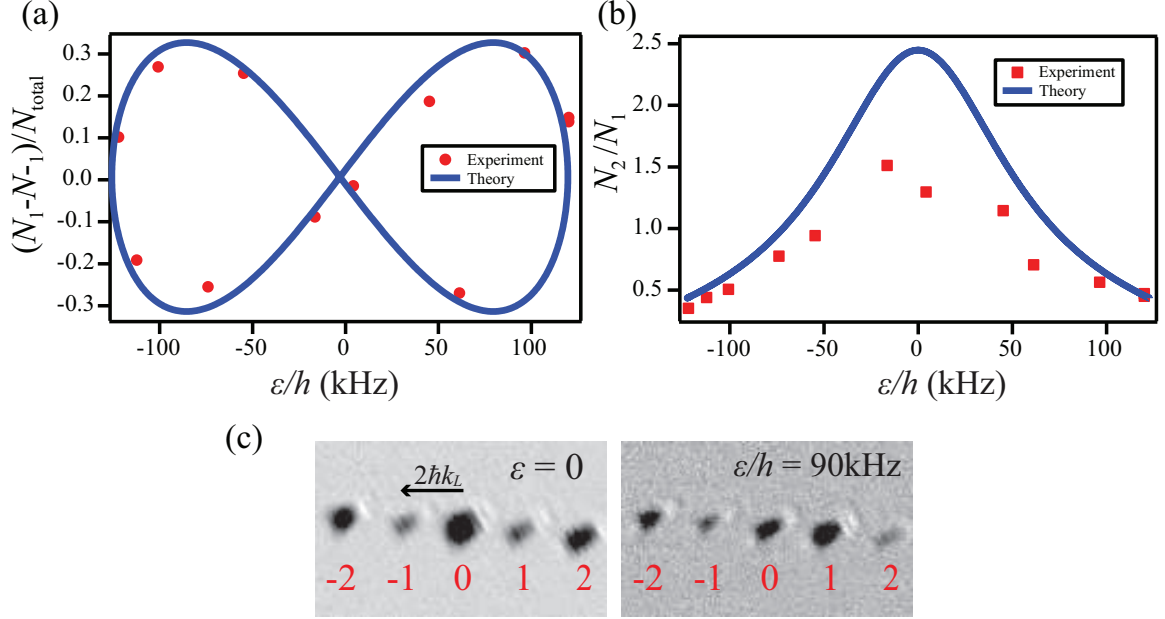


Figure 5.3: Experimental data and theoretical predictions show that (a) $(N_1 - N_{-1})/N_{\text{total}}$ and (b) N_1/N_2 are strong functions of the energy offset ε/h in a bichromatic superlattice. ε/h is determined by $\Delta\phi_r$, and $N_{\pm 1}$ are the number of atoms with momentum $\pm 2\hbar k_L$, N_1 is the number of atoms with momentum $|p| = 2\hbar k_L$, and N_2 is the number of atoms with momentum $|p| = 4\hbar k_L$. (c) Typical diffraction patterns at the symmetric point and a non-symmetric point of a bichromatic superlattice.

5.2 Bose-Hubbard model for a bichromatic superlattice

Figure 5.4(a) shows the schematic diagram of the reciprocal lattice for atoms in the optical superlattice and the imaging process. Figure 5.4(b) marks some of the important parameters in the system. To study bosons in superlattices, several theoretical models have been introduced [59, 154, 156]. Similar to [154], we can still employ the decoupled MF approximation to the BH model for describing spinor bosons in optical superlattices. The site-independent Hamiltonian of superlattice-confined spinor BECs is expressed as

$$\begin{aligned}
\hat{H} = & \frac{U_0}{2} \sum_{i=L,R} \hat{n}_i(\hat{n}_i - 1) - J_i(\hat{\mathbf{L}}^\dagger \cdot \hat{\mathbf{R}} + \text{H.c.}) + \varepsilon(\hat{n}_L - \hat{n}_R) - \mu(\hat{n}_L + \hat{n}_R) \\
& + \frac{U_2}{2} \sum_{i=L,R} (\hat{\mathbf{S}}_i^2 - 2\hat{n}_i) - J_{e1}[\vec{\phi}_R \cdot \hat{\mathbf{L}}^\dagger + \vec{\phi}_L \cdot \hat{\mathbf{R}}^\dagger - \vec{\phi}_R \cdot \vec{\phi}_L^* + \text{H.c.}] \\
& + 2J_{e2}[2\vec{\phi}_L \cdot \hat{\mathbf{L}}^\dagger + 2\vec{\phi}_R \cdot \hat{\mathbf{R}}^\dagger - \vec{\phi}_L \cdot \vec{\phi}_L^* - \vec{\phi}_R \cdot \vec{\phi}_R^* + \text{H.c.}] + q_B \sum_{i=L,R} \sum_j m_{ij}^2 \hat{n}_{ij} \quad (5.2)
\end{aligned}$$

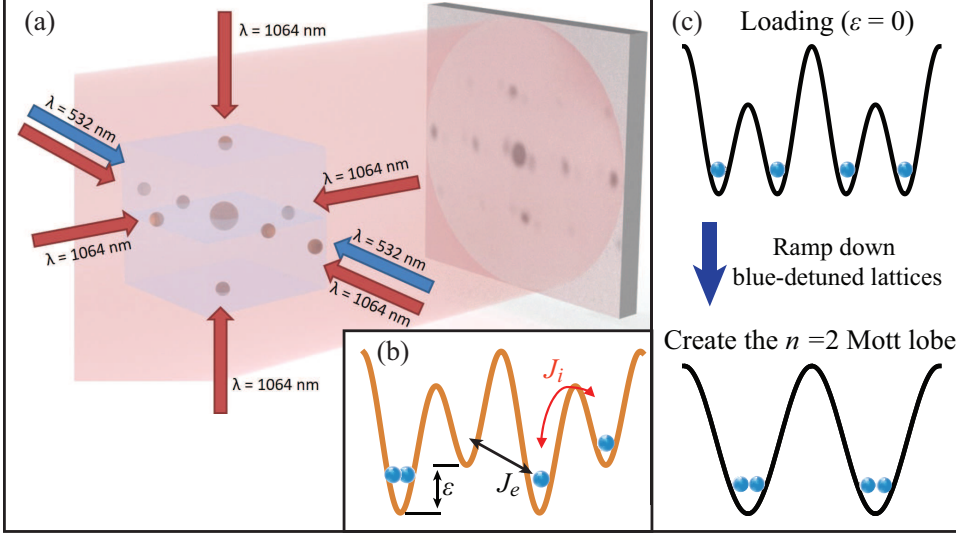


Figure 5.4: (a) Schematic of the reciprocal lattice for atoms in the optical superlattice. The imaging beam is represented by the red area, and a time-of flight picture is captured along the imaging direction. (b) The offset of the double well is ε and the intra-site (inter-site) hopping strength is J_i (J_e). (c) The generation of $n = 2$ Mott lobe.

Considering the double well structure in each unit cell, vector $\hat{\mathbf{L}}^\dagger = \{\hat{L}_1^\dagger, \hat{L}_0^\dagger, \hat{L}_{-1}^\dagger\}$ with L_j^\dagger the creation operator for atoms in $|F = 1, m_F = j\rangle$ ($j = 1, 0, -1$) state in the left well and $\hat{\mathbf{L}}$ contains annihilation operators of the left well. $\hat{\mathbf{R}}^\dagger$ ($\hat{\mathbf{R}}$) is the creation (annihilation) operator of the right well. $\hat{n}_L = \sum_j \hat{L}_j^\dagger \hat{L}_j$ ($\hat{n}_R = \sum_j \hat{R}_j^\dagger \hat{R}_j$) is the atom number at the left (right) site. J_i (J_{e1} and J_{e2}) is the hopping energy within the unit cell (between neighboring unit cells). ε is the energy offset between left and right sites as Fig. 5.4(b) shows. μ is the chemical potential. $\vec{\phi}_{R,L}$ are the vector order parameters. We can conveniently prepare desired states by dynamically changing J and ε (i.e., changing the power ratio and the relative phase $\Delta\phi$ between the two overlapping long and short lattice beams.)

Similarly, the SF and MI states are the two ground states for BECs in very shallow or deep enough superlattices respectively, and for antiferromagnetic spinor BECs, there are metastable states across the phase transition. The value of ρ_0 can still act as an indicator of the ground states and phase transitions. The calculated ground state phase diagram is shown in Fig. 5.5.

Similar to the MF calculations of spinor bosons in cubic optical lattices, our calculations of the superlattice case show U_2 and q_B are two important parameters. In deep enough lattices,

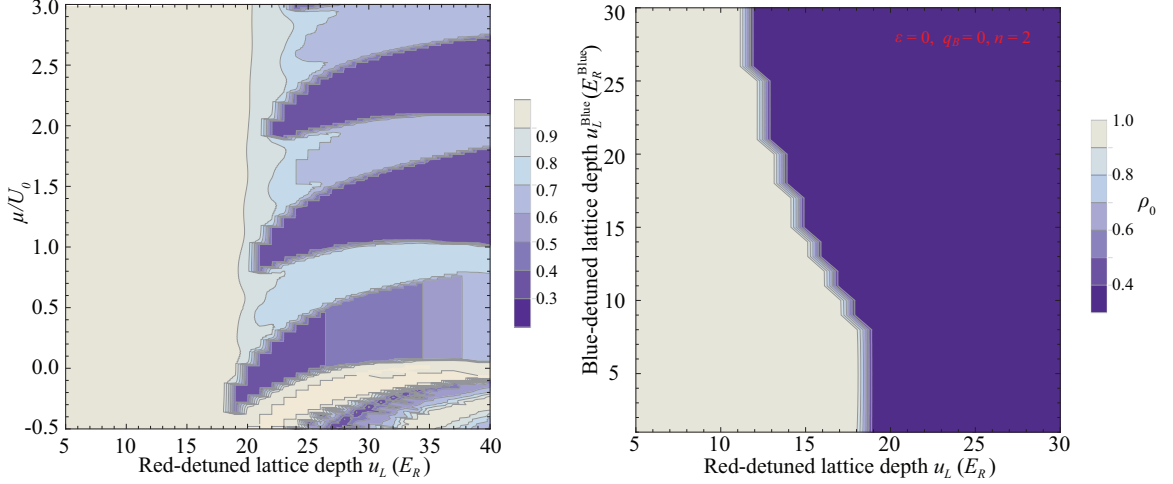


Figure 5.5: The MF ground state phase diagram at (a) $u_L^{\text{Blue}}/u_L = 0.5$ and (b) With μ/U_0 inside the $n = 2$ Mott lobe. In both panels, $\varepsilon = 0$ and $q_B = 0$.

the MI phase is only characterized by the total filling factor in an unit cell $n = n_L + n_R$. At low magnetic field, even filling Mott lobes favor spin singlet pairs with the spin gap induced by U_2 . Superlattice helps enlarge the even filling Mott lobes and shrink the odd fillings. When q_B is high enough the ground state becomes $m_F = 0$ state and the system shows similar behavior as scalar condensates. Based on fig. 5.5(b), when u_L^{Blue} increase to a suitable value, the change of the inside well barrier helps the phase transition to happen earlier.

5.3 Generation of spin entanglement between cold atoms in superlattices

There are several methods to generate entanglement using spinor bosonic gases in optical superlattices [142, 154, 156, 164]. Here I mainly discuss the intrinsic entangled state related to the ground state of our system, and the constructed entangled states via the dynamical processes between atoms in double wells.

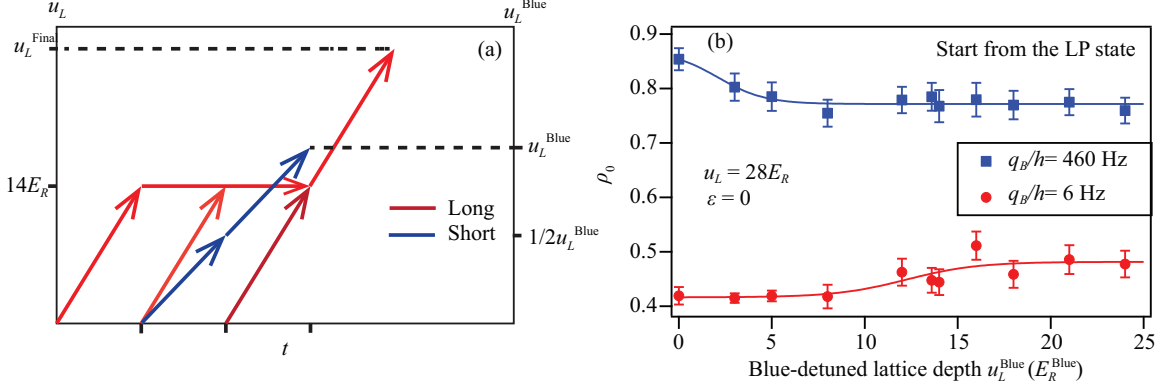


Figure 5.6: (a) Typical ramp sequence for all four lattice beams. All axes have arbitrary units (see text). (b) Measured ρ_0 versus u_L^{Blue} after an initial LP spinor BEC undergoes ramp-up sequences to $28E_R$ at $q_B/h = 6$ Hz (blue) and $q_B/h = 460$ Hz (red). The solid lines are sigmoid fits of the data to guide the eye.

5.3.1 Ground state of cold atoms in optical superlattices

We first study the ground state properties of cold atoms in the superlattice, as the MF theory predicts that superlattice help with increasing the even filling in the system, so does the fraction of spin singlets when q is small. With q fixed at a certain value we ramp u_L to $28E_R$ adiabatically so the system enters MI state and we change u_L^{Blue} during the ramp up sequence. To minimum the heating effect on atoms introduced by lattice beams, we do not ramp all lattice beams together but use a special ramp sequence. One typical example ramping the system to MI state, as Fig. 5.6(a) shows, is that the horizontal red-detuned lattice beam along the double-well axis first adiabatically ramps up to $\frac{1}{2}u_L^{\text{final}} = 14E_R$. Thereafter the other horizontal red-detuned lattice beam is ramped up to $14E_R$ and the blue-detuned lattice beam is ramped up to half of its final depth u_L^{Blue} at the same time, with the first lattice beam holding at $14E_R$. Then with the two red-detuned horizontal lattice beams holding at $14E_R$, the vertical lattice beam is ramped up to $14E_R$ while the blue-detuned lattice beam ramps to its final depth u_L^{Blue} . Finally three red-detuned lattice beams are ramped to final $u_L^{\text{final}} = 28E_R$ with 532 nm beam at fixed u_L^{Blue} so the system transits to the MI state. ρ_{mF} can be measure with the two-stage microwave imaging after a certain time of flight.

For data in Fig. 5.6(b), q_B/h is set at 6 Hz and 460 Hz. Within the scan region of u_L^{Blue} ,

the superlattice structure changes from double wells with shallow barriers to ideal double wells in our model. For the regular lattice case with $u_L^{\text{Blue}} = 0$ in Fig. 5.6, the values of ρ_0 are close to the MF predictions. Signature of transition shows up when u_L^{Blue} gradually increases as ρ_0 versus u_L^{Blue} data follow sigmoid fittings. The positions of the transition points are different for $q/h = 6$ Hz and $q/h = 460$ Hz, indicating the competition between J_i and q . However for 6 Hz data the ρ_0 is expected to be closer to $\frac{1}{3}$ when u_L^{Blue} increases since the singlet fraction is expected to be larger. The explanation of the data remains to be further explored. These data show that our superlattice system have its unique features to be explored, meanwhile there are q dependence data in the deep lattices show that the current system is limited by the lattice induced heating (not shown in the figures). Further cooling of atoms in such system is possible with the recent development of the cooling techniques [62, 141, 142]. The measurement of entanglement in the system can also help us understand its properties. A process shown in Fig. 5.4(c), as discussed in Ref. [119], is expected to help with creating $n = 2$ Mott lobe and to realize a larger fraction of spin singlets for antiferromagnetic spinor atoms in the optical superlattices.

5.3.2 Generation of entanglement with state manipulations

With the development of the techniques manipulating and addressing single atom spins in a many-atoms system (i.e. cold atoms in optical lattices), the generation of entanglement in such system has been realized [142, 164], and its applications to quantum information and quantum computing have attracted many interests [7]. I will discuss some of the generic techniques for state preparation, manipulation and detection of cold spinor atoms in the optical superlattice. The basic configuration for such system is usually two spinor atoms in a double well. Two certain spin states are chosen as the $|\uparrow\rangle$ and $|\downarrow\rangle$ states of a qubit. Usually the spin states need to have long lifetime and are interchangeable using a RF/microwave pulse or with exchange interaction [165]. For example Ref. [164] used $|\uparrow\rangle = |F = 2, m_F = -2\rangle$ and $|\downarrow\rangle = |F = 1, m_F = -1\rangle$ for ^{87}Rb and Ref. [158] chose $|\uparrow\rangle = |F = 1, m_F = 0\rangle$ and $|\downarrow\rangle = |F = 1, m_F = -1\rangle$. The initial spin state can be easily prepared at $|\downarrow\rangle$ for all atoms with a magnetic field gradient or a magnetic trap before lattice

loading. With unit filling after loading atoms in deep lattice, a double well structure with spin-dependent potential can be realized with a magnetic field gradient [158, 166]. Then the spin state can be manipulated selectively depending on whether the atom is located at the left or right site, as shown in Fig. 5.7(a). If a RF pulse is applied resonant with atoms on the left site, then the state in double well becomes $|\uparrow, \downarrow\rangle$, where the occupation of left or right site is represented by the position in the notation. Then dynamics can be initialized to demonstrate the quantum SWAP gate operation and to prepare entangled states, e.g. $(|\uparrow, \downarrow\rangle + i|\downarrow, \uparrow\rangle)/\sqrt{2}$ or $(|\uparrow, \downarrow\rangle + |\downarrow, \uparrow\rangle)/\sqrt{2}$.

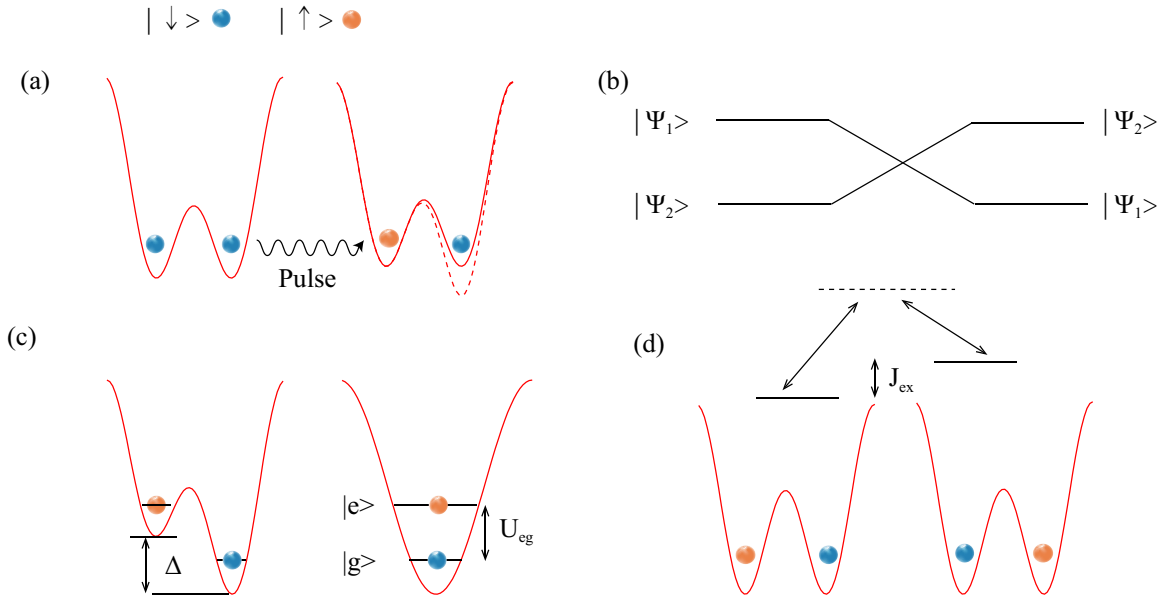


Figure 5.7: (a) Demonstration of the initial state preparation, only the spin on the left well is flipped by the RF/microwave pulse when an energy offset between the two wells is introduced, e.g. by applying a magnetic field gradient. (b) The graphical representation of the SWAP quantum gate. (c) Demonstration of the SWAP operation in [158], the left and right well have an energy offset Δ before merging, (see text). (d) Demonstration of another kind of super-exchange driven SWAP operation [142, 161, 164, 167], the high energy states with two atoms occupying the same well can only be the virtual intermediate states in second-order tunnelling processes, (see text).

Two methods have been experimentally demonstrated as Fig. 5.7 (c) and (d) show. In Ref. [158], when the double well with the initial state $|\uparrow, \downarrow\rangle$ is merged into a single site, the two atoms can occupy different vibrational bands, which can be expressed as $|\uparrow_e, \downarrow_g\rangle$. To maintain the symmetry of the two-particle bosonic wave function, the spatial component and the spin component have to be both symmetric or both anti-symmetric.

In the former case, two atoms overlap spatially, leading to collisional interaction $U_{eg} = (8\pi\hbar^2 a_s/m) \int |\phi_e(X)|^2 |\phi_g(X)|^2 d^3x$, where a_s is the s -wave scattering length, m is the mass, ϕ_i is the spatial wavefunction for the ground vibrational band (g) and the excited vibrational band (e). While for the latter case there is no spacial overlapping of the atoms hence no interaction between them. The symmetric (antisymmetric) case corresponds to the singlet (triplet) state, and there is an effective spin-spin interaction due to the energy difference. This leads to the oscillation between $|\uparrow_e, \downarrow_g\rangle$ and $|\downarrow_e, \uparrow_g\rangle$. This operation, shown in Fig. 5.7 (b), is called quantum SWAP gate in quantum computing, which could map a tensor product state to a tensor product state [165]. However, if the operation stops at the time $t_{\text{SWAP}}/2$, then the so called $\sqrt{\text{SWAP}}$ operation can map the tensor product state to an entangled state. To measure the state after evolution, a band mapping technique is combined with a magnetic field gradient during time-of-flight, so atoms on different bands are mapped onto different Brillouin zones and atoms with different spins are separated along another direction. The observed collisional swap dynamics shows clear oscillation over many periods with negligible decay [158].

The first method for SWAP operation needs to merge the two atoms into the same site, and the imperfect transfer to the desired vibrational bands limited the fidelity. Reference. [157] found a second-order tunnelling in such system and the related superexchange is a kind of non-local spin exchange [167]. When $U \gg J$, where J is the single-particle tunnelling energy and U is the interaction energy, $|\uparrow\downarrow, 0\rangle$ and $|0, \uparrow\downarrow\rangle$ can not be reached starting from $|\uparrow, \downarrow\rangle$ and the spin dynamics can be described as a Heisenberg-type effective spin Hamiltonian $\hat{\mathbf{H}} = -J_{\text{ex}} \hat{\mathbf{S}}_{\mathbf{L}} \cdot \hat{\mathbf{S}}_{\mathbf{R}}$, where $J_{\text{ex}} = 4J^2/U$ is a different kind of effective spin-spin interaction. Similar SWAP operation can be realized through the evolution from $|\uparrow, \downarrow\rangle$ to $|\downarrow, \uparrow\rangle$, without moving the atoms. The readout of final states can be achieved with the same band mapping plus a Stern-Gerlach filter [167], or by a two-stage filtering accompanied with the *in situ* absorption imaging for a two dimensional system [142, 164]. To count the number of atoms in singlet or triplet states in the latter one, a $\pi/2$ -pulse is applied so the triplet state become $(|\uparrow, \uparrow\rangle + |\downarrow, \downarrow\rangle)/\sqrt{2}$ while the singlet state remains the same. Then atoms in $|\uparrow\rangle$ state are counted with the first imaging pulse regardless of their position, and the rest $|\downarrow\rangle$ atoms are

transfer to a desired state with a microwave pulse, so $|\downarrow\rangle$ atom pairs escape the trap after merging the double well and holding the trap for sufficient time. The remain atoms are contributed by the singlet state only. With the help of precise measurement, Ref. [142, 164] are able to measure the spin correlations and entanglement.

After the preparation of Bell pairs in many double wells, the next step is to connect each other for a cluster state, one of the multi-particle entangled state that can be useful for the one-way quantum computer [39, 168]. The size of the cluster is crucial for implementation of the quantum algorithm since a sequence of measurements are carried out on a single atom [169, 170], and one of the limitation for neutral atoms in optical lattices is the defects like an empty lattice site due to the finite temperature. Progress has been made recently to greatly cool down such system and the measured entanglement fidelity is significantly improved [142].

The above discussed methods should be generic and practical for systems including our setup. Besides these protocols, we also propose some different methods to generate entanglement and spin squeezing: through coherent atomic collisions that naturally exist in spinor BECs, or through nonlinear interactions between atoms and a light field, which can be induced by a quantum non-demolition measurement (e.g., Faraday rotation spectroscopy) [20].

CHAPTER VI

FUTURE DIRECTIONS

Antiferromagnetic spinor BECs have been suggested as ideal candidate to generate entanglement and spin squeezing with. In the past twenty years, entanglement and spin squeezing in atomic systems have attracted much attention for applications in quantum information processing and quantum computing [39], as well as their potential abilities to significantly enhance the precision of spin-related measurements [8]. For example, our calculations predict that spin-squeezed sodium spinor BECs can be applied to develop an ultra-precise magnetic field sensor.

6.1 DiVincenzo's criteria for atom quantum computers

There are several promising physical systems with certain computational models for the realization of quantum computers, e.g. trapped ions [171], NMR quantum computer [172], superconducting quantum computer [173], neutral atoms [39] and etc. [165]. The necessary conditions for constructing a quantum computer proposed by David P. DiVincenzo in 2000 is the so-called DiVincenzo's criteria. There have been some evaluations of a neutral atom quantum computer based on these criteria or a generalized version a decade ago [165, 174, 175], while some new developments have been achieved since then. Thus I will briefly summarize the evaluations with some recent updates.

1. A scalable physical system with well characterized qubits:

Due to the properties of superposition and entanglement for qubits, the required number

of qubits to run a useful quantum computer is much less than the number of transistors in a classical one, yet certain scale for the qubit number from a few hundreds up to 10^4 is still necessary. The meaning of "well characterized" includes the understanding of the qubit's physical parameters, all states of the qubit and the coupling, the interaction between qubits and the response to the external fields, etc. For neutral atom, as discussed above, two atomic internal states can serve as the $|\downarrow\rangle$ and $|\uparrow\rangle$ states for a qubit. However, the many other states could be a problem if the working states leak to these states. When atoms are loaded to the optical lattices, the typical scale of the system is around 10^6 [39]. Unit filling can be achieved by the transition into a Mott-insulator state, and the quantum gas microscope allows the selective addressing of atoms in a single site [142].

2. The ability to initialize the state of the qubits to a simple fiducial state, such as $|000\dots\rangle$:

It is straightforward that initialization is the precondition for a trustworthy output, which is true for both quantum and classical quantum computing. Meanwhile continuous supply of qubits in a low-entropy state is a requirement for quantum error correction. The internal states spinor atoms can be reliably prepared by optical pumping or starting for a BEC then loading the optical lattices [165].

3. Long relevant decoherence times, much longer than the gate operation time:

The interaction between the quantum system and the environment introduce noise into the system, so the evolution of the quantum states can be different from the one in a perfect closed quantum system. Thus it is necessary to complete the required gate operations before the system becomes decoherent. This can be realized by increasing the decoherence time of the system or by speeding up the gate operations. It has been experimentally demonstrated that neutral atoms have long decoherence time, which is mainly due to the charge neutrality and depends on the methods for states preparation (e.g. many-body entangled states can be insensitive to the external perturbations). The decoherence time of such system is typical at tens of millisecond or longer and the gate operation time is around microsecond [142]. However, the decoherence induced by gate operation is a potential problem.

4. A universal set of quantum gates:

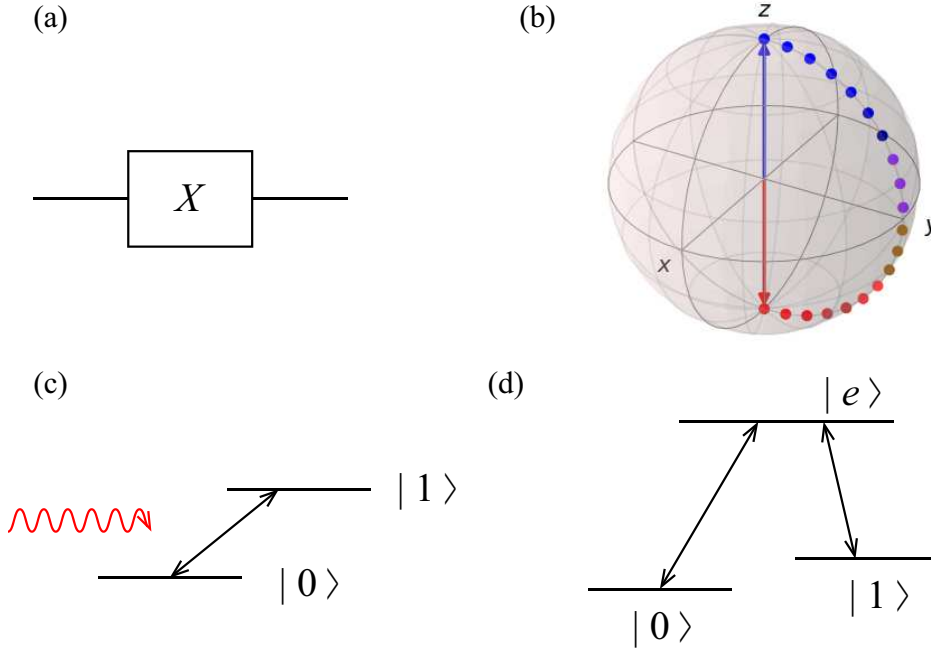


Figure 6.1: (a) The graphical representation of one of the single quantum gate: negation (NOT), which can be represented by the Pauli Matrix σ_x . (b) Gate operation of X in a Bloch sphere, it equals a π radians rotation along the x -axis. (c) Microwave induced Rabi oscillation can realize the single quantum gate operation. (d) Raman transition can also be used to implement the single qubit operation.

The universality theorem states that the set of single qubit gates and the CNOT gate can form a universal set of quantum circuits. In other words, any $U(2^n)$ gates can be re-expressed as sequences of single-qubit gates and CNOT gates [176, 177]. For measurement-based quantum computing, the universality refers to the 'universal resource' that could generate all states with single qubit operation [39], and the two dimensional cluster state appears to be one of the candidate [178–181]. The single qubit operations in neutral atoms can be realized by applying RF/microwave pulse as discussed or by Raman transitions as shown in Fig.6.1 (c) and (d). Reference [182] demonstrated their system's ability of operating CNOT gate among many qubits. The $\sqrt{\text{SWAP}}$ operation in the superlattice mentioned above, together with the single qubit rotations, are also claimed to be a set of universal gates [158, 183].

5. A qubit-specific measurement capability:

The readout of the result after operations usually require the measurement of the qubits or

some particular qubits. It has been explained in the last section on how imaging beam can selectively count the $|\uparrow\rangle$ or $|\downarrow\rangle$ atoms and how the complete spin correlated basis can be identified. An alternative method is the “quantum jump” [184, 185].

6. The ability to interconvert stationary and flying qubits:

The clear design of flying qubits is using photons. The conversion between atomic states and photons can be realized by quantum electrodynamics techniques.

7. The ability to faithfully transmit flying qubits between specified locations:

If the information is encoded in the photons, then the optical techniques can be used for transmitting.

To summarize, neutral atoms in optical lattices is a very promising platform for building quantum computers. Although its current development is a bit slower than some other systems like trapped ions or superconducting circuits, it has the unique advantage, especially the large scale, to be one of the few best candidate in the future.

6.2 Applications of spinor gases in quantum magnetometry

Magnetometry with high spatial resolution (micrometer) and high field sensitivity (picotesla or even femtotesla) has its application to a wide variety of fields ranging from fundamental science [186], to engineering [187], to medicine [188, 189], and to space science [190–192]. Atomic magnetometer has been studied ever since the development of manipulating atoms with laser. Both hot atomic vapors and versatile cold atomic gases have been investigated, among them a spinor BEC system has many unique advantages as a clean and well-controlled system [8]. Reference. [193] has demonstrated the ability of their $F = 1$ ^{87}Rb BEC with a $120\ \mu\text{m}^2$ spatial resolution and a $8.3\ \text{pT}/\text{Hz}^{1/2}$ field sensitivity.

The underlying principle is usually the Larmor precession expressed as [194]:

$$\omega_L = 2\pi\nu_L = \frac{g_F\mu_B}{\hbar} |\mathbf{B}|, \quad (6.1)$$

where ω_L is the Larmor frequency, g_F is the Landé- g factor, μ_B is the Bohr magneton. So the sensitivity is characterized by $\Delta\nu$, the width of the resonance in the experiment. For example the coherence time in spin polarized atomic magnetometer give a limitation of such system. There are other fundamental limitations like the quantum limits including atomic projection noise, photon shot noise and energy resolution limits [10, 192]. Proposals have been brought forward to surpass some of these limitations [10, 192, 195], and the realization of entanglement and squeezing are essential.

Spinor cold atom systems with spin squeezing are proposed with their resolution below the atomic shot-noise limits [196, 197]. Our calculations also indicate that optical lattices can be used to create much greater spin squeezing, since lattices can largely enhance interatomic interactions and suppress tunnelling among lattice sites. Criteria for a quantum system to work as a quantum sensor have been listed and three DiVincenzo criteria are also included [195], so building a quantum computer shared many properties in common with realizing a quantum sensor, and the discussions above, the recent advances of entanglement generation in lattice confined atoms system, also have the potential to be used in metrology [39].

In conclusion, the advances of new techniques and theories make the spinor BEC a good candidate to study non-equilibrium dynamics and more topics related to this. While some universality and integrability has been found in the complicated strong-interacting many-body systems, more questions remain to be solved. Theories will guide the experiments while the experimental researches could also support the development of theories in many aspects, as it has happened in the development of cold atomic physics.

REFERENCES

- [1] A. Einstein. Quantentheorie des einatomigen idealen gases. *Sitzungsberichte der Preussischen Akademie der Wissenschaften*, 1:3, 1925.
- [2] V. I. Yukalov. Basics of bose-einstein condensation. *Physics of Particles and Nuclei*, 42(3):460–513, May 2011.
- [3] M. H. Anderson, J. R. Ensher, M. R. Matthews, C. E. Wieman, and E. A. Cornell. Observation of bose-einstein condensation in a dilute atomic vapor. *Science*, 269(5221):198, Jul 14 1995. - Copyright American Association for the Advancement of Science Jul 14, 1995; - 2010-06-08; CODEN - SCIEAS.
- [4] K. B. Davis, M. O. Mewes, M. R. Andrews, N. J. van Druten, D. S. Durfee, D. M. Kurn, and W. Ketterle. Bose-einstein condensation in a gas of sodium atoms. *Phys. Rev. Lett.*, 75:3969–3973, Nov 1995.
- [5] C. C. Bradley, C. A. Sackett, J. J. Tollett, and R. G. Hulet. Evidence of bose-einstein condensation in an atomic gas with attractive interactions. *Phys. Rev. Lett.*, 75:1687–1690, Aug 1995.
- [6] S. L. Cornish, N. R. Claussen, J. L. Roberts, E. A. Cornell, and C. E. Wieman. Stable ^{85}Rb bose-einstein condensates with widely tunable interactions. *Phys. Rev. Lett.*, 85:1795–1798, Aug 2000.
- [7] Immanuel Bloch, Jean Dalibard, and Wilhelm Zwerger. Many-body physics with ultracold gases. *Rev. Mod. Phys.*, 80:885–964, Jul 2008.
- [8] Dan M. Stamper-Kurn and Masahito Ueda. Spinor bose gases: Symmetries, magnetism, and quantum dynamics. *Rev. Mod. Phys.*, 85:1191–1244, Jul 2013.

- [9] D. Jaksch and P. Zoller. The cold atom hubbard toolbox. *Annals of Physics*, 315(1):52 – 79, 2005. Special Issue.
- [10] Luca Pezzè, Augusto Smerzi, Markus K. Oberthaler, Roman Schmied, and Philipp Treutlein. Quantum metrology with nonclassical states of atomic ensembles. *Rev. Mod. Phys.*, 90:035005, Sep 2018.
- [11] Dmitry A. Abanin, Ehud Altman, Immanuel Bloch, and Maksym Serbyn. Colloquium: Many-body localization, thermalization, and entanglement. *Rev. Mod. Phys.*, 91:021001, May 2019.
- [12] D. M. Stamper-Kurn, M. R. Andrews, A. P. Chikkatur, S. Inouye, H.-J. Miesner, J. Stenger, and W. Ketterle. Optical confinement of a bose-einstein condensate. *Phys. Rev. Lett.*, 80:2027–2030, Mar 1998.
- [13] Tin-Lun Ho. Spinor bose condensates in optical traps. *Phys. Rev. Lett.*, 81:742–745, Jul 1998.
- [14] W.-J. Huang and S.-C. Gou. Ground-state energy of the spinor bose-einstein condensate. *Phys. Rev. A*, 59:4608–4613, Jun 1999.
- [15] Masahito Ueda. Many-body theory of dilute bose-einstein condensates with internal degrees of freedom. *Phys. Rev. A*, 63:013601, Dec 2000.
- [16] Takeshi Mizushima, Kazushige Machida, and Takafumi Kita. Continuous vortices and collective excitations in ferromagnetic spinor bose–einstein condensates. *Physica B: Condensed Matter*, 329:17–18, 2003.
- [17] Qiang Gu and Richard A Klemm. Ferromagnetic phase transition and bose-einstein condensation in spinor bose gases. *Physical Review A*, 68(3):031604, 2003.
- [18] A. T. Black, E. Gomez, L. D. Turner, S. Jung, and P. D. Lett. Spinor dynamics in an antiferromagnetic spin-1 condensate. *Phys. Rev. Lett.*, 99:070403, Aug 2007.
- [19] Ming-Shien Chang, Qishu Qin, Wenxian Zhang, Li You, and Michael S. Chapman.

- Coherent spinor dynamics in a spin-1 bosecondensate. *Nature Physics*, 1(2):111–116, Nov 2005.
- [20] Y. Liu, S. Jung, S. E. Maxwell, L. D. Turner, E. Tiesinga, and P. D. Lett. Quantum phase transitions and continuous observation of spinor dynamics in an antiferromagnetic condensate. *Phys. Rev. Lett.*, 102:125301, Mar 2009.
- [21] J. Stenger, S. Inouye, D. M. Stamper-Kurn, H.-J. Miesner, A. P. Chikkatur, and W. Ketterle. Spin domains in ground-state bose-einstein condensates. *Nature*, 396(6709):345–348, Nov 1998.
- [22] J. Jiang, L. Zhao, M. Webb, and Y. Liu. Mapping the phase diagram of spinor condensates via adiabatic quantum phase transitions. *Phys. Rev. A*, 90:023610, Aug 2014.
- [23] A. Görlitz, T. L. Gustavson, A. E. Leanhardt, R. Löw, A. P. Chikkatur, S. Gupta, S. Inouye, D. E. Pritchard, and W. Ketterle. Sodium bose-einstein condensates in the $f = 2$ state in a large-volume optical trap. *Phys. Rev. Lett.*, 90:090401, Mar 2003.
- [24] G. Breit and I. I. Rabi. Measurement of nuclear spin. *Phys. Rev.*, 38:2082–2083, Dec 1931.
- [25] Lichao Zhao. *Antiferromagnetic spinor condensates in microwave dressing fields and optical lattices*. PhD thesis, Oklahoma State University, 2015.
- [26] Daniel A Steck. Sodium d line data. *Report, Los Alamos National Laboratory, Los Alamos*, 124:74, 2000.
- [27] L. Zhao, J. Jiang, T. Tang, M. Webb, and Y. Liu. Dynamics in spinor condensates tuned by a microwave dressing field. *Phys. Rev. A*, 89:023608, Feb 2014.
- [28] Fabrice Gerbier, Artur Widera, Simon Fölling, Olaf Mandel, and Immanuel Bloch. Resonant control of spin dynamics in ultracold quantum gases by microwave dressing. *Phys. Rev. A*, 73:041602, Apr 2006.
- [29] Sabrina R. A. Leslie. *On Spinor Condensates as Amplifiers, Sensors and Tunable Quan-*

- tum Playgrounds for Studies of Spin*. PhD thesis, University of California, Berkeley, 2008.
- [30] Tetsuo Ohmi and Kazushige Machida. Bose-einstein condensation with internal degrees of freedom in alkali atom gases. *Journal of the Physical Society of Japan*, 67(6):1822–1825, 1998.
- [31] C. K. Law, H. Pu, and N. P. Bigelow. Quantum spins mixing in spinor bose-einstein condensates. *Phys. Rev. Lett.*, 81:5257–5261, Dec 1998.
- [32] Wenxian Zhang, D. L. Zhou, M.-S. Chang, M. S. Chapman, and L. You. Coherent spin mixing dynamics in a spin-1 atomic condensate. *Phys. Rev. A*, 72:013602, Jul 2005.
- [33] E. M. Bookjans, A. Vinit, and C. Raman. Quantum phase transition in an antiferromagnetic spinor bose-einstein condensate. *Phys. Rev. Lett.*, 107:195306, Nov 2011.
- [34] Tin-Lun Ho and Sung Kit Yip. Fragmented and single condensate ground states of spin-1 bose gas. *Phys. Rev. Lett.*, 84:4031–4034, May 2000.
- [35] N. Behbood, F. Martin Ciurana, G. Colangelo, M. Napolitano, Géza Tóth, R. J. Sewell, and M. W. Mitchell. Generation of macroscopic singlet states in a cold atomic ensemble. *Phys. Rev. Lett.*, 113:093601, Aug 2014.
- [36] L. Zhao, T. Tang, Z. Chen, and Y. Liu. Lattice-induced rapid formation of spin singlets in spin-1 spinor condensates, 2018.
- [37] Andrei Derevianko and Hidetoshi Katori. Colloquium: Physics of optical lattice clocks. *Rev. Mod. Phys.*, 83:331–347, May 2011.
- [38] V Ahufinger, A Mebrahtu, R Corbalán, and A Sanpera. Quantum switches and quantum memories for matter-wave lattice solitons. *New Journal of Physics*, 9(1):4, 2007.
- [39] Immanuel Bloch. Quantum coherence and entanglement with ultracold atoms in optical lattices. *Nature*, 453(7198):1016–1022, Jun 2008.

- [40] I. M. Georgescu, S. Ashhab, and Franco Nori. Quantum simulation. *Rev. Mod. Phys.*, 86:153–185, Mar 2014.
- [41] Patrick A. Lee, Naoto Nagaosa, and Xiao-Gang Wen. Doping a mott insulator: Physics of high-temperature superconductivity. *Rev. Mod. Phys.*, 78:17–85, Jan 2006.
- [42] Markus Greiner, Olaf Mandel, Tilman Esslinger, Theodor W. Hansch, and Immanuel Bloch. Quantum phase transition from a superfluid to a mott insulator in a gas of ultracold atoms. *Nature*, 415(6867):39–44, Jan 2002.
- [43] Eugene Demler and Fei Zhou. Spinor bosonic atoms in optical lattices: Symmetry breaking and fractionalization. *Phys. Rev. Lett.*, 88:163001, Apr 2002.
- [44] Adilet Imambekov, Mikhail Lukin, and Eugene Demler. Spin-exchange interactions of spin-one bosons in optical lattices: Singlet, nematic, and dimerized phases. *Phys. Rev. A*, 68:063602, Dec 2003.
- [45] Artur Widera, Fabrice Gerbier, Simon Fölling, Tatjana Gericke, Olaf Mandel, and Immanuel Bloch. Coherent collisional spin dynamics in optical lattices. *Phys. Rev. Lett.*, 95:190405, Nov 2005.
- [46] K. W. Mahmud and E. Tiesinga. Dynamics of spin-1 bosons in an optical lattice: Spin mixing, quantum-phase-revival spectroscopy, and effective three-body interactions. *Phys. Rev. A*, 88:023602, Aug 2013.
- [47] K. V. Krutitsky, M. Timmer, and R. Graham. First- and second-order superfluid–mott-insulator phase transitions of spin-1 bosons with coupled ground states in optical lattices. *Phys. Rev. A*, 71:033623, Mar 2005.
- [48] Takashi Kimura, Shunji Tsuchiya, and Susumu Kurihara. Possibility of a first-order superfluid–mott-insulator transition of spinor bosons in an optical lattice. *Phys. Rev. Lett.*, 94:110403, Mar 2005.
- [49] G. G. Batrouni, V. G. Rousseau, and R. T. Scalettar. Magnetic and superfluid transitions in the one-dimensional spin-1 boson hubbard model. *Phys. Rev. Lett.*, 102:140402, Apr 2009.

- [50] Zhi Li, Ai-Xia Zhang, Juan Ma, and Ju-Kui Xue. Coherent spin-mixing and wave packets dynamics of spin-1 condensates in optical lattices. *Physics Letters A*, 374(13-14):1401–1406, 2010.
- [51] Claude N. Cohen-Tannoudji. Nobel lecture: Manipulating atoms with photons. *Rev. Mod. Phys.*, 70:707–719, Jul 1998.
- [52] Markus Greiner. *Ultracold quantum gases in three-dimensional optical lattice potentials*. PhD thesis, Ludwig-Maximilians-Universitt Mnchen, April 2003.
- [53] Felix Bloch. über die quantenmechanik der elektronen in kristallgittern. *Zeitschrift für Physik*, 52(7-8):555–600, 1929.
- [54] J. Hubbard. Electron correlations in narrow energy bands. *Proceedings of the Royal Society of London A: Mathematical, Physical and Engineering Sciences*, 276(1365):238–257, 1963.
- [55] H. A. Gersch and G. C. Knollman. Quantum cell model for bosons. *Phys. Rev.*, 129:959–967, Jan 1963.
- [56] Matthew P. A. Fisher, Peter B. Weichman, G. Grinstein, and Daniel S. Fisher. Boson localization and the superfluid-insulator transition. *Phys. Rev. B*, 40:546–570, Jul 1989.
- [57] D. Jaksch, C. Bruder, J. I. Cirac, C. W. Gardiner, and P. Zoller. Cold bosonic atoms in optical lattices. *Phys. Rev. Lett.*, 81:3108–3111, Oct 1998.
- [58] N. Elstner and H. Monien. Dynamics and thermodynamics of the bose-hubbard model. *Phys. Rev. B*, 59:12184–12187, May 1999.
- [59] P. Buonsante and A. Vezzani. Phase diagram for ultracold bosons in optical lattices and superlattices. *Phys. Rev. A*, 70:033608, Sep 2004.
- [60] Subir Sachdev. *Quantum Phase Transitions*. Cambridge University Press, 2 edition, 2011.
- [61] S. Trotzky, L. Pollet, F. Gerbier, U. Schnorrberger, I. Bloch, N. V. Prokof'ev, B. Svis-

- tunov, and M. Troyer. Suppression of the critical temperature for superfluidity near the mott transition. *Nature Physics*, 6(12):998–1004, Dec 2010.
- [62] D C McKay and B DeMarco. Cooling in strongly correlated optical lattices: prospects and challenges. *Reports on Progress in Physics*, 74(5):054401, apr 2011.
- [63] Yongqiang Li, Liang He, and Walter Hofstetter. Magnetic phase transitions of spin-1 ultracold bosons in a cubic optical lattice. *Phys. Rev. A*, 93:033622, Mar 2016.
- [64] V. A. Kashurnikov, N. V. Prokof’ev, and B. V. Svistunov. Revealing the superfluid–mott-insulator transition in an optical lattice. *Phys. Rev. A*, 66:031601, Sep 2002.
- [65] Simon Fölling, Artur Widera, Torben Müller, Fabrice Gerbier, and Immanuel Bloch. Formation of spatial shell structure in the superfluid to mott insulator transition. *Phys. Rev. Lett.*, 97:060403, Aug 2006.
- [66] Gretchen K. Campbell, Jongchul Mun, Micah Boyd, Patrick Medley, Aaron E. Leanhardt, Luis G. Marcassa, David E. Pritchard, and Wolfgang Ketterle. Imaging the mott insulator shells by using atomic clock shifts. *Science*, 313(5787):649–652, 2006.
- [67] Z. Chen, T. Tang, J. Austin, Z. Shaw, L. Zhao, and Y. Liu. Quantum quench and nonequilibrium dynamics in lattice-confined spinor condensates. *Phys. Rev. Lett.*, 123:113002, Sep 2019.
- [68] J. Jiang, L. Zhao, S.-T. Wang, Z. Chen, T. Tang, L.-M. Duan, and Y. Liu. First-order superfluid-to-mott-insulator phase transitions in spinor condensates. *Phys. Rev. A*, 93:063607, Jun 2016.
- [69] Ramesh V. Pai, K. Sheshadri, and Rahul Pandit. Phases and transitions in the spin-1 bose-hubbard model: Systematics of a mean-field theory. *Phys. Rev. B*, 77:014503, Jan 2008.
- [70] Daisuke Yamamoto, Takeshi Ozaki, Carlos A. R. Sá de Melo, and Ippei Danshita. First-order phase transition and anomalous hysteresis of bose gases in optical lattices. *Phys. Rev. A*, 88:033624, Sep 2013.

- [71] Anatoli Polkovnikov, Krishnendu Sengupta, Alessandro Silva, and Mukund Vengalattore. Colloquium: Nonequilibrium dynamics of closed interacting quantum systems. *Rev. Mod. Phys.*, 83:863–883, Aug 2011.
- [72] Corinna Kollath, Andreas M. Läuchli, and Ehud Altman. Quench dynamics and nonequilibrium phase diagram of the bose-hubbard model. *Phys. Rev. Lett.*, 98:180601, Apr 2007.
- [73] Ryan Barnett, Anatoli Polkovnikov, and Mukund Vengalattore. Prethermalization in quenched spinor condensates. *Phys. Rev. A*, 84:023606, Aug 2011.
- [74] Tim Langen, Remi Geiger, and Jrg Schmiedmayer. Ultracold atoms out of equilibrium. *Annual Review of Condensed Matter Physics*, 6(1):201–217, 2015.
- [75] P Braun-Munzinger, D Magestro, K Redlich, and J Stachel. Hadron production in au–au collisions at rhic. *Physics Letters B*, 518(1-2):41–46, 2001.
- [76] J. Berges, Sz. Borsányi, and C. Wetterich. Prethermalization. *Phys. Rev. Lett.*, 93:142002, Sep 2004.
- [77] Lev Kofman, Andrei Linde, and Alexei A. Starobinsky. Reheating after inflation. *Phys. Rev. Lett.*, 73:3195–3198, Dec 1994.
- [78] Dmitry Podolsky, Gary N Felder, Lev Kofman, and Marco Peloso. Equation of state and beginning of thermalization after preheating. *Physical Review D*, 73(2):023501, 2006.
- [79] Edward Farhi, Jeffrey Goldstone, Sam Gutmann, Joshua Lapan, Andrew Lundgren, and Daniel Preda. A quantum adiabatic evolution algorithm applied to random instances of an np-complete problem. *Science*, 292(5516):472–475, 2001.
- [80] M. Anquez, B. A. Robbins, H. M Bharath, M. Boguslawski, T. M. Hoang, and M. S. Chapman. Quantum kibble-zurek mechanism in a spin-1 bose-einstein condensate. *Phys. Rev. Lett.*, 116:155301, Apr 2016.

- [81] Markus Heyl. Dynamical quantum phase transitions: a review. *Reports on Progress in Physics*, 81(5):054001, 2018.
- [82] André Eckardt. Colloquium: Atomic quantum gases in periodically driven optical lattices. *Reviews of Modern Physics*, 89(1):011004, 2017.
- [83] Christian Schweizer, Fabian Grusdt, Moritz Berngruber, Luca Barbiero, Eugene Demler, Nathan Goldman, Immanuel Bloch, and Monika Aidelsburger. Floquet approach to 2 lattice gauge theories with ultracold atoms in optical lattices. *Nature Physics*, 15(11):1168–1173, Nov 2019.
- [84] Jiazhong Hu, Lei Feng, Zhendong Zhang, and Cheng Chin. Quantum simulation of unruh radiation. *Nature Physics*, 15(8):785–789, Aug 2019.
- [85] Yang-Yang Chen, Pengfei Zhang, Wei Zheng, Zhigang Wu, and Hui Zhai. Many-body echo. *Phys. Rev. A*, 102:011301, Jul 2020.
- [86] Antonio Rubio-Abadal, Matteo Ippoliti, Simon Hollerith, David Wei, Jun Rui, S. L. Sondhi, Vedika Khemani, Christian Gross, and Immanuel Bloch. Floquet prethermalization in a bose-hubbard system. *Phys. Rev. X*, 10:021044, May 2020.
- [87] A Griessner, AJ Daley, SR Clark, Dieter Jaksch, and Peter Zoller. Dissipative dynamics of atomic hubbard models coupled to a phonon bath: dark state cooling of atoms within a bloch band of an optical lattice. *New Journal of Physics*, 9(2):44, 2007.
- [88] G. Barontini, R. Labouvie, F. Stubenrauch, A. Vogler, V. Guarrera, and H. Ott. Controlling the dynamics of an open many-body quantum system with localized dissipation. *Phys. Rev. Lett.*, 110:035302, Jan 2013.
- [89] Takafumi Tomita, Shuta Nakajima, Ippei Danshita, Yosuke Takasu, and Yoshiro Takahashi. Observation of the mott insulator to superfluid crossover of a driven-dissipative bose-hubbard system. *Science advances*, 3(12):e1701513, 2017.
- [90] Jiaming Li, Andrew K Harter, Ji Liu, Leonardo de Melo, Yogesh N Joglekar, and Le Luo. Observation of parity-time symmetry breaking transitions in a dissipative floquet system of ultracold atoms. *Nature communications*, 10(1):1–7, 2019.

- [91] Lei Pan, Xin Chen, Yu Chen, and Hui Zhai. Non-hermitian linear response theory. *Nature Physics*, 16(7):767–771, Jul 2020.
- [92] Artur Widera, Fabrice Gerbier, Simon Flling, Tatjana Gericke, Olaf Mandel, and Immanuel Bloch. Precision measurement of spin-dependent interaction strengths for spin-1 and spin-287rb atoms. *New Journal of Physics*, 8(8):152–152, aug 2006.
- [93] Aixi Chen, Wanying Qiu, and Zhiping Wang. Exact analytical solution for quantum spins mixing in spin-1 bose–einstein condensates. *Chinese Physics. B*, 17(11):4204–4206, 2008.
- [94] Ceren B. Dağ, Sheng-Tao Wang, and L.-M. Duan. Classification of quench-dynamical behaviors in spinor condensates. *Phys. Rev. A*, 97:023603, Feb 2018.
- [95] L. E. Sadler, J. M. Higbie, S. R. Leslie, M. Vengalattore, and D. M. Stamper-Kurn. Spontaneous symmetry breaking in a quenched ferromagnetic spinor bose-einstein condensate. *Nature*, 443(7109):312–315, Sep 2006.
- [96] Seji Kang, Sang Won Seo, Hiromitsu Takeuchi, and Y. Shin. Observation of wall-vortex composite defects in a spinor bose-einstein condensate. *Phys. Rev. Lett.*, 122:095301, Mar 2019.
- [97] Max F. Riedel, Pascal Böhi, Yun Li, Theodor W. Hänsch, Alice Sinatra, and Philipp Treutlein. Atom-chip-based generation of entanglement for quantum metrology. *Nature*, 464(7292):1170–1173, Apr 2010.
- [98] C. D. Hamley, C. S. Gerving, T. M. Hoang, E. M. Bookjans, and M. S. Chapman. Spin-nematic squeezed vacuum in a quantum gas. *Nature Physics*, 8(4):305–308, Apr 2012.
- [99] H.-X. Yang, T. Tian, Y.-B. Yang, L.-Y. Qiu, H.-Y. Liang, A.-J. Chu, C. B. Dağ, Y. Xu, Y. Liu, and L.-M. Duan. Observation of dynamical quantum phase transitions in a spinor condensate. *Phys. Rev. A*, 100:013622, Jul 2019.
- [100] T. Tian, H.-X. Yang, L.-Y. Qiu, H.-Y. Liang, Y.-B. Yang, Y. Xu, and L.-M. Duan.

- Observation of dynamical quantum phase transitions with correspondence in an excited state phase diagram. *Phys. Rev. Lett.*, 124:043001, Jan 2020.
- [101] Jae-yoon Choi, Sebastian Hild, Johannes Zeiher, Peter Schauß, Antonio Rubio-Abadal, Tarik Yefsah, Vedika Khemani, David A. Huse, Immanuel Bloch, and Christian Gross. Exploring the many-body localization transition in two dimensions. *Science*, 352(6293):1547–1552, 2016.
- [102] J. Jiang, L. Zhao, M. Webb, N. Jiang, H. Yang, and Y. Liu. Simple and efficient all-optical production of spinor condensates. *Phys. Rev. A*, 88:033620, Sep 2013.
- [103] L.-Y. Qiu, H.-Y. Liang, Y.-B. Yang, H.-X. Yang, T. Tian, Y. Xu, and L.-M. Duan. Observation of generalized kibble-zurek mechanism across a first-order quantum phase transition in a spinor condensate. *Science Advances*, 6(21), 2020.
- [104] D. M. Stamper-Kurn, M. R. Andrews, A. P. Chikkatur, S. Inouye, H.-J. Miesner, J. Stenger, and W. Ketterle. Optical confinement of a bose-einstein condensate. *Phys. Rev. Lett.*, 80:2027–2030, Mar 1998.
- [105] J Hecker Denschlag, J E Simsarian, H Hffner, C McKenzie, A Browaeys, D Cho, K Helmerson, S L Rolston, and W D Phillips. A bose-einstein condensate in an optical lattice. *Journal of Physics B: Atomic, Molecular and Optical Physics*, 35(14):3095, 2002.
- [106] C Becker, P Soltan-Panahi, J Kronjger, S Drscher, K Bongs, and K Sengstock. Ultracold quantum gases in triangular optical lattices. *New Journal of Physics*, 12(6):065025, jun 2010.
- [107] Maciej Lewenstein, Anna Sanpera, Veronica Ahufinger, Bogdan Damski, Aditi Sen, and Ujjwal Sen. Ultracold atomic gases in optical lattices: mimicking condensed matter physics and beyond. *Advances in Physics*, 56(2):243–379, 2007.
- [108] A. de Paz, A. Sharma, A. Chotia, E. Maréchal, J. H. Huckans, P. Pedri, L. Santos, O. Gorceix, L. Vernac, and B. Laburthe-Tolra. Nonequilibrium quantum magnetism in a dipolar lattice gas. *Phys. Rev. Lett.*, 111:185305, Oct 2013.

- [109] Johannes Zeiher, Jae-yoon Choi, Antonio Rubio-Abadal, Thomas Pohl, Rick van Bijnen, Immanuel Bloch, and Christian Gross. Coherent many-body spin dynamics in a long-range interacting ising chain. *Phys. Rev. X*, 7:041063, Dec 2017.
- [110] H. Pu, C. K. Law, S. Raghavan, J. H. Eberly, and N. P. Bigelow. Spin-mixing dynamics of a spinor bose-einstein condensate. *Phys. Rev. A*, 60:1463–1470, Aug 1999.
- [111] J. Kronjäger, C. Becker, P. Navez, K. Bongs, and K. Sengstock. Magnetically tuned spin dynamics resonance. *Phys. Rev. Lett.*, 97:110404, Sep 2006.
- [112] Y. Liu, E. Gomez, S. E. Maxwell, L. D. Turner, E. Tiesinga, and P. D. Lett. Number fluctuations and energy dissipation in sodium spinor condensates. *Phys. Rev. Lett.*, 102:225301, Jun 2009.
- [113] Artur Widera. *Constructing Correlated Spin States with Neutral Atoms in Optical Lattices*. PhD thesis, Johannes Gutenberg-Universitt, 2007.
- [114] L. Zhao, J. Jiang, T. Tang, M. Webb, and Y. Liu. Antiferromagnetic spinor condensates in a two-dimensional optical lattice. *Phys. Rev. Lett.*, 114:225302, Jun 2015.
- [115] Nguyen Thanh Phuc, Yuki Kawaguchi, and Masahito Ueda. Effects of thermal and quantum fluctuations on the phase diagram of a spin-1 ^{87}rb bose-einstein condensate. *Phys. Rev. A*, 84:043645, Oct 2011.
- [116] Markus Greiner, Olaf Mandel, Theodor W. Hänsch, and Immanuel Bloch. Collapse and revival of the matter wave field of a bose-einstein condensate. *Nature*, 419(6902):51–54, Sep 2002.
- [117] J. Schachenmayer, A. J. Daley, and P. Zoller. Atomic matter-wave revivals with definite atom number in an optical lattice. *Phys. Rev. A*, 83:043614, Apr 2011.
- [118] Sebastian Will, Thorsten Best, Ulrich Schneider, Lucia Hackermüller, Dirk-Sören Lühmann, and Immanuel Bloch. Time-resolved observation of coherent multi-body interactions in quantum phase revivals. *Nature*, 465(7295):197–201, May 2010.
- [119] J. Sebby-Strabley, B. L. Brown, M. Anderlini, P. J. Lee, W. D. Phillips, J. V. Porto,

- and P. R. Johnson. Preparing and probing atomic number states with an atom interferometer. *Phys. Rev. Lett.*, 98:200405, May 2007.
- [120] Simon Braun, Mathis Friesdorf, Sean S. Hodgman, Michael Schreiber, Jens Philipp Ronzheimer, Arnau Riera, Marco del Rey, Immanuel Bloch, Jens Eisert, and Ulrich Schneider. Emergence of coherence and the dynamics of quantum phase transitions. *Proceedings of the National Academy of Sciences*, 112(12):3641–3646, 2015.
- [121] F. A. van Abeelen and B. J. Verhaar. Determination of collisional properties of cold na atoms from analysis of bound-state photoassociation and feshbach resonance field data. *Phys. Rev. A*, 59:578–584, Jan 1999.
- [122] Crubellier, A., Dulieu, O., Masnou-Seeuws, F., Elbs, M., Knöckel, H., and Tiemann, E. Simple determination of na2 scattering lengths using observed bound levels at the ground state asymptote. *Eur. Phys. J. D*, 6(2):211–220, 1999.
- [123] S. Knoop, T. Schuster, R. Scelle, A. Trautmann, J. Appmeier, M. K. Oberthaler, E. Tiesinga, and E. Tiemann. Feshbach spectroscopy and analysis of the interaction potentials of ultracold sodium. *Phys. Rev. A*, 83:042704, Apr 2011.
- [124] C. Samuelis, E. Tiesinga, T. Laue, M. Elbs, H. Knöckel, and E. Tiemann. Cold atomic collisions studied by molecular spectroscopy. *Phys. Rev. A*, 63:012710, Dec 2000.
- [125] Kazuya Fujimoto and Makoto Tsubota. Spin turbulence with small spin magnitude in spin-1 spinor bose-einstein condensates. *Phys. Rev. A*, 88:063628, Dec 2013.
- [126] Justin Lovegrove, Magnus O. Borgh, and Janne Ruostekoski. Energetic stability of coreless vortices in spin-1 bose-einstein condensates with conserved magnetization. *Phys. Rev. Lett.*, 112:075301, Feb 2014.
- [127] S. Yi and H. Pu. Spontaneous spin textures in dipolar spinor condensates. *Phys. Rev. Lett.*, 97:020401, Jul 2006.
- [128] Jasper S. Krauser, Jannes Heinze, Nick Fläschner, Sören Götze, Ole Jürgensen, Dirk-Sören Lühmann, Christoph Becker, and Klaus Sengstock. Coherent multi-flavour spin dynamics in a fermionic quantum gas. *Nature Physics*, 8(11):813–818, Nov 2012.

- [129] Ehud Altman and Assa Auerbach. Oscillating superfluidity of bosons in optical lattices. *Phys. Rev. Lett.*, 89:250404, Dec 2002.
- [130] Shainen M. Davidson and Anatoli Polkovnikov. $su(3)$ semiclassical representation of quantum dynamics of interacting spins. *Phys. Rev. Lett.*, 114:045701, Jan 2015.
- [131] E. Tiesinga and P. R. Johnson. Collapse and revival dynamics of number-squeezed superfluids of ultracold atoms in optical lattices. *Phys. Rev. A*, 83:063609, Jun 2011.
- [132] T W B Kibble. Topology of cosmic domains and strings. *Journal of Physics A: Mathematical and General*, 9(8):1387–1398, aug 1976.
- [133] T. W. B. Kibble. Some implications of a cosmological phase transition. *Physics Reports*, 67(1):183–199, Dec 1980.
- [134] W. H. Zurek. Cosmological experiments in superfluid helium? *Nature*, 317(6037):505–508, Oct 1985.
- [135] Wojciech H Zurek. Cosmic strings in laboratory superfluids and the topological remnants of other phase transitions. *Acta physica Polonica. B*, 24(7):1301–1311, 1993.
- [136] W.H. Zurek. Cosmological experiments in condensed matter systems. *Physics Reports*, 276(4):177 – 221, 1996.
- [137] Isaac Chuang, Ruth Durrer, Neil Turok, and Bernard Yurke. Cosmology in the laboratory: Defect dynamics in liquid crystals. *Science*, 251(4999):1336–1342, 1991.
- [138] A. Maniv, E. Polturak, and G. Koren. Observation of magnetic flux generated spontaneously during a rapid quench of superconducting films. *Phys. Rev. Lett.*, 91:197001, Nov 2003.
- [139] Nir Navon, Alexander L. Gaunt, Robert P. Smith, and Zoran Hadzibabic. Critical dynamics of spontaneous symmetry breaking in a homogeneous bose gas. *Science*, 347(6218):167–170, 2015.
- [140] David Chen, Matthew White, Cecilia Borries, and Brian DeMarco. Quantum quench of an atomic mott insulator. *Phys. Rev. Lett.*, 106:235304, Jun 2011.

- [141] Ryan Olf, Fang Fang, G. Edward Marti, Andrew MacRae, and Dan M. Stamper-Kurn. Thermometry and cooling of a bose gas to 0.02 times the condensation temperature. *Nature Physics*, 11(9):720–723, Sep 2015.
- [142] Bing Yang, Hui Sun, Chun-Jiong Huang, Han-Yi Wang, Youjin Deng, Han-Ning Dai, Zhen-Sheng Yuan, and Jian-Wei Pan. Cooling and entangling ultracold atoms in optical lattices. *Science*, 2020.
- [143] Michael P. Zaletel, Dan M. Stamper-Kurn, and Norman Y. Yao. Preparation of low entropy correlated many-body states via conformal cooling quenches, 2016.
- [144] J. Mur-Petit, M. Guilleumas, A. Polls, A. Sanpera, M. Lewenstein, K. Bongs, and K. Sengstock. Dynamics of $f = 1$ ^{87}Rb condensates at finite temperatures. *Phys. Rev. A*, 73:013629, Jan 2006.
- [145] Yuki Endo and Tetsuro Nikuni. Kinetic theory of a spin-1 bose condensed gas at finite temperatures. *Journal of Low Temperature Physics*, 163(3):92–121, May 2011.
- [146] Mehrtash Babadi, Eugene Demler, and Michael Knap. Far-from-equilibrium field theory of many-body quantum spin systems: Prethermalization and relaxation of spin spiral states in three dimensions. *Phys. Rev. X*, 5:041005, Oct 2015.
- [147] Toshiya Kinoshita, Trevor Wenger, and David S. Weiss. A quantum newton’s cradle. *Nature*, 440(7086):900–903, Apr 2006.
- [148] Marcos Rigol, Vanja Dunjko, Vladimir Yurovsky, and Maxim Olshanii. Relaxation in a completely integrable many-body quantum system: An ab initio study of the dynamics of the highly excited states of 1d lattice hard-core bosons. *Phys. Rev. Lett.*, 98:050405, Feb 2007.
- [149] Michael Schreiber, Sean S. Hodgman, Pranjal Bordia, Henrik P. Lüschen, Mark H. Fischer, Ronen Vosk, Ehud Altman, Ulrich Schneider, and Immanuel Bloch. Observation of many-body localization of interacting fermions in a quasirandom optical lattice. *Science*, 349(6250):842–845, 2015.
- [150] P. Soltan-Panahi, J. Struck, P. Hauke, A. Bick, W. Plenkers, G. Meineke, C. Becker,

- P. Windpassinger, M. Lewenstein, and K. Sengstock. Multi-component quantum gases in spin-dependent hexagonal lattices. *Nat Phys*, 7(5):434–440, May 2011.
- [151] M. Pasienski, D. McKay, M. White, and B. DeMarco. A disordered insulator in an optical lattice. *Nature Physics*, 6(9):677–680, Sep 2010.
- [152] T. Barthel, C. Kasztelan, I. P. McCulloch, and U. Schollwöck. Magnetism, coherent many-particle dynamics, and relaxation with ultracold bosons in optical superlattices. *Phys. Rev. A*, 79:053627, May 2009.
- [153] Arya Dhar, Manpreet Singh, Ramesh V. Pai, and B. P. Das. Mean-field analysis of quantum phase transitions in a periodic optical superlattice. *Phys. Rev. A*, 84:033631, Sep 2011.
- [154] Andreas Wagner, Andreas Nunnenkamp, and Christoph Bruder. Mean-field analysis of spinor bosons in optical superlattices. *Phys. Rev. A*, 86:023624, Aug 2012.
- [155] A. M. Rey, V. Gritsev, I. Bloch, E. Demler, and M. D. Lukin. Preparation and detection of magnetic quantum phases in optical superlattices. *Phys. Rev. Lett.*, 99:140601, Oct 2007.
- [156] Andreas Wagner, Christoph Bruder, and Eugene Demler. Spin-1 atoms in optical superlattices: Single-atom tunneling and entanglement. *Phys. Rev. A*, 84:063636, Dec 2011.
- [157] S. Fölling, S. Trotzky, P. Cheinet, M. Feld, R. Saers, A. Widera, T. Müller, and I. Bloch. Direct observation of second-order atom tunnelling. *Nature*, 448(7157):1029–1032, Aug 2007.
- [158] Marco Anderlini, Patricia J. Lee, Benjamin L. Brown, Jennifer Sebby-Strabley, William D. Phillips, and J. V. Porto. Controlled exchange interaction between pairs of neutral atoms in an optical lattice. *Nature*, 448(7152):452–456, Jul 2007.
- [159] Kim G. L. Pedersen, Brian M. Andersen, Georg M. Bruun, and Anders S. Sørensen. Using superlattice potentials to probe long-range magnetic correlations in optical lattices. *Phys. Rev. A*, 92:063633, Dec 2015.

- [160] Yu-Ao Chen, Sylvain Nascimbène, Monika Aidelsburger, Marcos Atala, Stefan Trotzky, and Immanuel Bloch. Controlling correlated tunneling and superexchange interactions with ac-driven optical lattices. *Phys. Rev. Lett.*, 107:210405, Nov 2011.
- [161] Stefan Trotzky, Yu-Ao Chen, Ute Schnorrberger, Patrick Cheinet, and Immanuel Bloch. Controlling and detecting spin correlations of ultracold atoms in optical lattices. *Phys. Rev. Lett.*, 105:265303, Dec 2010.
- [162] Junru Li, Wujie Huang, Boris Shteynas, Sean Burchesky, Furkan Çağrı Top, Edward Su, Jeongwon Lee, Alan O. Jamison, and Wolfgang Ketterle. Spin-orbit coupling and spin textures in optical superlattices. *Phys. Rev. Lett.*, 117:185301, Oct 2016.
- [163] Wujie Huang. *Spin-orbit coupling in optical superlattices*. PhD thesis, Massachusetts Institute of Technology., 2016.
- [164] Han-Ning Dai, Bing Yang, Andreas Reingruber, Xiao-Fan Xu, Xiao Jiang, Yu-Ao Chen, Zhen-Sheng Yuan, and Jian-Wei Pan. Generation and detection of atomic spin entanglement in optical lattices. *Nature Physics*, 12(8):783–787, Aug 2016.
- [165] Nakahara Mikio and Ohmi Tetsuo. *Quantum Computing: From Linear Algebra to Physical Realizations*. CRC Press; 1 edition, 2008.
- [166] Bing Yang, Han-Ning Dai, Hui Sun, Andreas Reingruber, Zhen-Sheng Yuan, and Jian-Wei Pan. Spin-dependent optical superlattice. *Phys. Rev. A*, 96:011602, Jul 2017.
- [167] S. Trotzky, P. Cheinet, S. Fölling, M. Feld, U. Schnorrberger, A. M. Rey, A. Polkovnikov, E. A. Demler, M. D. Lukin, and I. Bloch. Time-resolved observation and control of superexchange interactions with ultracold atoms in optical lattices. *Science*, 319(5861):295–299, 2008.
- [168] Hans J. Briegel and Robert Raussendorf. Persistent entanglement in arrays of interacting particles. *Phys. Rev. Lett.*, 86:910–913, Jan 2001.
- [169] Robert Raussendorf and Hans J. Briegel. A one-way quantum computer. *Phys. Rev. Lett.*, 86:5188–5191, May 2001.

- [170] Robert Raussendorf and Hans Briegel. Computational model underlying the one-way quantum computer. *arXiv preprint quant-ph/0108067*, 2001.
- [171] Colin D. Bruzewicz, John Chiaverini, Robert McConnell, and Jeremy M. Sage. Trapped-ion quantum computing: Progress and challenges. *Applied Physics Reviews*, 6(2):021314, 2019.
- [172] Jonathan Jones. Quantum computing with nmr. *Progress in nuclear magnetic resonance spectroscopy*, 59:91–120, 08 2011.
- [173] R. Barends, J. Kelly, A. Megrant, A. Veitia, D. Sank, E. Jeffrey, T. C. White, J. Mutus, A. G. Fowler, B. Campbell, Y. Chen, Z. Chen, B. Chiaro, A. Dunsworth, C. Neill, P. O’Malley, P. Roushan, A. Vainsencher, J. Wenner, A. N. Korotkov, A. N. Cleland, and John M. Martinis. Superconducting quantum circuits at the surface code threshold for fault tolerance. *Nature*, 508(7497):500–503, Apr 2014.
- [174] Quantum computation roadmap, 2004.
- [175] T. D. Ladd, F. Jelezko, R. Laflamme, Y. Nakamura, C. Monroe, and J. L. O’Brien. Quantum computers. *Nature*, 464(7285):45–53, Mar 2010.
- [176] David P. DiVincenzo. Two-bit gates are universal for quantum computation. *Phys. Rev. A*, 51:1015–1022, Feb 1995.
- [177] Adriano Barenco, Charles H. Bennett, Richard Cleve, David P. DiVincenzo, Norman Margolus, Peter Shor, Tycho Sleator, John A. Smolin, and Harald Weinfurter. Elementary gates for quantum computation. *Phys. Rev. A*, 52:3457–3467, Nov 1995.
- [178] Maarten Van den Nest, Akimasa Miyake, Wolfgang Dür, and Hans J. Briegel. Universal resources for measurement-based quantum computation. *Phys. Rev. Lett.*, 97:150504, Oct 2006.
- [179] D. Gross and J. Eisert. Novel schemes for measurement-based quantum computation. *Phys. Rev. Lett.*, 98:220503, May 2007.

- [180] M Van den Nest, W Dür, A Miyake, and HJ Briegel. Fundamentals of universality in one-way quantum computation. *New Journal of Physics*, 9(6):204, 2007.
- [181] D. Gross, J. Eisert, N. Schuch, and D. Perez-Garcia. Measurement-based quantum computation beyond the one-way model. *Phys. Rev. A*, 76:052315, Nov 2007.
- [182] Olaf Mandel, Markus Greiner, Artur Widera, Tim Rom, Theodor W. Hänsch, and Immanuel Bloch. Controlled collisions for multi-particle entanglement of optically trapped atoms. *Nature*, 425(6961):937–940, Oct 2003.
- [183] Daniel Loss and David P. DiVincenzo. Quantum computation with quantum dots. *Phys. Rev. A*, 57:120–126, Jan 1998.
- [184] J. C. Bergquist, Randall G. Hulet, Wayne M. Itano, and D. J. Wineland. Observation of quantum jumps in a single atom. *Phys. Rev. Lett.*, 57:1699–1702, Oct 1986.
- [185] Nir Davidson, Heun Jin Lee, Charles S. Adams, Mark Kasevich, and Steven Chu. Long atomic coherence times in an optical dipole trap. *Phys. Rev. Lett.*, 74:1311–1314, Feb 1995.
- [186] S. Aigner, L. Della Pietra, Y. Japha, O. Entin-Wohlman, T. David, R. Salem, R. Folman, and J. Schmiedmayer. Long-range order in electronic transport through disordered metal films. *Science*, 319(5867):1226–1229, 2008.
- [187] Amila Ariyaratne, Dolev Bluvstein, Bryan A. Myers, and Ania C. Bleszynski Jayich. Nanoscale electrical conductivity imaging using a nitrogen-vacancy center in diamond. *Nature Communications*, 9(1):2406, Jun 2018.
- [188] R. L. Fagaly. Superconducting quantum interference device instruments and applications. *Review of Scientific Instruments*, 77(10):101101, 2006.
- [189] Elena Boto, Sofie S Meyer, Vishal Shah, Orang Alem, Svenja Knappe, Peter Kruger, T Mark Fromhold, Mark Lim, Paul M Glover, Peter G Morris, et al. A new generation of magnetoencephalography: Room temperature measurements using optically-pumped magnetometers. *NeuroImage*, 149:404–414, 2017.

- [190] Mario H. Acua. Space-based magnetometers. *Review of Scientific Instruments*, 73(11):3717–3736, 2002.
- [191] C. S. Arridge, J. P. Eastwood, C. M. Jackman, G.-K. Poh, J. A. Slavin, M. F. Thomson, N. André, X. Jia, A. Kidder, L. Lamy, A. Radioti, D. B. Reisenfeld, N. Sergis, M. Volwerk, A. P. Walsh, P. Zarka, A. J. Coates, and M. K. Dougherty. Cassini in situ observations of long-duration magnetic reconnection in saturn’s magnetotail. *Nature Physics*, 12(3):268–271, Mar 2016.
- [192] Morgan W. Mitchell and Silvana Palacios Alvarez. Colloquium: Quantum limits to the energy resolution of magnetic field sensors. *Rev. Mod. Phys.*, 92:021001, Apr 2020.
- [193] M. Vengalattore, J. M. Higbie, S. R. Leslie, J. Guzman, L. E. Sadler, and D. M. Stamper-Kurn. High-resolution magnetometry with a spinor bose-einstein condensate. *Phys. Rev. Lett.*, 98:200801, May 2007.
- [194] A. and M. Haji-Sheikh Grosz and S. Mukhopadhyay. *High Sensitivity Magnetometers*. Springer, New York, 2016.
- [195] C. L. Degen, F. Reinhard, and P. Cappellaro. Quantum sensing. *Rev. Mod. Phys.*, 89:035002, Jul 2017.
- [196] S. R. Leslie, J. Guzman, M. Vengalattore, Jay D. Sau, Marvin L. Cohen, and D. M. Stamper-Kurn. Amplification of fluctuations in a spinor bose-einstein condensate. *Phys. Rev. A*, 79:043631, Apr 2009.
- [197] Jay D Sau, Sabrina R Leslie, Marvin L Cohen, and Dan M Stamper-Kurn. Spin squeezing of high-spin, spatially extended quantum fields. *New Journal of Physics*, 12(8):085011, 2010.

APPENDICES


APPENDIX A

QUANTUM QUENCH AND NONEQUILIBRIUM DYNAMICS IN LATTICE-CONFINED SPINOR CONDENSATES

This appendix includes a reprint of Ref. [67]: Z. Chen, T. Tang, J. Austin, Z. Shaw, L. Zhao, and Y. Liu. Quantum quench and nonequilibrium dynamics in lattice-confined spinor condensates. *Phys. Rev. Lett.*, 123:113002, Sep 2019.

Quantum Quench and Nonequilibrium Dynamics in Lattice-Confined Spinor Condensates

Z. Chen¹, T. Tang, J. Austin, Z. Shaw, L. Zhao, and Y. Liu^{*}
Department of Physics, Oklahoma State University, Stillwater, Oklahoma 74078, USA

 (Received 20 May 2019; published 10 September 2019)

We present an experimental study on nonequilibrium dynamics of a spinor condensate after it is quenched across a superfluid to Mott insulator (MI) phase transition in cubic lattices. Intricate dynamics consisting of spin-mixing oscillations at multiple frequencies are observed in time evolutions of the spinor condensate localized in deep lattices after the quantum quench. Similar spin dynamics also appear after spinor gases in the MI phase are suddenly moved away from their ground states via quenching magnetic fields. We confirm these observed spectra of spin-mixing dynamics can be utilized to reveal atom number distributions of an inhomogeneous system, and to study transitions from two-body to many-body dynamics. Our data also imply the nonequilibrium dynamics depend weakly on the quench speed but strongly on the lattice potential. This enables precise measurements of the spin-dependent interaction, a key parameter determining the spinor physics.

DOI: [10.1103/PhysRevLett.123.113002](https://doi.org/10.1103/PhysRevLett.123.113002)

Spinor Bose-Einstein condensates (BECs) are multi-component condensates possessing a spin degree of freedom [1]. Combined with optical lattices and microwave dressing fields, spinor gases offer an unprecedented degree of control over many parameters and have thus been considered as ideal candidates for studying nonequilibrium dynamics [1–12]. Such a system can be easily prepared far away from equilibrium through quenching one of its highly controllable parameters, e.g., the number of atoms, temperature, total spin of the system, the lattice potential, or the dimensionality of the system [1–10]. Interesting dynamics have also been initiated in lattice-confined spinor gases by nonequilibrium initial states, such as interaction-driven revival dynamics in one-dimensional Ising spin chains [13], dynamics and equilibration of spinor BECs in two-dimensional lattices [3], and spin-mixing dynamics of tightly confined atom pairs in cubic lattices [14,15]. Another notable advantage of spinor systems on investigating nonequilibrium dynamics is their long equilibration time, ranging from tens of milliseconds to several seconds [1,3]. Experimental studies on nonequilibrium dynamics have been conducted in spinor gases extensively at two extremes, i.e., in a clean two-body system with a pair of atoms in the Mott-insulator (MI) phase [14,15], and in a many-body system with more than 10^4 atoms in the superfluid (SF) phase [1–4]. Transitions between these two extremes, however, remain less explored [5].

In this Letter, we experimentally confirm that lattice-trapped spinor BECs provide a perfect platform to understand these less-explored transitions. Our experiments are performed in a quantum quench scenario starting with an antiferromagnetic spinor BEC at its SF ground state, based

on a theoretical proposal in Ref. [5]. We continuously quench the potential of a cubic lattice to a very large value, completely suppressing tunnelings to freeze atom number distributions in individual lattice sites. Spin dynamics are observed at fast quench speeds, and adiabatic SF-MI quantum phase transitions are detected after sufficiently slow lattice ramps. About half of the data shown in this Letter are collected after the lattice is quenched at an intermediate speed, which is slow enough to prevent excitations to higher vibrational bands while remaining fast enough to suppress hopping among lattice sites. We observe dynamics consisting of spin-mixing oscillations at multiple frequencies in spinor BECs after the quantum quench in magnetic fields of strength $B < 60 \mu\text{T}$. The remaining data are taken after adiabatic lattice ramps. Similar spin dynamics also occur after we abruptly move spinor gases in the MI phase away from their ground states via quenching magnetic fields. In our system, an inhomogeneous system with an adjustable peak occupation number per lattice site (n_{peak}), a significant amount of lattice sites are occupied by more than two atoms. The observed spin-mixing spectra are thus utilized to study transitions between two-body and many-body spin dynamics and to reveal atom number distributions of an inhomogeneous system. Our data also indicate the nonequilibrium dynamics depend weakly on the quench speed but strongly on the lattice potential. We find every observed spin dynamics is well described by a sum of multiple Rabi-type spin-mixing oscillations. This enables us to precisely measure the ratio of the spin-independent interaction U_0 to the spin-dependent interaction U_2 , an important factor determining the spinor physics.

The site-independent Bose-Hubbard model has successfully described lattice-confined spinor BECs [5,16,17]. We can understand our data taken in deep lattices with a simplified Bose-Hubbard model by ignoring the tunneling energy J as follows [5,17]:

$$H = \frac{U_0}{2}n(n-1) + \frac{U_2}{2}(\vec{S}^2 - 2n) + q(n_+ + n_-) - \mu n. \quad (1)$$

Here, q is the net quadratic Zeeman energy induced by magnetic and microwave fields, μ is the chemical potential, $n = \sum_{m_F} n_{m_F}$ is the total atom number in each lattice site with n_{m_F} atoms staying in the hyperfine m_F state, and \vec{S} is the spin operator [5,17].

We start each experimental cycle at $q/h = 40$ Hz in free space with a spin-1 antiferromagnetic spinor BEC of up to 10^5 sodium atoms in its ground state, the longitudinal polar (LP) state with $\rho_0 = 1$ and $m = 0$ [18]. Here ρ_{m_F} is the fractional population of the m_F state, $m = \rho_{+1} - \rho_{-1}$ is the magnetization, and h is the Planck constant. Two different quench sequences, Quench- L and Quench- Q , are applied in this Letter [18]. In the Quench- L sequences, we tune magnetic fields to a desired q and then quench up the depth u_L of a cubic lattice from 0 to $28(2)E_R$ within a time duration t_{ramp} , where E_R is the recoil energy [18]. This final depth u_L is much larger than SF-MI transition points and thus deep enough to localize atoms into individual lattice sites. In the Quench- Q sequences, we adiabatically ramp up cubic lattices to a final depth of $u_L \geq 28E_R$ in a high field (where $q \gg U_2$), which ensures atoms cross SF-MI transitions and enter into their ground states (where $\rho_0 \simeq 1$) in the MI phase [16], and we then suddenly quench magnetic fields to a desired q for initiating nonequilibrium dynamics. After each quench sequence, we hold atoms in lattices for a certain time t_{hold} , then measure ρ_0 based on Ref. [18].

Nonequilibrium dynamics consisting of spin-mixing oscillations at multiple frequencies are observed after both Quench- L and Quench- Q sequences in spinor gases localized in deep lattices at $q/h < 100$ Hz. Two typical time evolutions detected after Quench- Q sequences are shown in Fig. 1(a). Such an evolution appears to be fit by a composition of multiple Rabi-type oscillations [see solid lines in Fig. 1(a) and Eq. (2)]. This can be explained by considering that n atoms tightly confined in one lattice site display a Rabi-type oscillation at a fixed frequency f_n , and the observed dynamics combine all time evolutions occurring in individual lattice sites for our inhomogeneous system. We derive $f_n = E_n/h$ from Eq. (1), where E_n is the energy gap between the ground state and the first excited state in the subspace of $m = 0$ at a given n [see Fig. 1(b)]. Analytical expressions for f_n can be found at $n = 2$ and $n = 3$, i.e., $f_2 = U_2\sqrt{9 - 4(q/U_2) + 4(q/U_2)^2}/h$ and $f_3 = U_2\sqrt{25 + 4(q/U_2) + 4(q/U_2)^2}/h$. We develop the following empirical formula based on the predicted f_n for an inhomogeneous system with a certain n_{peak} , and find all

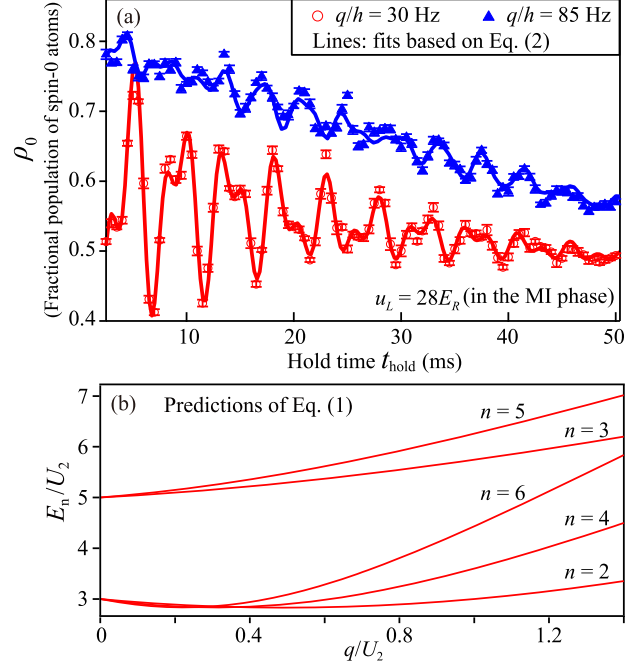


FIG. 1. (a) Observed spin dynamics after Quench- Q sequences to different q . Lines are fits based on Eq. (2) [18]. (b) Lines denote the predicted energy $E_n = hf_n$ (see text).

observed spin dynamics can be fit by this formula [see typical examples in Fig. 1(a) and Ref. [18]],

$$\rho_0(t) = \sum_{n=2}^{n_{\text{peak}}} A_n \exp(-t/\tau_n) \sin[2\pi f_n(t - t_0)] + \Delta\rho_0 \exp(-t/\tau_0) + \frac{1}{3}. \quad (2)$$

Here, the first term combines individual Rabi-type oscillations at all possible n with $1/\tau_n$ being the damp rate for oscillation amplitudes and t_0 marking the beginning of oscillations, while the second term describes an overall decay of spin oscillations at a decay rate of $1/\tau_0$. This decay may be mainly due to unavoidable lattice-induced heatings. The third term of Eq. (2) indicates the three spin components equally distribute in equilibrium states when $t_{\text{hold}} \rightarrow \infty$ [3,19]. The validity of Eq. (2), a conservative model, may be justified by the fact that observed atom losses are less than 10% within every time evolution studied in this Letter.

To better illustrate the spin-mixing dynamics, we conduct fast Fourier transformations (FFT) onto all observed time evolutions. Two typical FFT spectra extracted from the same dataset over different time durations are shown in Fig. 2(a), where the vertical lines mark the five f_n predicted by Eq. (1). Each of these two FFT spectra has five distinguished peaks agreeing well with the predictions of Eq. (1); i.e., all spin components in the three even Mott lobes oscillate at lower frequencies while particles in the two odd Mott lobes display higher spin oscillation

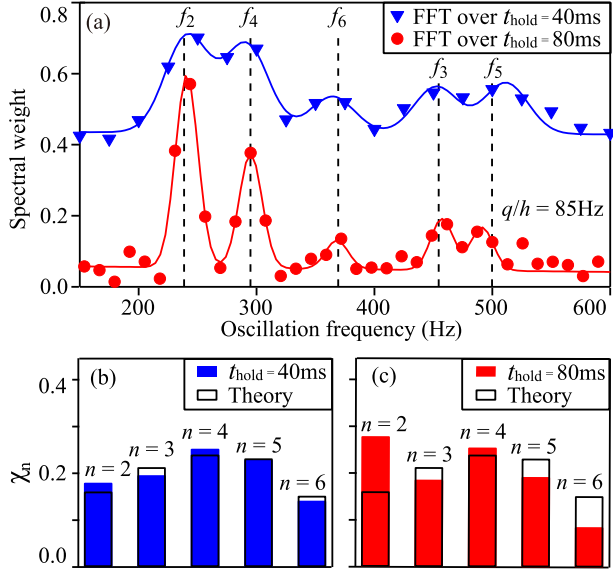


FIG. 2. (a) Triangles (circles) represent fast Fourier transformations (FFT) over the first 40 ms (80 ms) of t_{hold} on the $q/h = 85$ Hz dataset shown in Fig. 1(a). Vertical lines mark the predicted f_n (see text). Solid lines are five-Gaussian fits. Results obtained at $t_{\text{hold}} = 40$ ms are shifted up by 0.4 for visual clarity. (b) Atom number distributions extracted from the $t_{\text{hold}} = 40$ ms FFT spectrum in panel (a). We define χ_n as the fraction of atoms localized in lattice sites having n atoms, and extract χ_n from dividing the area below the corresponding peak in a FFT spectrum by the spin oscillation amplitude D_n (see Ref. [20]). Black bars mark the predicted χ_n in Mott-insulator shells at $n_{\text{peak}} = 6$ based on Eq. (1) and the Thomas-Fermi approximation. (c) Similar to panel (b) but extracted from the $t_{\text{hold}} = 80$ ms FFT spectrum in panel (a).

frequencies when $q/U_2 < 1.55$. Atom number distributions in the spinor gases can also be revealed from the corresponding FFT spectrum over a given time duration, as explained in Figs. 2(b) and 2(c). A comparison between these two figures clearly demonstrates that number distributions χ_n in our system quickly change with time t_{hold} and the $n = 2$ Mott lobe becomes more dominating after atoms are held in deep lattices for a longer time. This

implies atoms in the $n = 2$ Mott lobe decay more slowly, which may be owing to a lack of three-body inelastic collisions in this lobe. Figure 2(b) shows another notable result: each experimental χ_n extracted from the FFT spectrum over a short time duration (i.e., $t_{\text{hold}} = 40$ ms) coincides with the theoretical χ_n derived from Eq. (1) and the Thomas-Fermi approximation for Mott-insulator shells at $n_{\text{peak}} = 6$. Atoms in initial states distribute into these predicted Mott shells during the Quench- Q sequences, because the initial states are the ground states of the MI phase. Our data thus experimentally confirm that the spin-mixing dynamics and their corresponding FFT spectra over a short t_{hold} can efficiently probe the initial Fock-state distributions after a sufficiently fast quench.

Similar nonequilibrium dynamics are also detected in time evolutions of spinor gases after Quench- L sequences under a wide range of magnetic fields (see Fig. 3). To our knowledge, this may be the first experimental observation of such complicated spin-mixing dynamics, although its theoretical model has been studied by Ref. [5]. Our observations indicate the spin-mixing dynamics weakly depend on t_{ramp} [21]. Typical examples can be seen in Fig. 3(a), where the data sets collected at distinct t_{ramp} display similar dynamics with almost identical oscillation frequencies and slightly different oscillation amplitudes. This may be due to the fact that t_{ramp} in a Quench- L sequence is carefully chosen for limiting all spin components to oscillate between the ground states and the first excited states.

The spin oscillations observed after Quench- L sequences can also be well fit by Eq. (2) [see Fig. 3(a)]. We can extract the spin-dependent interaction U_2 from these fitting curves, because U_2 decides frequency f_n when $n \geq 2$ at a fixed q . Figures 3(b) and 3(c) show 20 experimental values of U_2 extracted from our data taken under very different conditions. By applying linear fits to these data points, we find a precise value for two key parameters that determine the spinor physics, i.e., $U_2/U_0 \simeq 0.035(3)$ and $a_2/a_0 \simeq 1.115(10)$ for ^{23}Na atoms. Here a_2 and a_0 are s -wave scattering lengths, and $a_2/a_0 = (U_2 + U_0)/(U_0 - 2U_2)$ based on Refs. [25,26]. Many published values of

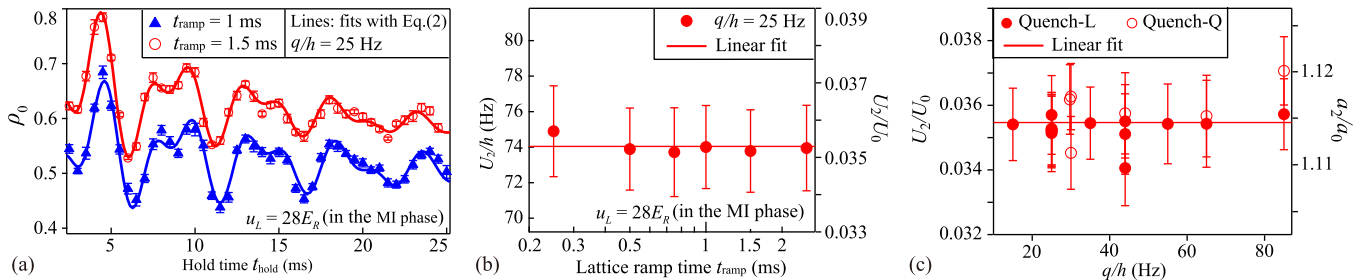


FIG. 3. (a) Observed spin dynamics after Quench- L sequences at two t_{ramp} . Lines are fits based on Eq. (2). Data taken at $t_{\text{ramp}} = 1.5$ ms are shifted up by 0.1 for visual clarity. (b) Extracted U_2 and U_2/U_0 from fitting observed dynamics with Eq. (2) at various t_{ramp} [23]. The horizontal line is a linear fit. (c) Similar to panel (b) but based on our data taken under 20 different conditions. The right axis marks the corresponding ratio $a_2/a_0 = (U_2 + U_0)/(U_0 - 2U_2)$, where a_0 and a_2 are scattering lengths.

U_2/U_0 were derived from the scattering lengths [5,27–33]. For example, Refs. [27,28], respectively, found scattering lengths that would lead to $U_2/U_0 = 0.032(14)$ and $0.035(11)$. In addition, measuring the scattering lengths through Feshbach spectroscopy could yield $U_2/U_0 = 0.037(6)$ [29] and $0.036(3)$ [30]. Therefore, the observed spin dynamics can conveniently measure spin-dependent interactions and U_2/U_0 with a good resolution.

We also notice one puzzling difference between the nonequilibrium dynamics initiated by Quench- L and Quench- Q sequences: atoms appear to oscillate with a larger amplitude despite having the same frequencies after the Quench- Q sequence, even if spinor gases are prepared into the same final u_L and q by these two quench sequences. This amplitude difference may be attributed to the inevitable dephasing and energy dissipations induced by a number of tunneling processes. Note that atoms are fully localized in individual lattice sites with negligible tunnelings during Quench- Q sequences. In contrast, spinor gases cross SF-MI phase transitions during a Quench- L sequence, tunnelings among adjacent sites thus cannot be ignored during a certain part of this sequence. Other possible reasons for the different oscillation amplitudes may include significant heatings induced by first-order SF-MI phase transitions at a small q during Quench- L sequences [16], different atom number distributions introduced by the quench sequences [34], and nonadiabatic lattice ramps in Quench- L sequences.

To understand how tunnelings affect the spin-mixing dynamics, we monitor spin oscillations after varying the tunneling energy J in a well-controlled way [8]. We first prepare a nonequilibrium initial state with a Quench- Q sequence to $q/h = 30$ Hz in a very deep cubic lattice of $u_{L,x} = u_{L,y} = u_{L,z} = 33(3)E_R$ with $J \simeq 0$, and then suddenly increase J to a desired value by properly reducing only one lattice depth $u_{L,z}$. Here $u_{L,x}$, $u_{L,y}$, and $u_{L,z}$ are depths of the three lattice beams along orthogonal directions, respectively. Results shown in Fig. 4 are collected at four signature $u_{L,z}$, gradually spanning from the few-body dynamics for spinor gases tightly localized in deep lattices at $u_{L,z} = 33E_R$ with $J \simeq 0$, to the many-body dynamics for atoms loosely confined in shallow lattices with $J \gg 0$ at $u_{L,z} = 12E_R$. Amplitudes of spin-mixing oscillations appear to quickly decrease as $u_{L,z}$ is reduced, and completely vanish when $u_{L,z} < 14E_R$. We may understand these observations from two simple illustrations. In one scenario, two atoms oscillate at the frequency f_2 in an $n=2$ lattice site. The spin oscillation disappears as one of the two atoms tunnels out of the site. In another scenario, $n > 2$ atoms oscillate in a lattice site at frequency f_n . After one atom hopping out of this site, spin oscillations occurring in this site and the adjacent site that accepts the atom should be changed. The occurrence of many of such tunneling events could significantly reduce oscillation amplitudes of the observed spin-mixing dynamics. As J increases with the reduction of $u_{L,z}$, the damping is enhanced and

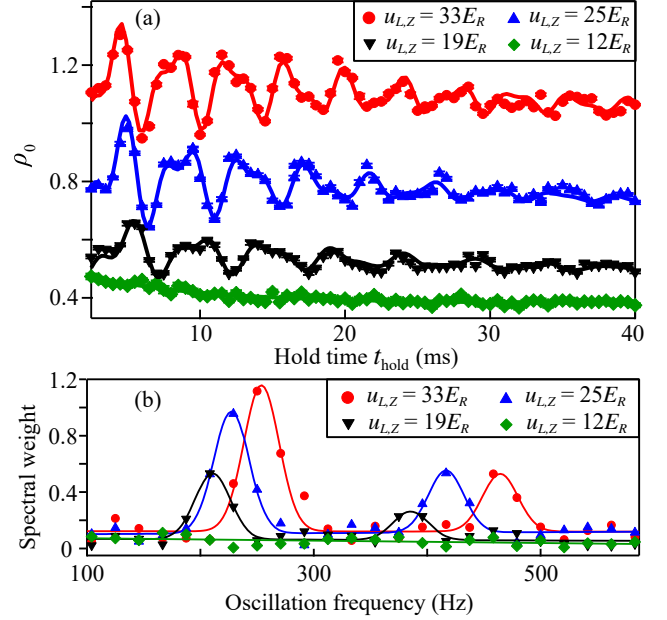


FIG. 4. (a) Observed spin dynamics after Quench- Q sequences to $q/h = 30$ Hz at various $u_{L,z}$ while $u_{L,x} = u_{L,y} = 33(3)E_R$ (see text). Results obtained at $u_{L,z} = 33(3)E_R$, $25(2)E_R$, and $19(2)E_R$ are, respectively, shifted up by 0.55, 0.25, and 0.06 for visual clarity. Lines are fits based on Eq. (2). (b) FFT spectra of the dynamics shown in panel (a). Lines are two-Gaussian fits.

eventually stops the spin oscillations. As a numerical example, the predicted damp time constant due to tunnelings is 11 ms at $u_{L,z} = 19E_R$ [8], which is comparable to the experimental τ_n of around 15 ms extracted from Fig. 4(a). These results justify our use of deep lattices and subsequent neglecting of J in Eq. (1). The underlying physics of the damped spin dynamics and its connection with the Schwinger boson model [35,36] are worthy of further investigation.

Figure 4(b) show the FFT spectra extracted from the nonequilibrium dynamics observed at the four $u_{L,z}$. Each of these FFT spectra has only two distinguished peaks rather than the predicted five peaks; i.e., the wide peaks at around 250 Hz correspond to the oscillations of even n atoms and the wide peaks at around 450 Hz to the oscillations of odd n atoms. One possible reason for this discrepancy is t_{hold} needs to be much longer (greater than 160 ms for all even n) to reduce the aliasing effect of the spectrum analysis, but t_{hold} in our system is limited by lattice heatings and atom losses. The FFT spectra in Fig. 4(b), however, clearly show that a larger $u_{L,z}$ leads to spin oscillations of higher frequencies. This can be interpreted by the fact that frequency f_n is determined by U_2 and thus also by the effective lattice depth $u_L = \sqrt[3]{u_{L,x}u_{L,y}u_{L,z}}$. Our calculations confirm that the effective U_2 gives oscillation frequencies that fall into those broad peaks seen in Fig. 4(b).

In conclusion, we have presented the first experimental study on few-body spin dynamics and transitions between the well-studied two-body and many-body dynamics in

antiferromagnetic spinor BECs. Dynamics consisting of spin-mixing oscillations at multiple frequencies, as opposed to the singular frequency seen in a BEC of thousands of atoms in the superfluid phase, have been observed in time evolutions of the spinor condensate localized in deep lattices after two quench sequences. Unlike the many-body spin dynamics, especially those interpreted by the single mode approximation in Refs. [1–3], the spin-mixing oscillations presented in this Letter indicate quantum recurrences induced by discrete energy spectra [5]. We have confirmed our observed spin-mixing dynamics can reveal atom number distributions of an inhomogeneous system and also enable precise measurements of two key parameters. The lattice quench method is applicable to other spinor systems.

We thank Eite Tiesinga for insightful discussions. We also thank the National Science Foundation, the Noble Foundation, and the Oklahoma Center for the Advancement of Science and Technology for financial support.

*yingmei.liu@okstate.edu

- [1] D. M. Stamper-Kurn and M. Ueda, *Rev. Mod. Phys.* **85**, 1191 (2013).
- [2] L. Zhao, J. Jiang, T. Tang, M. Webb, and Y. Liu, *Phys. Rev. A* **89**, 023608 (2014).
- [3] L. Zhao, J. Jiang, T. Tang, M. Webb, and Y. Liu, *Phys. Rev. Lett.* **114**, 225302 (2015).
- [4] C. Becker, P. Soltan-Panahi, J. Kronjäger, S. Dörscher, K. Bongs, and K. Sengstock, *New J. Phys.* **12**, 065025 (2010).
- [5] K. W. Mahmud and E. Tiesinga, *Phys. Rev. A* **88**, 023602 (2013).
- [6] C. B. Dağ, S.-T. Wang, and L.-M. Duan, *Phys. Rev. A* **97**, 023603 (2018).
- [7] M. Lewenstein, A. Sanpera, V. Ahufinger, B. Damski, A. Sen(De), and U. Sen, *Adv. Phys.* **56**, 243 (2007).
- [8] J. S. Krauser, J. Heinze, N. Fläschner, S. Götze, O. Jürgensen, D.-S. Lühmann, C. Becker, and K. Sengstock, *Nat. Phys.* **8**, 813 (2012).
- [9] A. de Paz, A. Sharma, A. Chotia, E. Maréchal, J. H. Huckans, P. Pedri, L. Santos, O. Gorceix, L. Vernac, and B. Laburthe-Tolra, *Phys. Rev. Lett.* **111**, 185305 (2013).
- [10] J. Jiang, L. Zhao, M. Webb, and Y. Liu, *Phys. Rev. A* **90**, 023610 (2014).
- [11] J. Simon, W. S. Bakr, R. Ma, M. E. Tai, P. M. Preiss, and M. Greiner, *Nature (London)* **472**, 307 (2011).
- [12] P. Soltan-Panahi, J. Struck, P. Hauke, A. Bick, W. Plenkers, G. Meineke, C. Becker, P. Windpassinger, M. Lewenstein, and K. Sengstock, *Nat. Phys.* **7**, 434 (2011).
- [13] J. Zeiher, J.-Y. Choi, A. Rubio-Abadal, T. Pohl, R. van Bijnen, I. Bloch, and C. Gross, *Phys. Rev. X* **7**, 041063 (2017).
- [14] A. Widera, F. Gerbier, S. Fölling, T. Gericke, O. Mandel, and I. Bloch, *Phys. Rev. Lett.* **95**, 190405 (2005).
- [15] A. Widera, F. Gerbier, S. Fölling, T. Gericke, O. Mandel, and I. Bloch, *New J. Phys.* **8**, 152 (2006).
- [16] J. Jiang, L. Zhao, S.-T. Wang, Z. Chen, T. Tang, L.-M. Duan, and Y. Liu, *Phys. Rev. A* **93**, 063607 (2016), and the references therein.
- [17] L. Zhao, T. Tang, Z. Chen, and Y. Liu, [arXiv:1801.00773](https://arxiv.org/abs/1801.00773).
- [18] See Supplemental Material at <http://link.aps.org/supplemental/10.1103/PhysRevLett.123.113002> for additional details of our experimental procedures and analysis methods.
- [19] N. T. Phuc, Y. Kawaguchi, and M. Ueda, *Phys. Rev. A* **84**, 043645 (2011).
- [20] Our calculations based on Eq. (1) indicate spin oscillation amplitudes D_n for an inhomogeneous system with $n_{\text{peak}} = 6$ at $q/h = 85$ Hz are $D_1 = 0$, $D_2 = 0.413$, $D_3 = 0.229$, $D_4 = 0.269$, $D_5 = 0.215$, and $D_6 = 0.199$. Because no spin oscillations occur when $n = 1$, χ_n shown in Fig. 2 reflect the normalized number distributions after the $n = 1$ Mott lobe is excluded.
- [21] When $t_{\text{ramp}} < 1$ ms, we find atoms in our system need an additional 1 ms to completely lose their phase coherence. A similar phenomenon has also been reported in rubidium systems [22].
- [22] J. Sebby-Strabley, B. L. Brown, M. Anderlini, P. J. Lee, W. D. Phillips, J. V. Porto, and P. R. Johnson, *Phys. Rev. Lett.* **98**, 200405 (2007).
- [23] U_0 is derived from Ref. [24].
- [24] D. Jaksch, C. Bruder, J. I. Cirac, C. W. Gardiner, and P. Zoller, *Phys. Rev. Lett.* **81**, 3108 (1998).
- [25] T. L. Ho, *Phys. Rev. Lett.* **81**, 742 (1998).
- [26] T. Ohmi and K. Machida, *J. Phys. Soc. Jpn.* **67**, 1822 (1998).
- [27] A. Crubellier, O. Dulieu, F. Masnou-Seeuws, M. Elbs, H. Knöckel, and E. Tiemann, *Eur. Phys. J. D* **6**, 211 (1999).
- [28] F. A. van Abeelen and B. J. Verhaar, *Phys. Rev. A* **59**, 578 (1999).
- [29] C. Samuelis, E. Tiesinga, T. Laue, M. Elbs, H. Knöckel, and E. Tiemann, *Phys. Rev. A* **63**, 012710 (2000).
- [30] S. Knoop, T. Schuster, R. Scelle, A. Trautmann, J. Appmeier, M. K. Oberthaler, E. Tiesinga, and E. Tiemann, *Phys. Rev. A* **83**, 042704 (2011).
- [31] K. Fujimoto and M. Tsubota, *Phys. Rev. A* **88**, 063628 (2013).
- [32] J. Lovegrove, M. O. Borgh, and J. Ruostekoski, *Phys. Rev. Lett.* **112**, 075301 (2014).
- [33] S. Yi and H. Pu, *Phys. Rev. Lett.* **97**, 020401 (2006).
- [34] Z. Chen, J. Austin, Z. Shaw, L. Zhao, and Y. Liu (to be published).
- [35] E. Altman and A. Auerbach, *Phys. Rev. Lett.* **89**, 250404 (2002).
- [36] S. M. Davidson and A. Polkovnikov, *Phys. Rev. Lett.* **114**, 045701 (2015).

APPENDIX B

LATTICE-INDUCED RAPID FORMATION OF SPIN SINGLETs IN SPIN-1 SPINOR CONDENSATES

This appendix includes a reprint of Ref. [36]: L. Zhao, T. Tang, Z. Chen, and Y. Liu, Lattice-induced rapid formation of spin singlets in spin-1 spinor condensates, arXiv: 1801.00773.

Lattice-induced rapid formation of spin singlets in spin-1 spinor condensates

L. Zhao, T. Tang, Z. Chen, and Y. Liu*

Department of Physics, Oklahoma State University, Stillwater, Oklahoma 74078, USA

(Dated: January 3, 2018)

We experimentally demonstrate that combining a cubic optical lattice with a spinor Bose-Einstein condensate substantially relaxes three strict constraints and brings spin singlets of ultracold spin-1 atoms into experimentally accessible regions. About 80 percent of atoms in the lattice-confined spin-1 spinor condensate are found to form spin singlets, immediately after the atoms cross first-order superfluid to Mott-insulator phase transitions in a microwave dressing field. A phenomenological model is also introduced to well describe our observations without adjustable parameters.

PACS numbers: 67.85.Fg, 03.75.Kk, 03.75.Mn, 05.30.Rt

Many-body spin singlet states, in which multiple spin components of zero total spin are naturally entangled, have been widely suggested as ideal candidates in investigating quantum metrology and quantum memories [1–14]. Advantages of spin singlets in the quantum information research include long lifetimes and enhanced tolerance to environmental noises [2, 3]. These advantages may become more pronounced if the singlets consist of ultracold spin-1 particles [1]. A spin singlet is the ground state of many types of spinor gases, however, its experimental realizations have proven to be very challenging mainly due to its fragilities [3, 10, 12–15]. Allowed parameter ranges for spin singlets of spin-1 atoms are strictly limited to the vicinity of zero quadratic Zeeman energy q and zero magnetization m , and the ranges drastically shrink when the atom number increases [10–13]. Another constraint is the formation of spin singlets requires atoms remaining adiabatic for a long time duration [13, 16]. In this Letter, we experimentally demonstrate that combining a spinor Bose-Einstein condensate (BEC) with cubic optical lattices significantly relaxes these strict constraints and enables creating spin singlets of spin-1 atoms rapidly. Our observations confirm that spin singlets are brought into experimentally accessible regions by two key lattice-modified parameters, which are the lattice-enhanced interatomic interactions and substantially reduced atom number in individual lattice sites. Lattice-confined spinor BECs present degeneracies in spin and spatial domains, which provide perfect platforms to simulate quantum mesoscopic systems and study rich physics of fragmentation [7, 12].

Different methods have been proposed for detecting spin singlets. The first approach is to measure the population of each spin component, as atoms in a spin singlet should be evenly distributed into all spin states [17, 18]. The second method is to verify a spin singlet is invariant after its spin is rotated by a resonant Rf-pulse [2, 9, 12, 18, 19]. Another signature of a spin singlet is its high level of spin squeezing shown in quantum non-demolition measurements [2, 4–6]. A spin singlet can also be identified by its high-order correlation functions, e.g., its zero spin nematicity detected by light scattering

measurements [12, 20]. Other detectable parameters of a spin singlet include large population fluctuations in each of its spin components, and its excitation spectra mapped by Bragg scattering [10, 17]. In this paper, we apply the first two methods to demonstrate that about 80% of spin-1 atoms in a lattice-confined spinor BEC can form spin singlets, immediately after the atoms cross first-order superfluid (SF) to Mott-insulator (MI) phase transitions in a microwave dressing field. A phenomenological model is also developed to explain our observations without adjustable parameters.

We start each experimental cycle with an antiferromagnetic $F=1$ spinor BEC of $n = 1.2 \times 10^5$ sodium atoms and zero m in its free-space ground state, i.e., a longitudinal polar (LP) state in the $q > 0$ region or a transverse polar (TP) state when $q < 0$ [21–25]. The atoms are then loaded into cubic lattices and enter into the MI phase with the peak occupation number per lattice site being five, $n_{\text{peak}} = 5$. We express the Hamiltonian of the spinor Mott insulators by ignoring the hopping energy in the site-independent Bose-Hubbard model as [21]:

$$\hat{H} = \frac{U_0}{2}(\hat{n}^2 - \hat{n}) - \mu\hat{n} + \frac{U_2}{2}(\hat{S}^2 - 2\hat{n}) + q(\hat{n}_1 + \hat{n}_{-1}). \quad (1)$$

Here U_0 (U_2) is the spin-independent (spin-dependent) interaction, μ is the chemical potential, \hat{S} is the spin operator, and $\hat{n} = \sum_{m_F} \hat{n}_{m_F}$ is the number operator of all hyperfine m_F states. We obtain the ground states of spinor Mott insulators by diagonalizing Eq. (1) at a given n . For example, the ground states are spin singlets at zero q in the even Mott lobes.

Sufficiently deep cubic lattices localize atoms and lower n by five orders of magnitude in a typical BEC system. Figure 1 illustrates how this enormous reduction in n together with the lattice-enhanced interatomic interactions can make spin singlets realizable in experimentally accessible regions. Figure 1 is derived from the mean-field theory (MFT) and based on two notable signatures of a spin singlet, i.e., each of its m_F states has an identical fractional population ρ_{m_F} and a big $\Delta\rho_{m_F}$ (the standard deviation of ρ_{m_F}) [10, 17, 18]. For example,

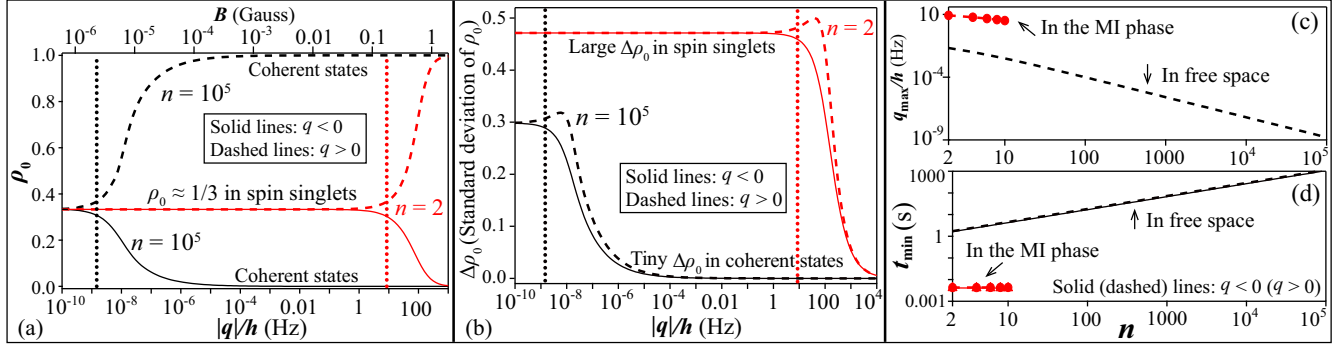


FIG. 1. (a) and (b): vertical black (red) dotted lines mark q_{\max} , the maximum allowed q for spin singlets, in $F=1$ sodium spinor BECs of $n = 10^5$ atoms in free space (in the $n=2$ Mott lobe at $u_L = 26E_R$). All panels are derived from MFT at zero m with solid (dashed) lines representing the $q < 0$ ($q > 0$) region, and black (red) lines representing spinor gases in free space (spinor Mott insulators) [16]. (a) Predicted ρ_0 versus $|q|$ at $n = 2$ (red) and 10^5 (black). The top horizontal axis lists the corresponding B when $q > 0$. (b) Predicted $\Delta\rho_0$ versus $|q|$ at $n = 2$ (red) and 10^5 (black). (c) Predicted q_{\max} versus n . (d) The minimum time t_{\min} versus n for generating singlets of sodium atoms via an adiabatic sweep at its corresponding $\pm q_{\max}$.

spin singlets of $F=1$ atoms should have $\rho_0 \approx \rho_{\pm 1} \approx 1/3$ and $\Delta\rho_0 = 2\Delta\rho_{\pm 1} > 0.29$. In sharp contrast, $\rho_0 = 0$ and $\rho_{\pm 1} = 0.5$ ($\rho_0 = 1$ and $\rho_{\pm 1} = 0$) with negligible $\Delta\rho_{m_F}$ are found in coherent TP (LP) states when $q < 0$ ($q > 0$) [24]. The allowed q range for spin singlets is $0 \leq |q| \leq q_{\max}$, which is determined by considering $\Delta\rho_{m_F} \gg 0$ and $\rho_0 = (1 + 0.1)/3$ at $q = q_{\max}$ (that corresponds to $\rho_0 \simeq (1 - 0.1)/3$ at $q = -q_{\max}$) in MFT [26]. An expansion of ten orders of magnitude in q_{\max} is marked by vertical dotted lines in Figs. 1(a) and 1(b), i.e., from a narrow region of $|q|/h < 2 \times 10^{-9}$ Hz in a free-space spinor BEC of 10^5 atoms to a much broader range of $|q|/h < 9$ Hz in $n=2$ spinor Mott insulators. Here h is the Planck constant. This drastic raise in q_{\max} as n decreases is also shown in Fig. 1(c) for a wide range of achievable n . In addition, the lattice-induced big reduction in n can relax the magnetization constraint on creating spin singlets by five orders of magnitude, because $|m| \lesssim 0.15/n$ is required for singlets at zero q [27]. Figure 1(d) indicates another big improvement made by cubic lattices: t_{\min} can be dramatically decreased by three orders of magnitude after a free-space spinor BEC enters the MI phase [16]. Here t_{\min} is the minimum time for generating singlets via adiabatically sweeping one parameter, such as q and the lattice depth u_L . Spin singlets of $F=1$ atoms can thus be created in realistic experimental setups, e.g., in the spinor Mott insulators of $|m| \leq 0.05$ as confirmed by our experimental data in Figs. 3 and 4.

In each experimental cycle, we prepare a LP or TP state at $q/h = 40$ Hz by pumping all atoms in the undesired m_F states of a $F=1$ spinor BEC to the $F=2$ state with resonant microwave pulses, and blasting away these $F=2$ atoms via a resonant laser pulse. We then quench q to a proper value in microwave dressing fields [28], and load atoms into a cubic lattice constructed by three standing waves along orthogonal directions. The lattice spacing is 532 nm, while lattice beams are originated from

a single-mode laser at 1064 nm and frequency-shifted by 20 MHz with respect to each other. We use Kapitza-Dirac diffraction patterns to calibrate u_L . Each data point in this paper is collected after atoms being abruptly released from a lattice at a fixed u_L and expanding ballistically within a given time of flight t_{TOF} . The standard Stern-Gerlach absorption imaging is a good method to measure ρ_{m_F} of spinor gases in the SF phase. Stern-Gerlach separations become indiscernible, when atoms completely lose phase coherence in the MI phase and the signal-to-noise ratio diminishes in TOF images. To measure ρ_0 in spinor Mott insulators, we develop a two-step microwave imaging method as follows: 1) count the $m_F=0$ atoms with the first imaging pulse preceded by transferring all atoms in the $|F=1, m_F=0\rangle$ state to the $F=2$ state; 2) count all remaining atoms that are in the $m_F = \pm 1$ states with the second imaging pulse. We compare these two imaging methods using a free-space spinor BEC, and find they give similar ρ_0 with a negligible difference (unless specified, all quoted uncertainties are 2 standard errors).

To ensure atoms adiabatically enter the MI phase, a cubic lattice is linearly ramped up within time t_{ramp} to $u_L = 26E_R$. Here E_R is the recoil energy [23]. We carefully select t_{ramp} based on three criteria. First, t_{ramp} should be long enough to satisfy $du_L/dt \ll 32\pi E_R^2/h$, the interband adiabaticity requirement [29]. Second, t_{ramp} should be larger than the MFT predicted t_{\min} , as explained in Fig. 1(d). These two criteria set $t_{\text{ramp}} > 5$ ms for our system. On the other hand, t_{ramp} should be sufficiently short, with $t_{\text{ramp}} \leq t_0$ to ensure lattice-induced heating is negligible and atom losses are not greater than 10%. Figure 2 explains how we determine t_0 from the observed relationship between t_{ramp} and ρ_0 in spinor Mott insulators at $u_L = 26E_R$ and $q/h = 460$ Hz. In such a high field, SF-MI phase transitions are second order because $U_2 = 0.04U_0 > 0$ and $q \gg U_2$ at this u_L for the

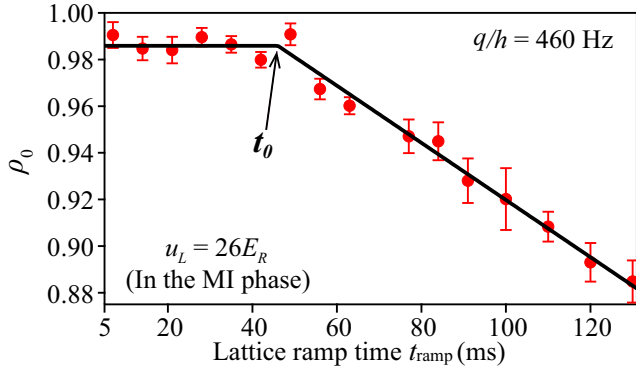


FIG. 2. Measured ρ_0 versus t_{ramp} after an initial LP spinor BEC enters the MI phase in a high field. Black lines are two linear fits. We estimate t_0 , the ideal t_{ramp} , from the intersection point of these two lines (see text).

sodium atoms [21]. Atoms initially in a LP state should thus stay in the LP state with $\rho_0 \simeq 1$, as they adiabatically cross the phase transitions and enter into the MI phase [21]. The value of ρ_0 quickly drops when inevitable heating is induced by lattices in a non-adiabatic lattice ramp sequence. We extract t_0 from the intersection point of two linear fits to the data in Fig. 2, which yields $t_{\text{ramp}} \leq t_0 \approx 45$ ms. Within this acceptable t_{ramp} range, a slower lattice ramp is preferred because it could more easily keep the system adiabatic and provide sufficient time for the atom redistribution processes [30]. The ideal lattice ramp speed is therefore set at $du_L/dt = 26E_R/t_0$ for our system.

The opposite limit is $|q| \ll U_2$ near zero q , where SF-MI phase transitions are first order and spin singlets are the ground state of $F=1$ spinor gases in the even Mott lobes [21]. We may thus identify the formation of spin singlets from evolutions of ρ_0 and $\Delta\rho_0$ during a first-order SF-MI transition. Figure 3 shows two such evolutions when atoms initially in the TP state are adiabatically loaded into the cubic lattice at the ideal lattice ramp speed to various final u_L in $q/h = -4$ Hz. These evolutions have three distinct regions. In the SF phase where $0 \leq u_L \leq 15E_R$, atoms remain in the TP state with $\rho_0 = 0$ and negligible $\Delta\rho_0$. As atoms cross first-order SF-MI transitions in $15E_R \leq u_L \leq 18E_R$, ρ_0 and $\Delta\rho_0$ sigmoidally increase with u_L . When all atoms enter into the MI phase at $u_L \geq 21E_R$, both ρ_0 and $\Delta\rho_0$ reach their equilibrium values of $\rho_0 \approx 0.3$ and $\Delta\rho_0 \gg 0$. These observations qualitatively agree with the characteristics of spin singlets. Despite that other factors can also increase $\Delta\rho_0$ in the MI phase, the measured $\Delta\rho_0$ is much smaller than the MFT prediction shown in Fig. 1(b). This may be due to the fact that the observed $\Delta\rho_0$ is an average over all 5×10^4 lattice sites in our system. Unless one can detect single lattice site precisely, the value of $\Delta\rho_0$ may not be used to verify spin singlets in lattice-confined spinor gases. We also monitor the time evolu-

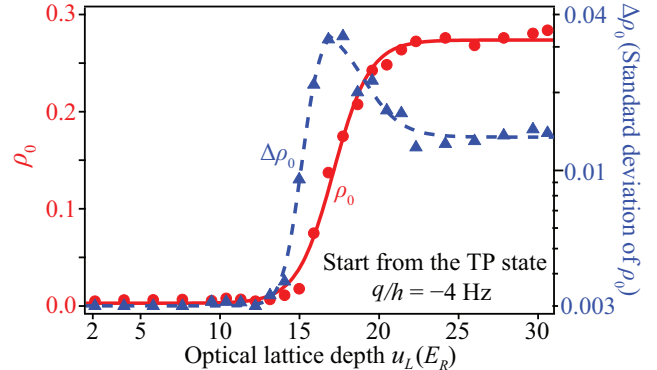


FIG. 3. Measured ρ_0 (red circles) and $\Delta\rho_0$ (blue triangles) versus u_L after an initial TP spinor BEC undergoes the ideal lattice sequence to various final u_L in a weak field near zero q . The solid line is a sigmoidal fit, and the dashed line is to guide the eye.

tion of atoms at fixed u_L and q after the ideal lattice ramp sequence. No spin oscillations are found at each q studied in this paper, which confirms atoms always stay at their ground states in these ideal lattice sequences.

We observe similar ρ_0 and $\Delta\rho_0$ evolutions within a wide range of q near zero field. The measured ρ_0 versus q in spinor Mott insulators at $u_L = 26E_R$ is shown in Fig. 4(a). These Mott insulators of $n_{\text{peak}} = 5$ are inhomogeneous systems, in which ρ_0 at a fixed q may be given by the weighted average over all Mott lobes:

$$\rho_0 = \sum_{j=1}^5 \rho_{0j} \chi_j. \quad (2)$$

Here ρ_{0j} is the MFT predicted ρ_0 in the ground state ψ_j of the $n=j$ Mott lobe, and χ_j represents mean-field atom density distributions in a harmonic trap [21]. The prediction of Eq. (2) shown by red dashed lines in Fig. 4(a), however, appears to largely disagree with our data. To understand this big discrepancy, we have tried several models and found only one phenomenological model can surprisingly describe our data without adjustable parameters (see black solid lines in Fig. 4(a)). This phenomenological model is based on one major difference between spinor and scalar Mott insulators predicted by the Bose-Hubbard model: i.e., the formation of spin singlets enlarges even Mott lobes in antiferromagnetic spinor gases [21]. For example, the $n=2$ even Mott lobe emerges at $u_L \approx 16.5E_R$, while the $n=3$ odd Mott lobe only exists in a much deeper lattice of $u_L \geq 19.5E_R$ for $F=1$ sodium spinor gases near zero field [21]. In the intermediate lattice depth of $16.5E_R < u_L < 19.5E_R$ near zero q , atoms in the $n=3$ lattice sites can freely tunnel among adjacent lattice sites, while particles in an $n=2$ lattice site already enter into the MI phase and are localized in this site. At a proper u_L near zero q , atoms may thus be able to redistribute among lattice sites with a given

odd n in the lattice-confined spinor gases. For example, at $u_L = 19E_R > 16.5E_R$, the tunneling of one atom converts two adjacent $n=3$ lattice sites to one $n=2$ and one $n=4$ sites. This u_L is then deep enough to localize the six atoms by forming a two-body spin singlet in one site and a 4-body spin singlet in the other site [30]. As a result of similar redistribution processes, atoms initially in lattice sites with $n = 5$ may form 4-body and 6-body spin singlets in the ideal lattice ramp sequences. In contrast, redistribution processes may not occur among the $n=1$ lattice sites, because the $n=1$ and $n=2$ Mott lobes emerge at similar u_L for the sodium atoms. Our phenomenological model takes these atom redistribution processes into account, and expresses ρ_0 in the spinor Mott insulators created by the ideal lattice ramp sequence as

$$\rho_0 = \sum_{j=3,5} \chi_j \frac{(j+1)\rho_{0,j+1} + (j-1)\rho_{0,j-1}}{2j} + \sum_{j=1,2,4} \rho_{0,j} \chi_j. \quad (3)$$

Figure 4(a) shows that the prediction of Eq. (3) agrees with our experimental data. The validity of this phenomenological model is also verified by comparing its prediction with the observed ρ_0 , after a resonant Rf-pulse is applied to rotate the spin of atoms by 90 degrees. In this paper, the spin rotation operator $\hat{R}_x = \exp(-i\frac{\pi}{2}\hat{S}_x)$ is along the x -axis, which is orthogonal to the quantization axis (z -axis). After $\pi/2$ spin rotations, $\rho_{0,j}$ in Eq. (3) changes to $\rho_{0,j}^r = \frac{\langle \psi_j | \hat{R}_x^\dagger \hat{n}_0 \hat{R}_x | \psi_j \rangle}{\langle \psi_j | \hat{R}_x^\dagger \hat{n}_x \hat{R}_x | \psi_j \rangle}$ in the $n=j$ Mott lobe. The prediction of Eq. (3) after these spin rotations is shown by the upper black solid line in Fig. 4(a), which well agrees with our data. The two data sets in Fig. 4(a) respectively represent projections of the atomic spin along two orthogonal axes. The observed good agreements between our phenomenological model and these data sets, therefore, suggest this model may reveal mechanisms of the ideal lattice ramp sequence in antiferromagnetic spinor gases.

Our data taken with and without the $\pi/2$ spin rotations appear to converge to a value around $\rho_0 \approx 1/3$ as q gets closer to zero in Fig. 4(a). This indicates the spinor Mott insulators become more rotationally invariant near zero field. As the spin rotational invariance is one unique signature of spin singlets, the reduced gap between the two data sets in Fig. 4(a) implies significant amounts of atoms may form spin singlets when q approaches zero. In our system, about 10% of atoms stay in the $n=1$ Mott lobe where no spin singlet can be formed. This accounts for the observed small gap between the two data sets near zero q in Fig. 4(a), and limits the maximum f_{ss} realizable in our system to about 90%. Here f_{ss} represents the fraction of atoms forming spin singlets in spinor gases. We extract f_{ss} from the measured ρ_0 based on Ref. [31]. The two data sets in Fig. 4(a) appear to yield similar

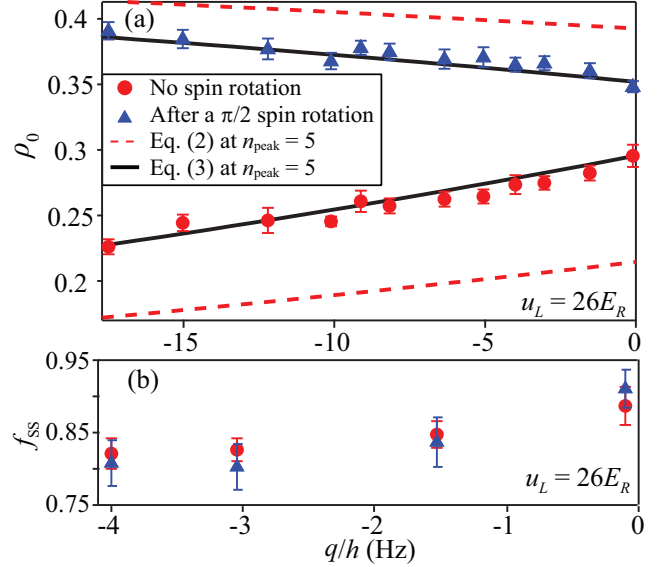


FIG. 4. (a) Red circles (blue triangles) are the measured ρ_0 in spinor Mott insulators without (with) atoms being rotated by resonant $\pi/2$ pulses at various q . The black solid (red dashed) line is the prediction of Eq. (3) (Eq. (2)). (b) Spin singlet fraction f_{ss} extracted from Panel (a) versus q (see text). The insulators are created after an initial TP spinor BEC undergoes the ideal lattice ramp sequence.

f_{ss} at a fixed q near zero field: i.e., $f_{ss} \approx 80\%$ when $-4 \text{ Hz} \leq q/h \leq 0 \text{ Hz}$ as shown in Fig. 4(b). This indicates around 80% of atoms form spin singlets in our system. Similar phenomena and slightly smaller f_{ss} are also observed in spinor Mott insulators generated after atoms initially in the LP state cross first-order SF-MI transitions in the ideal lattice ramp sequences when $q > 0$.

In conclusion, our experimental data have confirmed that combining cubic lattices with spinor BECs makes spin singlets of ultracold spin-1 atoms achievable in experimentally accessible regions. Via two independent detection methods, we have demonstrated that about 80% of atoms in the lattice-confined $F=1$ spinor BEC form spin singlets, after the atoms cross first-order SF-MI phase transitions near zero field. We have developed a phenomenological model that explains our observations without adjustable parameters. Our recent work has also indicated that we may be able to identify another signature of spin singlets, i.e., confirm their zero spin nematicity in light scattering measurements [32].

We thank the National Science Foundation and the Oklahoma Center for the Advancement of Science and Technology for financial support.

* Electronic address: yingmei.liu@okstate.edu

[1] C. C. Huang, M. S. Chang, and S. K. Yip, Phys. Rev. A **86**, 013403 (2012).

- [2] G. Tóth, and M. W. Mitchell, *New J. Phys.* **12**, 053007 (2010).
- [3] H. Sun, P. Xu, H. Pu, and W. Zhang, *Phys. Rev. A* **95**, 063624 (2017)
- [4] N. Behbood, F. Martin Ciurana, G. Colangelo, M. Napolitano, G. Tóth, R. J. Sewell, and M. W. Mitchell, *Phys. Rev. Lett.* **113**, 093601 (2014).
- [5] K. Eckert, L. Zawitkowski, A. Sanpera, M. Lewenstein, and E. S. Polzik, *Phys. Rev. Lett.* **98**, 100404 (2007).
- [6] G. Tóth, *Phys. Rev. A* **69**, 052327 (2004).
- [7] S. Ashhab and A. J. Leggett, *Phys. Rev. A* **68**, 063612 (2003).
- [8] F. Ciccarello, M. Paternostro, S. Bose, D. E. Browne, G. M. Palma, and M. Zarcone, *Phys. Rev. A* **82**, 030302(R) (2010).
- [9] I. Urizar-Lanz, P. Hyllus, I. L. Egusquiza, M. W. Mitchell, and G. Tóth, *Phys. Rev. A* **88**, 013626 (2013).
- [10] T. L. Ho and S. K. Yip, *Phys. Rev. Lett.* **84**, 4031 (2000).
- [11] C. K. Law, H. Pu, and N. P. Bigelow, *Phys. Rev. Lett.* **81**, 5257 (1998).
- [12] E. J. Mueller, T. L. Ho, M. Ueda, and G. Baym, *Phys. Rev. A* **74**, 033612 (2006).
- [13] A. Sala, D. L. Núñez, J. Martorell, L. De Sarlo, T. Zibold, F. Gerbier, A. Polls, and B. Juliá-Díaz, *Phys. Rev. A* **94**, 043623(2016).
- [14] L. De Sarlo, L. Shao, V. Corre, T. Zibold, D. Jacob, J. Dalibard, and F. Gerbier, *New J. Phys.* **15**, 113039 (2013).
- [15] Y. Eto, H. Ikeda, H. Suzuki, S. Hasegawa, Y. Tomiyama, S. Sekine, M. Sadgrove, and T. Hirano, *Phys. Rev. A* **88**, 031602(R)(2013)
- [16] Our MFT calculations are based on Ref. [24] with $t_{\min} = h/\Delta E$. Here ΔE is the energy gap between the ground state and the first excited state.
- [17] A. Imambekov, M. Lukin, and E. Demler, *Phys. Rev. A* **68**, 063602 (2003).
- [18] J. Javanainen, *J. Phys. B* **33**, 5493 (2000).
- [19] F. Zhou, *Int. J. Mod. Phys. B* **17**, 2643 (2003).
- [20] I. Carusotto and E. J. Mueller, *J. Phys. B* **37**, S115 (2004).
- [21] J. Jiang, L. Zhao, S.-T. Wang, Z. Chen, T. Tang, L.-M. Duan, and Y. Liu, *Phys. Rev. A* **93**, 063607 (2016), and the references therein.
- [22] D. M. Stamper-Kurn and M. Ueda, *Rev. Mod. Phys.* **85**, 1191 (2013).
- [23] L. Zhao, J. Jiang, T. Tang, M. Webb, and Y. Liu, *Phys. Rev. Lett.* **114**, 225302 (2015).
- [24] J. Jiang, L. Zhao, M. Webb, and Y. Liu, *Phys. Rev. A* **90**, 023610 (2014).
- [25] T.-L. Ho, *Phys. Rev. Lett.* **81**, 742 (1998); T. Ohmi and K. Machida, *J. Phys. Soc. Jpn.* **67**, 1822 (1998).
- [26] Our criterion for determining q_{\max} is stricter than those used in Refs. [13, 14].
- [27] We derive this magnetization constraint from Eq. 3 of Ref. [10].
- [28] L. Zhao, J. Jiang, T. Tang, M. Webb, and Y. Liu, *Phys. Rev. A* **89**, 023608 (2014).
- [29] J. K. Chin, D. E. Miller, Y. Liu, C. Stan, W. Setiawan, C. Sanner, K. Xu, and W. Ketterle, *Nature* **443**, 961 (2006).
- [30] The required time for the atom redistribution process is proportional to $(6nJ)^{-1}$ in cubic lattices. This may set $t_{\text{ramp}} \geq 35$ ms for our system.
- [31] Our phenomenological model predicts that $\rho_0 = f_{\text{ss}}/3 (= f_{\text{ss}}/3 + (1 - f_{\text{ss}})/2)$ in spinor Mott insulators created from an initial TP spinor BEC in the ideal lattice sequence without (with) $\pi/2$ spin rotations. This prediction only works near zero q and slightly underestimates f_{ss} .
- [32] T. Tang, L. Zhao, Z. Chen, and Y. Liu (unpublished).

APPENDIX C

FIRST-ORDER SUPERFLUID-TO-MOTT-INSULATOR PHASE TRANSITIONS IN SPINOR CONDENSATES

This appendix includes a reprint of Ref. [68]: J. Jiang, L. Zhao, S.-T. Wang, Z. Chen, T. Tang, L.-M. Duan, and Y. Liu, First-order superfluid-to-Mott-insulator phase transitions in spinor condensates, *Phys. Rev. A* 93, 063607 (2016).

First-order superfluid-to-Mott-insulator phase transitions in spinor condensates

J. Jiang,^{1,*} L. Zhao,^{1,*} S.-T. Wang,² Z. Chen,¹ T. Tang,¹ L.-M. Duan,² and Y. Liu^{1,†}

¹*Department of Physics, Oklahoma State University, Stillwater, Oklahoma 74078, USA*

²*Department of Physics, University of Michigan, Ann Arbor, Michigan 48109, USA*

(Received 14 December 2015; revised manuscript received 28 March 2016; published 7 June 2016)

We observe evidence of first-order superfluid-to-Mott-insulator quantum phase transitions in a lattice-confined antiferromagnetic spinor Bose-Einstein condensate. The observed signatures include the hysteresis effect, significant heatings across the phase transitions, and changes in spin populations due to the formation of spin singlets in the Mott-insulator phase. The nature of the phase transitions is found to strongly depend on the ratio of the quadratic Zeeman energy to the spin-dependent interaction. Our observations are qualitatively understood by the mean field theory and suggest tuning the quadratic Zeeman energy is a new approach to realize superfluid-to-Mott-insulator phase transitions.

DOI: [10.1103/PhysRevA.93.063607](https://doi.org/10.1103/PhysRevA.93.063607)

I. INTRODUCTION

A quantum phase transition from a superfluid (SF) to a Mott insulator (MI) was realized in a scalar Bose-Einstein condensate (BEC) trapped by three-dimensional (3D) optical lattices about a decade ago [1]. Marking an important milestone, this achievement has stimulated tremendous efforts to apply highly controllable ultracold bosonic and fermionic systems in studying condensed matter models [2–6]. The SF-MI transitions have been confirmed in various scalar BEC systems via different techniques that can efficiently control the ratio of interatomic interactions to the mobility of atoms [1,5–7]. One well-known approach to simultaneously enhance interatomic interactions and suppress atomic motion is by raising the depth of an optical lattice [1]. Another convenient method is to manipulate interactions with a magnetically tuned Feshbach resonance [7]. A third technique is to control the hopping energy of bosonic atoms by periodically shaking the lattice [6]. Spinor BECs, on the other hand, possess an additional spin degree of freedom, leading to a range of phenomena absent in scalar BECs [8–14]. One important prediction is the existence of first-order SF-MI phase transitions in lattice-trapped antiferromagnetic spinor BECs [2,11,13,15–18]. In contrast, the phase transitions can only be second order in scalar BECs and ferromagnetic spinor BECs [2,5,17].

In this paper, SF-MI transitions are studied in sodium antiferromagnetic spinor BECs confined by cubic optical lattices. We observe the hysteresis effect, changes in spin components, and substantial heating across the phase transitions. These indicate the existence of metastable states, the formation of spin singlets, and associated first-order transitions. In the ground state of the spinor BECs, the nature of SF-MI transitions is found to be determined by the competition between the quadratic Zeeman energy q_B and the spin-dependent interaction U_2 . At low magnetic fields where U_2 dominates, signatures of first-order transitions are observed. In the opposite limit, the transitions appear to be second order and resemble those occurring in scalar BECs. These qualitative features are explained by our mean-field

(MF) calculations. We also study the phase transitions with an initial metastable state and observe stronger heatings across all magnetic fields. Furthermore, our data indicate a new technique to realize SF-MI transitions is by varying q_B .

We describe lattice-trapped $F = 1$ spinor BECs with the Bose-Hubbard (BH) model [15,19]. In the decoupling MF approximation, the Hamiltonian can be reduced to a site-independent form [12,18,20]:

$$H_{\text{MF}} = \frac{U_0}{2}n(n-1) + \frac{U_2}{2}(\vec{S}^2 - 2n) + q_B \sum_{m_F} m_F^2 n_{m_F} - \mu n - zJ \sum_{m_F} (\phi_{m_F}^* b_{m_F} + \phi_{m_F} b_{m_F}^\dagger) + zJ |\vec{\phi}|^2. \quad (1)$$

U_0 is the spin-independent interaction, $n = \sum_{m_F} n_{m_F}$, and $n_{m_F} = b_{m_F}^\dagger b_{m_F}$ is the atom number per site of the m_F state. The vector order parameter is $\phi_{m_F} \equiv \langle b_{m_F} \rangle$, μ is the chemical potential, J is the nearest-neighbor hopping energy, z is the number of nearest neighbors, and \vec{S} is the spin operator [21]. U_2 is positive (negative) in $F = 1$ antiferromagnetic (ferromagnetic) spinor BECs, e.g., $U_2 \simeq 0.04U_0$ in a ^{23}Na system [22]. With spatially uniform superfluids in equilibrium, one can assume ϕ_{m_F} to be real. $\phi_{m_F} = 0$ ($\neq 0$) in the MI (SF) phase.

An antiferromagnetic $F = 1$ spinor BEC of zero magnetization forms a polar superfluid in equilibrium with $\langle \vec{S} \rangle = 0$ [2,22–24]. There are two types of polar superfluids: the longitudinal polar (LP) state with $(\phi_1, \phi_0, \phi_{-1}) = \sqrt{N_{\text{SF}}}(0, 1, 0)$, and the transverse polar (TP) state with $(\phi_1, \phi_0, \phi_{-1}) = \sqrt{N_{\text{SF}}/2}(1, 0, 1)$. Here N_{SF} is the number of condensed atoms per site. At zero q_B and the same N_{SF} , TP and LP states are degenerate in energy. At $q_B > 0$, the MF ground state is always the LP state, but a metastable TP phase may exist [2,24].

Our MF calculations show that q_B/U_2 is a key factor to understand the nature of SF-MI transitions in antiferromagnetic spinor BECs [25]. At low magnetic fields (where $0 \leq q_B \lesssim U_2$), U_2 penalizes high-spin configurations and enlarges the Mott lobes for even number fillings as atoms can form spin singlets to minimize the energy. Metastable Mott-insulator (MMI) and metastable superfluid (MSF) phases emerge due to the spin barrier and lead to first-order SF-MI transitions [see Figs. 1(a) and 1(c)] [15–18]. When 3D lattices are ramped up

*These authors contributed equally to this work.

†yingmei.liu@okstate.edu

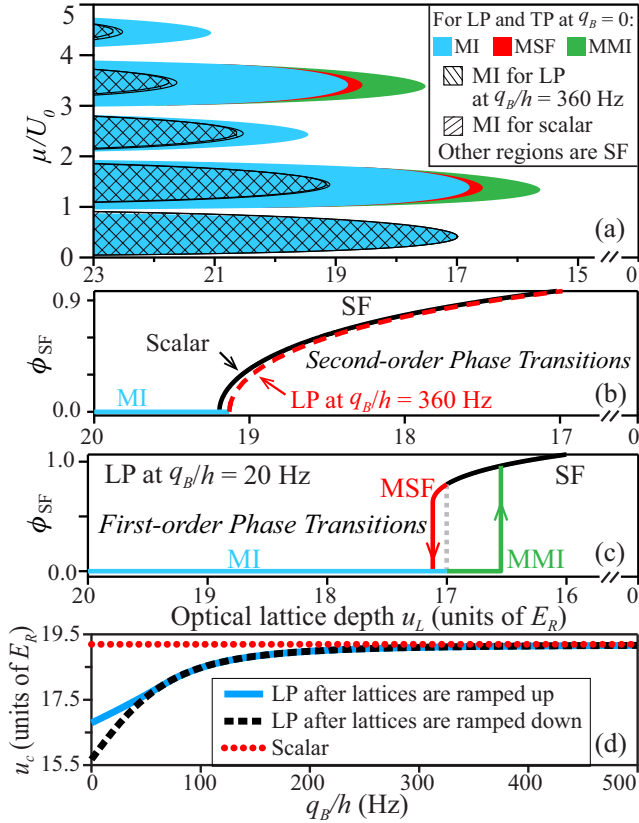


FIG. 1. (a) MF phase diagrams derived from the BH model for scalar BECs [19] and the LP and TP sodium spinor BECs in cubic lattices [see Eq. (1)]. The superfluid order parameter ϕ_{SF} versus u_L at $\mu/U_0 = 1.4$ in (b) scalar and LP spinor BECs at $q_B/h = 360$ Hz and (c) LP spinor BECs at $q_B/h = 20$ Hz. Here $|\phi_{SF}|^2 = N_{SF}$ and h is the Planck constant. (d) Predicted SF-MI transition point u_c versus q_B at $\mu/U_0 = 1.4$ [see Eq. (1)].

and down, hysteresis is expected across the phase transitions (i.e., different transition lattice depth u_c). In addition, when the system changes from a metastable phase to a stable phase (e.g., from MSF to MI), there will be a jump in the order parameter and the system energy, leading to unavoidable heating to the atoms. Hence, hysteresis, substantial heating, and the formation of spin singlets may be interpreted as signatures of first-order transitions. As q_B increases, the $m_F = 0$ state has lower energy than other m_F levels and U_2 becomes less relevant. When q_B becomes sufficiently larger than U_2 ($U_2/h \lesssim 80$ Hz in this work), the ground state phase diagram of antiferromagnetic spinor BECs reverts back to one that is similar to the scalar BH model with only second-order SF-MI transitions (see Fig. 1).

II. EXPERIMENTAL SETUP

Three different types of BECs (i.e., scalar BECs, LP and TP spinor BECs) are studied in this work. A scalar BEC containing up to 1.2×10^5 sodium atoms in the $|F = 1, m_F = -1\rangle$ state is created with an all-optical approach similar to Ref. [26]. A $F = 1$ spinor BEC of zero magnetization is then produced by imposing a resonant rf pulse to the scalar BEC at a fixed

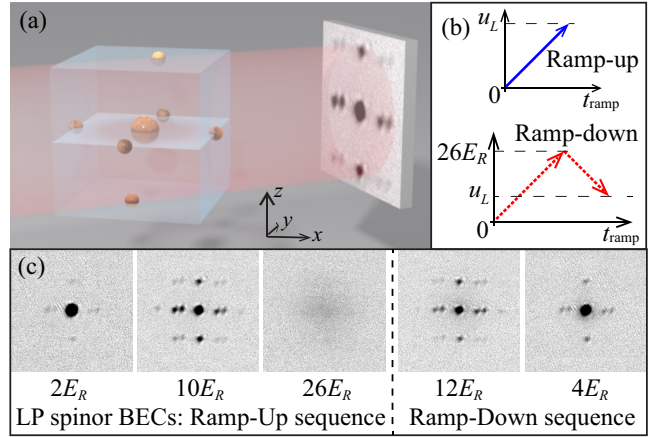


FIG. 2. (a) Schematic of the reciprocal lattice and a TOF image taken after lattices are abruptly released. The area in red represents the imaging beam. (b) Two lattice ramp sequences used in this paper. (c) Interference patterns observed after we abruptly release LP spinor BECs at various final u_L followed by a 5.5-ms TOF at $q_B/h = 360$ Hz. The left (right) panel is taken after ramp-up (ramp-down) sequences. The field of view is $400 \mu\text{m} \times 400 \mu\text{m}$.

q_B . Since the LP state (where $\rho_0 = 1$) is the MF ground state, it can be prepared by simply holding the spinor BEC for a sufficiently long time at high magnetic fields [24]. Here ρ_{m_F} is the fractional population of each m_F state. The TP state (where $\rho_{\pm 1} = 0.5$) is generated via a different approach: we apply a resonant microwave pulse to transfer all $m_F = 0$ atoms in the $F = 1$ spinor BEC to the $F = 2$ state, and then blast away these $F = 2$ atoms with a resonant laser pulse. After quenching q_B to a desired value, we adiabatically load the BEC into a cubic optical lattice within time t_{ramp} . This 3D lattice is constructed by three optical standing waves from a single-mode laser at 1064 nm, which results in a cubic periodic potential with a lattice spacing of 532 nm. All lattice beams are frequency-shifted by at least 20 MHz with respect to each other for eliminating cross interference among them. The calibration of optical lattice depth u_L is conducted via Kapitza-Dirac diffraction patterns and has an uncertainty of $\sim 15\%$. As shown in Fig. 2(b), lattices are linearly ramped up to a given u_L in a ramp-up sequence, while lattices are first adiabatically ramped up to $26E_R$ and then back down to a variable final u_L in a ramp-down sequence. Here $E_R = \hbar^2 k_L^2 / (2M)$ is the recoil energy, M and \hbar are, respectively, the atomic mass and the reduced Planck constant, and k_L is the lattice wave vector. We find that a ramp speed of $2E_R/\text{ms}$ is sufficient to satisfy the intraband adiabaticity condition and ensure $\geq 80\%$ of atoms remain in a scalar or a high-field LP spinor BEC after a ramp-down sequence to $2E_R$. We measure ρ_{m_F} with Stern-Gerlach imaging and microwave imaging after a certain time of flight (TOF).

III. FIRST-ORDER SUPERFLUID TO MOTT-INSULATOR PHASE TRANSITIONS

Distinct interference peaks can always be observed during ballistic expansion, after each BEC is abruptly released from

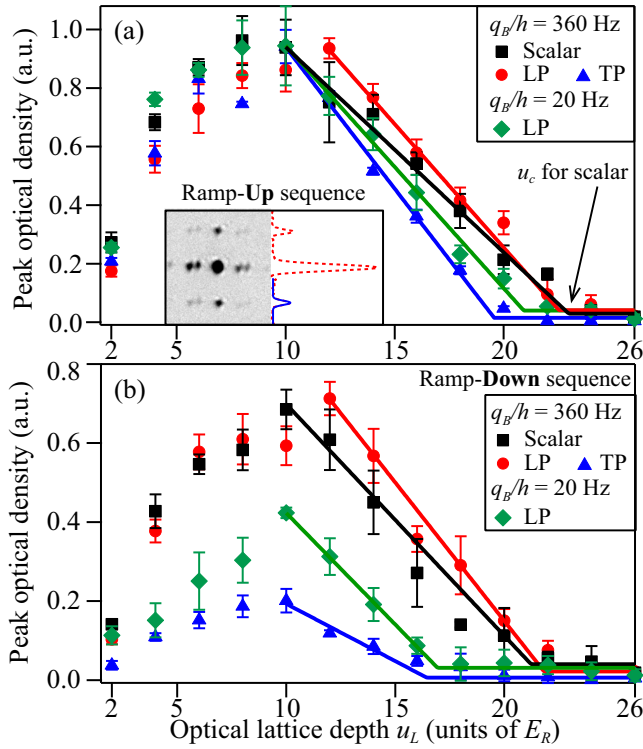


FIG. 3. (a) Peak OD of interference peaks versus u_L after lattice ramp-up sequences. Markers are experimental data, and lines are linear fits. We estimate u_c from the intersection of two linear fits to the data. The inset shows how we extract the peak OD from a TOF image (left). The dotted line in the right inset is a density profile of this TOF image through the central and one pair of interference peaks along the vertical direction, while the solid line is a bimodal fit to one side peak. (b) Similar to panel (a) except that all data are taken after lattice ramp-down sequences.

a shallow lattice of $u_L \leq 10E_R$. As shown in the TOF images in Fig. 2, the six first-order diffracted peaks are symmetrically set apart from the central peak by a distance corresponding to a momentum of $2\hbar k_L$ along three orthogonal axes. These interference peaks may be considered as evidence for coherence associated with the SF phase. In fact, a larger visibility of interference patterns, a narrower width of the central peak, and a higher optical density (OD) of interference peaks have all been used as trustworthy evidence for improved phase coherence in atomic systems [1,3,5,27].

TOF images in Fig. 2(c) show the loss and revival of the interference contrast in spinor BECs as cubic lattices are ramped up and down. A quantitative analysis of these TOF images demonstrates the interference peaks (i.e., coherence associated with the SF phase) change in a reversible manner with u_L (see Fig. 3). First, the interference patterns become more visible as lattices are made deeper and reach their maximum OD around $10E_R$. This may be due to lattice-enhanced density modulation [3,5,27]. Second, when u_L is further increased and exceeds u_c , the interference peaks steadily smear out to a single broad peak indicating atoms completely lose phase coherence. We extract u_c in Fig. 3 from the intersection of two linear fits to the data of a given BEC. To confirm the system has undergone a SF-MI transition, we monitor lattice ramp-down sequences, because

one characteristic of a MI state has proven to be a loss of phase coherence in deep lattices and a subsequent rapid revival of coherence as u_L is reduced [1,3,5]. The interference peaks of scalar and spinor BECs reversibly revive after ramp-down sequences, indicating atoms quickly recombine and return to SF states [see Fig. 3(b)].

Observations in Fig. 3 are qualitatively consistent with our MF calculations and suggest the existence of first-order SF-MI transitions under some circumstances. First, LP spinor BECs at high magnetic fields possess many properties (e.g., the peak OD) that are similar to those of scalar BECs. Their ramp-up and ramp-down curves are close to each other, while both have roughly symmetric transition points u_c . Similar phenomena were observed in ^{87}Rb and ^6Li systems and have been considered as signatures of second-order SF-MI transitions [1,3,5]. Second, LP states at low magnetic fields and TP states at high fields apparently have smaller u_c for both ramp-up and ramp-down processes compared to scalar BECs, suggesting enlarged Mott lobes. In particular, the ramp-down u_c for LP states at low fields is noticeably smaller than their ramp-up u_c , corroborating with the MF picture that hysteresis occurs across first-order phase transitions. Third, the recovered interference contrast is visibly different for various BECs after the ramp-down process (after SF-MI transitions). For scalar and high-field LP spinor BECs, nearly 75% of peak OD can be recovered in the interference peaks after ramp-down sequences. The slightly reduced interference contrast may be due to unaccounted heatings, which leads a small portion of atoms ($< 20\%$) to populate the Brillouin zone. In contrast, after we utilized quite a few techniques and optimized many parameters, the maximal recovered interference contrast of low-field LP states is only $\sim 40\%$ ($\sim 20\%$ for high-field TP states). We attribute this to unavoidable heatings across the first-order transitions as there is a jump in system energy between metastable states and stable states. Both hysteresis effect and significant heatings strongly suggest that first-order SF-MI transitions are realized in our experiment. Note, however, we do not see noticeable jumps in the observables as is typically associated with first-order transitions. This is likely due to the presence of even and odd atom fillings in inhomogeneous systems such as trapped BECs, although predicted first-order SF-MI transitions only exist for even occupancy number. Limited experimental resolutions may be another reason.

Our data in Fig. 3(b) also demonstrate that a new approach to realize SF-MI transitions is by ramping q_B at a fixed u_L . For example, when the final u_L in ramp-down sequences is set at a value between $17E_R$ and $21E_R$, atoms in LP spinor BECs can cross SF-MI transitions if q_B/h is sufficiently reduced (e.g., from 360 to 20 Hz). This agrees with Fig. 1(d): u_c depends on q_B .

We then compare scalar and spinor BECs within a wide range of magnetic fields, $20\text{ Hz} \leq q_B/h \leq 500\text{ Hz}$, after identical lattice ramp sequences to $u_L = 10E_R$. We choose $10E_R$ because it is apparently the lattice depth around which we observe the maximum interference contrast, with negligible difference in scalar and spinor BECs after ramp-up sequences at all q_B . This is consistent with Fig. 1, which predicts all BECs studied in this work should be well in the SF phase at $10E_R$. However, the interference peak ODs show intriguing

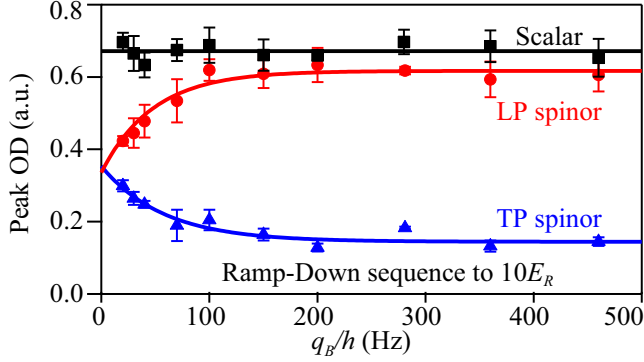


FIG. 4. Peak OD of interference peaks versus q_B observed after lattice ramp-down sequences to $10E_R$. Markers are experimental data. Red and blue lines are exponential fits. The black line is a linear fit.

differences after ramp-down sequences to $10E_R$ (see Fig. 4): deviations from the maximal value appear for LP spinor BECs at low magnetic fields and the TP state at all positive q_B . We again attribute this to different amount of heatings across SF-MI transitions. Different extent of heatings may be produced due to different spin barriers as well as the amount of energy jump across the transitions. Hence, the maximum recovered OD is a good indicator for the appearance or disappearance of first-order SF-MI transitions. Notably, LP spinor BECs are found to behave very similarly to scalar BECs when $q_B \gg U_2$ (see Fig. 4). This observation is consistent with Fig. 1(d), in which the two MF curves for the LP state merge indicating that metastable states disappear and SF-MI transitions become second order when $q_B/h > 70$ Hz. Furthermore, the difference between LP and TP spinor BECs appears to exponentially decrease as q_B approaches zero. Exponential fits to the data verify that LP and TP spinor BECs should show the same behavior at $q_B = 0$.

Figure 5(a) shows the change in the fractional population ρ_0 as the lattice is ramped up, which provides another evidence that is consistent with first-order SF-MI transitions. In the MF picture, the first-order transition is related to the formation of spin singlets in the even lobe MI phase. For example, in the $n = 2$ MI lobe, the MI ground state $|\psi_g\rangle$ at zero q_B is the singlet state where $\rho_0 = \rho_{+1} = \rho_{-1} = 1/3$ [11, 13, 15–18], i.e., $|\psi_g(q_B = 0)\rangle = |S = 0, S_z = 0\rangle = \frac{\sqrt{2}}{3}|101\rangle - \frac{\sqrt{1}}{3}|020\rangle$ in the occupation basis of $|n_1, n_0, n_{-1}\rangle$. For $q_B > 0$, we diagonalize Eq. (1) in this occupation basis and find $|\psi_g\rangle = \frac{U_2 - 2q_B + \sqrt{4q_B^2 - 4q_B U_2 + 9U_2^2}}{2\sqrt{2}U_2}|101\rangle - |020\rangle$. This calculation result is shown in Fig. 5(b). A line at $u_L = 26E_R$ from Fig. 5(b) represents the result in the $n = 2$ Mott lobe, which is also highlighted as the theoretical $n = 2$ line in Fig. 5(a) inset. Two predictions can be derived from this MF calculation: ρ_0 drastically decreases as atoms cross the first-order transition (from SF to MI), and ρ_0 rises with q_B in the $n = 2$ Mott lobe.

Our observations shown in Fig. 5(a) may be the first experimental confirmation of these predictions: an initial LP state is found to sigmoidally evolve to a state consisting of all three m_F components as u_L is ramped up at low magnetic fields, with the measured ρ_0 sigmoidally decreasing from one in the SF phase to around 0.6 in the MI phase

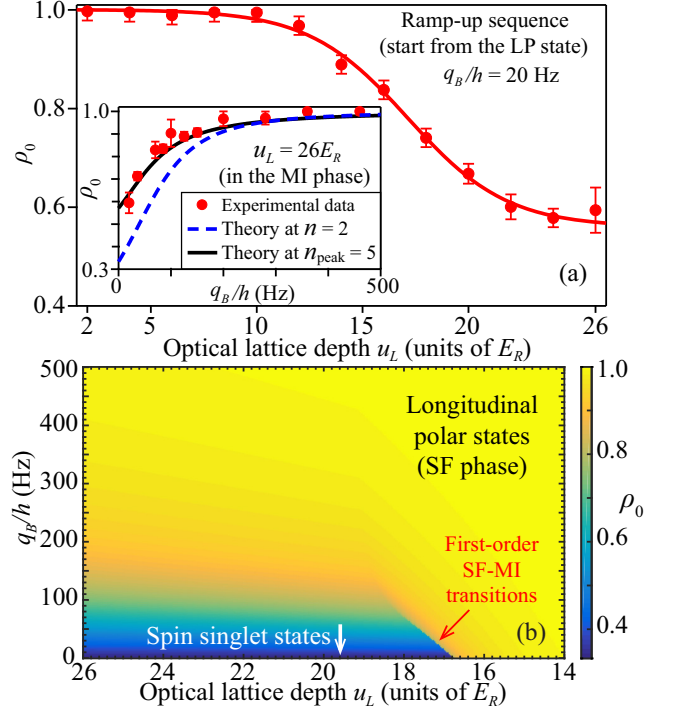


FIG. 5. (a) Measured ρ_0 versus u_L after an initial LP spinor BEC undergoes ramp-up sequences to various final u_L at $q_B/h = 20$ Hz. The solid line is a sigmoidal fit. Inset: Similar to the main figure except that we set q_B at various values and the final u_L at $26 E_R$ to ensure atoms enter into the MI phase. The dashed (solid) line represents the MF result for $n = 2$ ($n_{\text{peak}} = 5$). (b) Predicted ρ_0 in the ground state of antiferromagnetic spinor BECs at various u_L and q_B with $\mu/U_0 = 1.4$.

($u_L \geq 22E_R$). In addition, in the MI phase, the measured ρ_0 rises with q_B , and approaches one at $q_B \gg U_2$ where the ground state phase diagram of antiferromagnetic spinor BECs resembles the scalar BH model with only second-order SF-MI transitions [see Fig. 5(a) inset]. This observation can be well understood by the MF calculation [the $n_{\text{peak}} = 5$ line in Fig. 5(a) inset]. Note that the peak filling factor n_{peak} is five in our inhomogeneous system, and the data in Fig. 5(a) thus represent an average of different atom fillings. In other words, the theoretical $n_{\text{peak}} = 5$ line in Fig. 5(a) inset represents a weighted average of the MF predictions at five different n (i.e., $n = 1, 2, 3, 4, 5$) based on the atom density distribution in a harmonic trap. Good agreements between our data and the MF theory suggest that the observed substantial change in ρ_0 at very low fields may be mainly due to the formation of spin singlets in the even lobe MI phase (after atoms cross the first-order transitions).

IV. CONCLUSION

In conclusion, we have conducted the first experimental study on SF-MI transitions in lattice-confined sodium spinor BECs. We have observed hysteresis, significant heatings across the phase transitions, and the change in ρ_0 resulting from the formation of spin singlets in the MI phase. These observations strongly suggest first-order SF-MI transitions are realized

in our system. Our data are understood by the MF theory and suggest SF-MI transitions can be realized by tuning q_B . Further studies are required to confirm more signatures of the first-order transitions, e.g., by precisely imaging Mott shells [4,7].

ACKNOWLEDGMENTS

We thank the Army Research Office and the National Science Foundation for financial support. S.T.W. and L.M.D. are supported by the IARPA, the ARL, and the AFOSR MURI program. S.T.W. thanks Xiaopeng Li for helpful discussions.

-
- [1] M. Greiner, O. Mandel, T. Esslinger, T. W. Hänsch, and I. Bloch, *Nature (London)* **415**, 39 (2002).
- [2] D. M. Stamper-Kurn and M. Ueda, *Rev. Mod. Phys.* **85**, 1191 (2013).
- [3] J. K. Chin, D. E. Miller, Y. Liu, C. Stan, W. Setiawan, C. Sanner, K. Xu, and W. Ketterle, *Nature (London)* **443**, 961 (2006).
- [4] G. K. Campbell, J. Mun, M. Boyd, P. Medley, A. E. Leanhardt, L. G. Marcassa, D. E. Pritchard, and W. Ketterle, *Science* **313**, 649 (2006).
- [5] I. Bloch, J. Dalibard, and W. Zwerger, *Rev. Mod. Phys.* **80**, 885 (2008).
- [6] H. Lignier, C. Sias, D. Ciampini, Y. Singh, A. Zenesini, O. Morsch, and E. Arimondo, *Phys. Rev. Lett.* **99**, 220403 (2007).
- [7] C. Chin, R. Grimm, P. Julienne, and E. Tiesinga, *Rev. Mod. Phys.* **82**, 1225 (2010).
- [8] P. Windpassinger and K. Sengstock, *Rep. Prog. Phys.* **76**, 086401 (2013).
- [9] J. Heinze, S. Götzke, J. S. Krauser, B. Hundt, N. Fläschner, D.-S. Lühmann, C. Becker, and K. Sengstock, *Phys. Rev. Lett.* **107**, 135303 (2011).
- [10] P. Soltan-Panahi, J. Struck, P. Hauke, A. Bick, W. Plenkers, G. Meineke, C. Becker, P. Windpassinger, M. Lewenstein, and K. Sengstock, *Nat. Phys.* **7**, 434 (2011).
- [11] S. S. Natu, J. H. Pixley, and S. Das Sarma, *Phys. Rev. A* **91**, 043620 (2015).
- [12] K. W. Mahmud and E. Tiesinga, *Phys. Rev. A* **88**, 023602 (2013).
- [13] G. G. Batrouni, V. G. Rousseau, and R. T. Scalettar, *Phys. Rev. Lett.* **102**, 140402 (2009).
- [14] M. Shinozaki, S. Tsuchiya, S. Abe, T. Ozaki, and T. Nikuni, *J. Low Temp. Phys.* **175**, 236 (2014).
- [15] E. Demler and F. Zhou, *Phys. Rev. Lett.* **88**, 163001 (2002); A. Imambekov, M. Lukin, and E. Demler, *Phys. Rev. A* **68**, 063602 (2003).
- [16] K. V. Krutitsky, M. Timmer, and R. Graham, *Phys. Rev. A* **71**, 033623 (2005).
- [17] T. Kimura, S. Tsuchiya, and S. Kurihara, *Phys. Rev. Lett.* **94**, 110403 (2005).
- [18] D. Yamamoto, T. Ozaki, C. A. R. Sa de Melo, and I. Danshita, *Phys. Rev. A* **88**, 033624 (2013).
- [19] M. P. A. Fisher, P. B. Weichman, G. Grinstein, and D. S. Fisher, *Phys. Rev. B* **40**, 546 (1989).
- [20] R. V. Pai, K. Sheshadri, and R. Pandit, *Phys. Rev. B* **77**, 014503 (2008); A. Wagner, Spinor condensates in optical superlattices, Ph.D. thesis, University of Basel, 2012.
- [21] The linear Zeeman energy is ignored in Eq. (1), since it remains unchanged during collisional spin interconversions in $F = 1$ spinor BECs. The spin operators are given by $S_x = \frac{1}{\sqrt{2}}(b_0^\dagger b_1 + b_1^\dagger b_0 + b_{-1}^\dagger b_0 + b_0^\dagger b_{-1})$, $S_y = \frac{i}{\sqrt{2}}(b_0^\dagger b_1 - b_1^\dagger b_0 + b_{-1}^\dagger b_0 - b_0^\dagger b_{-1})$, $S_z = b_1^\dagger b_1 - b_{-1}^\dagger b_{-1}$.
- [22] L. Zhao, J. Jiang, T. Tang, M. Webb, and Y. Liu, *Phys. Rev. Lett.* **114**, 225302 (2015).
- [23] T.-L. Ho, *Phys. Rev. Lett.* **81**, 742 (1998); T. Ohmi and K. Machida, *J. Phys. Soc. Jpn.* **67**, 1822 (1998).
- [24] J. Jiang, L. Zhao, M. Webb, and Y. Liu, *Phys. Rev. A* **90**, 023610 (2014).
- [25] We solve Eq. (1) self-consistently by requiring $\phi_{m_F} = \langle b_{m_F} \rangle$ in the occupancy number n basis with a maximum of 15 atoms per site. Since the observed n_{peak} is five, the truncation errors are negligible.
- [26] L. Zhao, J. Jiang, T. Tang, M. Webb, and Y. Liu, *Phys. Rev. A* **89**, 023608 (2014).
- [27] K. Xu, Y. Liu, D. E. Miller, J. K. Chin, W. Setiawan, and W. Ketterle, *Phys. Rev. Lett.* **96**, 180405 (2006).

VITA

Zihe Chen

Candidate for the Degree of

Doctor of Philosophy

Dissertation: NON-EQUILIBRIUM DYNAMICS IN LATTICE-CONFINED ANTIFERROMAGNETIC SPINOR CONDENSATES

Major Field: Photonics

Biographical:

Education:

Completed the requirements for the Doctor of Philosophy in Photonics at Oklahoma State University, Stillwater, Oklahoma in December, 2020.

Completed the requirements for the Bachelor of Science in Physics at Nanjing University, Nanjing, China in 2014.

Professional Memberships:

American Physical Society